Excited State Structural Dynamics of Carotenoids and Charge Transfer Systems

by

Aaron Justin Van Tassle

B.S. (University of Illinois at Chicago) 2000

A dissertation submitted in partial satisfaction of the

requirements for the degree of

Doctor of Philosophy

in

Chemistry

in the

GRADUATE DIVISION

of the

UNIVERSITY OF CALIFORNIA, BERKELEY

Committee in charge:

Professor Graham R. Fleming, Chair

Professor Charles B. Harris

Professor Ehud Isacoff

Fall 2006

Excited State Structural Dynamics of Carotenoids and Charge Transfer Systems

by

Aaron Justin Van Tassle

Abstract

Excited State Structural Dynamics of Carotenoids and Charge Transfer Systems

by

Aaron Justin Van Tassle

Doctor of Philosophy in Chemistry

University of California, Berkeley

Professor Graham R. Fleming, Chair

This dissertation describes the development and implementation of a visible/near infrared pump/mid-infrared probe apparatus.

Chapter 1 describes the background and motivation of investigating optically induced structural dynamics, paying specific attention to solvation and the excitation selection rules of highly symmetric molecules such as carotenoids.

Chapter 2 describes the development and construction of the experimental apparatus used throughout the remainder of this dissertation.

Chapter 3 will discuss the investigation of DCM, a laser dye with a fluorescence signal resulting from a charge transfer state. By studying the dynamics of DCM and of its methyl deuterated isotopomer (an otherwise identical molecule), we are able to investigate the origins of the charge transfer state and provide evidence that it is of the controversial twisted intramolecular (TICT) type.

Chapter 4 introduces the use of two-photon excitation to the S_1 state, combined with one-photon excitation to the S_2 state of the carotenoid β-apo-8’-carotenal. These investigations show evidence for the formation of solitons, previously unobserved in molecular systems and found only in conducting polymers

Chapter 5 presents an investigation of the excited state dynamics of peridinin, the carotenoid responsible for the light harvesting of dinoflagellates. This investigation allows for a more detailed understanding of the importance of structural dynamics of carotenoids in light harvesting.

Chair Date

For my parents.

“As much as I don’t wanna spoil my reputation as a do nothing slacker, I will not hesitate to beat you senseless”

-Grif

Table of Contents

1. Introduction

2. Design and Implementation of Femtosecond Electronic Pump, Structural Probe Instrument

3. Investigation of the Excited State Structure of DCM via Ultrafast Electronic Pump / Vibrational Probe

4. Excited State Dynamics of β-apo-8'-carotenal: An Ultrafast Electronic and Vibrational Study

5. Excited State Structural Dynamics of the Charge Transfer State of Peridinin

5.3 Experimental

List of Figures

1. Chapter 1

2. Chapter 2

3. Chapter 3

4. Chapter 4

5. Chapter 5

List of Tables

3. Chapter 3

4. Chapter 4

5. Chapter 5

Acknowledgement

First and for most I'd like to thank Graham for giving me the means and freedom, some times a little too much freedom, to complete the work for my dissertation. Next most important are his assistants Kathy Demerdjian, Tiffaney Dressen, and Lisa Torres, who helped make sure I got a pay check every month and placed all the thousands of orders I had to place, and track them down for me when they get lost. Of course there are my partners in (Room 3) crime, Dula Parkinson, Bardley Prall, Hohjai Lee, Matt Prantil, who joined me on Team-IR once I had completed the initial experiments on DCM, and of course the newest recruit to Team-IR, Jacqui Burchfield, don't let Matt corrupt you too much. Id like to thank Ying-Zhong Ma, his breadth of knowledge and experience never ceased to amaze me, and whose children always laughed at group parties because we called him Ma. I'd also like to thank Infrared Associates, for not knowing how to program in C and necessitating the reverse engineering of their Labview drivers to get their hardware working; I would also like to thank them for providing a "data acquisition system" PC which was only powerful enough to become the room 3 music server, and in that role it provided hours of enjoyment during the long weekends reprogramming their drivers, whose efficiency was increased by more than two orders of magnitude when written in C than Labview (so much for "once you try Labview you'll never turn back" Andrew).

I owe Abbas Rizvi a lot, since he helped me come up with ideas to get through graduate school after I decided to not continue the research on fifth order Raman when Laura left. Of course all the other people that I worked directly with in my first few years: Xanthipe Jordanides, who first worked with me in lab when I arrived, Hugues

Mesnil, Laura Kaufman and Prof. Larry Ziegler, all three I worked on fifth order Raman with; Harsha Vaswani, who was my coffee buddy turned friend after the daily Fleming group coffee breaks ended, those ten minutes a day provided a necessary break from work and a place to express my frustration with all sorts of things. And of course I would like to thank my friends outside of work, Dan Horner, Ben Messer, and Brad Prall. You guys got me back into board games, and got me hooked on the Xbox. I never would have thought I would be into video games, and I blame you guys for getting me hooked, but in a good way. On that same note, I'd like to extend my sincerest gratitude to Xbox buddies, Brian "Pythonista" Almond, Aubyn "MeeMoos" Reyes, Co "Alsacien" Nguyen, and Sky "Skycube" Ortiz, and the rest of the 2old2play.com people, who helped me unwind and decompress, allowing me get through graduate school with my wits intact.

There are of course all the people who helped proof read this document, especially Greg Engel. Lastly I want to thank all of the member of the Fleming group past and present: Tomas Mancal, Donatas Zigmantas, Tom Avenson, Tae Ahn, Yuan-Chung Cheng, Elizabeth "Dazzle" Read, Matt "#2" Graham, Tessa Calhoun, Gabriella Schlau-Cohen, Igor Stiopkin, Andrei Pisliakov, Tobias Brixner, Nancy Holt, Jens Stenger, Patty Linden, Joerg Zimmermann, Gregor "GFP" Jung, Cherri Hsu, Ana Damjanovich who provided me a floor to sleep on when I first arrived in Berzerkley, Ritesh Agarwal, and Mino Yang. To anyone else I forgot to mention by name, I apologize, as this has been a long and arduous process, thank you.

Chapter 1: Introduction

1.1 Introduction

Excited state processes surround us and affect us every day of our lives: phosphors of our televisions fluoresce after being excited by an electron and further excite the pigments in our eye enabling vision, and photons of light are absorbed by trees highly evolved photosynthetic apparatus that as a byproduct produce the oxygen we need to survive. These processes occur on very short timescales, only few hundred femtoseconds (1 fs = $1*10^{-15}$ seconds, one millionth of a billionth of a second) in many cases.

The development of laser systems capable of producing pulses with durations on the order of femtoseconds allows the study of these fast physical dynamics.[1, 2] In this dissertation, I explore the structural changes that occur during the first few hundred picoseconds that follow excitation of a molecule. This chapter will outline the background and motivation necessary to understand the ideas presented.

1.2 Solvation

To understand the importance of structural dynamics to the study of chemistry, one first needs to understand the concept of solvation. In a simple solution there are two components, the solute and the solvent. If we dissolve a tablespoon of sugar in a glass of water the sugar is the solute and water is the solvent. Figure 1.1 shows a schematic representation of a solute molecule (colored in green) in a polar solvent. The solvent molecules, shown as the oval shapes, are colored red and blue; the red side indicates the part of the molecule possessing positive charge while the blue side of the solvent

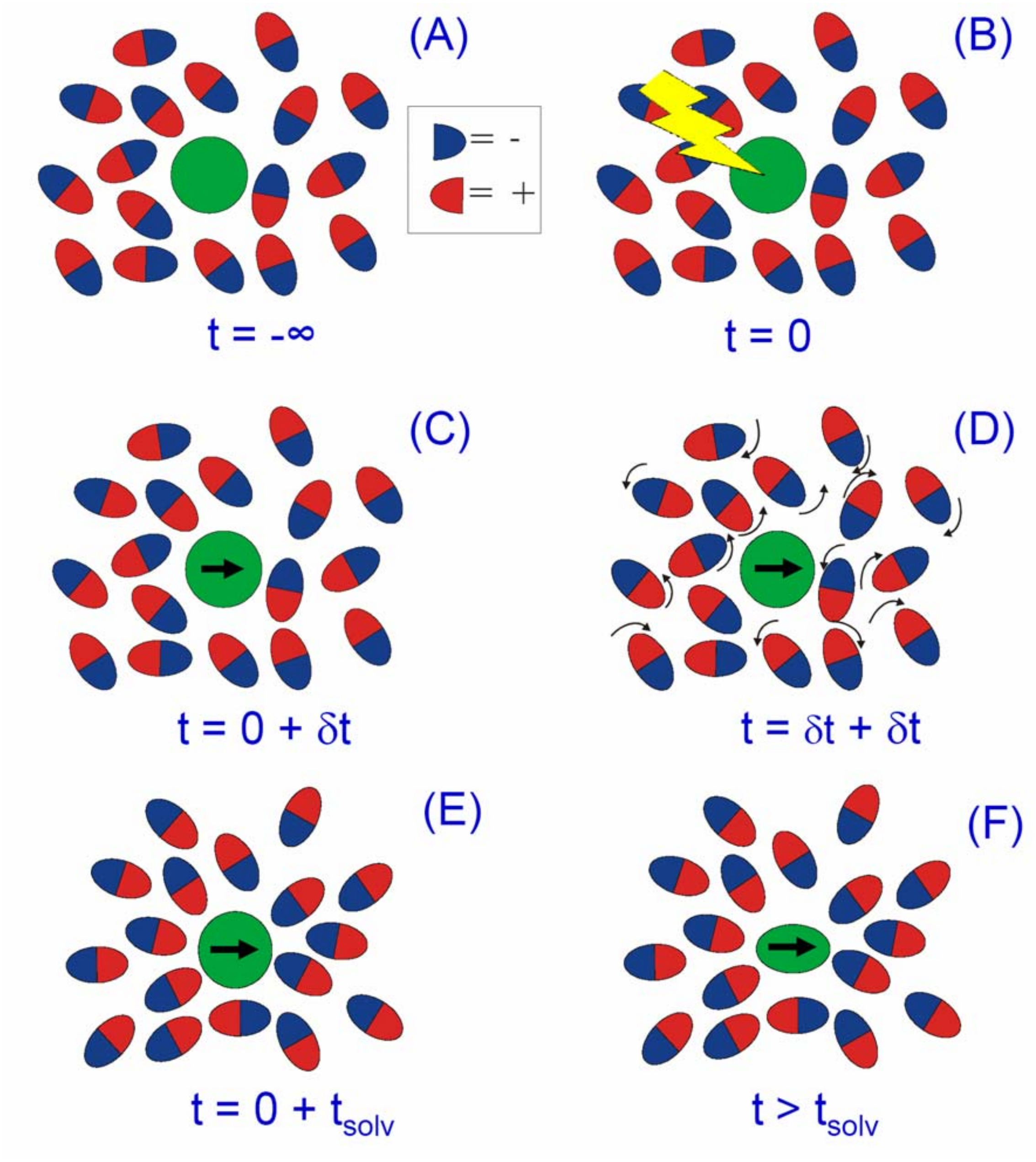

Figure 1.1: Schematic representation of solvation before and after absorption of a photon

molecule represents the negative charged end of the molecule. These solvent molecule are polar, that is their electric charge is not distributed evenly. These solvent molecules can be pictured as little, very weak, magnets. Each frame of the figure represents a different point in time. In the first frame Figure 1.1 (A) the oval, polar, solvent molecules are randomly oriented with respect to the green solute molecule, which at this point possesses no dipole moment. A dipole moment is caused by uneven distributions of electrons; the solvent is the case possesses a permanent dipole moment. In (B), labeled t=0 we allow the solute molecule to absorb a photon of light, and at a infinitesimal time, δt, later (C) it has reached the excited state. The absorption of a photon is so fast that it can be assumed instantaneous, and an induced dipole moment, represented by the arrow, now appears. The length of the arrow represents the magnitude of the dipole moment and points towards the positive end of the molecule. Beginning when the molecule becomes dipolar, the solvent begins to respond (D) and reorient itself by rotating so that the negative ends of the solvent molecules point toward the positive ends of the solute and the positive portions of the solvent molecules orient toward the negative end of the solute. After the solvation time, a characteristic time for each solvent to achieve equilibrium with the newly polar solute, that depends on its shape, polarity, viscosity and how it interacts with itself, the solvent has become more ordered around the probe molecule (E). During this process the solute molecule can react to the increased order of the solvent molecules (F) and change its electronic structure and perhaps molecular shape; in the case of our pictured molecule, the dipole moment increases (denoted by the increased length of the arrow) and its shape changes in response. While this cartoon is clearly an overly simplified picture, it is useful in understanding the basics of solvation.

Figure 1.2 show the simplest potential energy diagram for the process described previously. In this picture, two electronic energy levels of a simple molecule are shown; S_0 represents the ground state of the molecule (the S indicates that the states are singlet states where there are no unpaired electrons in the molecule), and S_1 represents the first excited state. The horizontal lines in the individual states represent vibrational energy levels. In the current picture both energy levels are represented as harmonic potentials, and as such, the spacing between the vibrational energy levels are equal. All vertical arrows represent the absorption or emission of energy; in the context of our discussion, this energy is a photon of light. The length of the vertical arrows is proportional to the amount of energy the transition represents, hence the longer an arrow the more energy it represents and the shorter wavelength it possesses. The circled letters correspond to the part of Figure 1.1 that is occurring at that position. In general only vertical transitions from the center of the lowest vibrational level can occur. Consequently the absorption of the photon at point B put the molecule into a higher vibrational level of the excited state. Notice that instead of the molecule responding to the solvent reorganization by changing shape, it undergoes emission of a photon of longer wavelength with a lesser amount of energy. This extra energy is lost as thermal energy that is transferred to the solvent. The difference in energy between the absorbed photon and the emitted photon is called the Stokes shift, and provide information on the nature of the excited state. If, for example, the molecule in the excited state has a large dipole moment it can undergo solvatochromism, the color changes with solvent

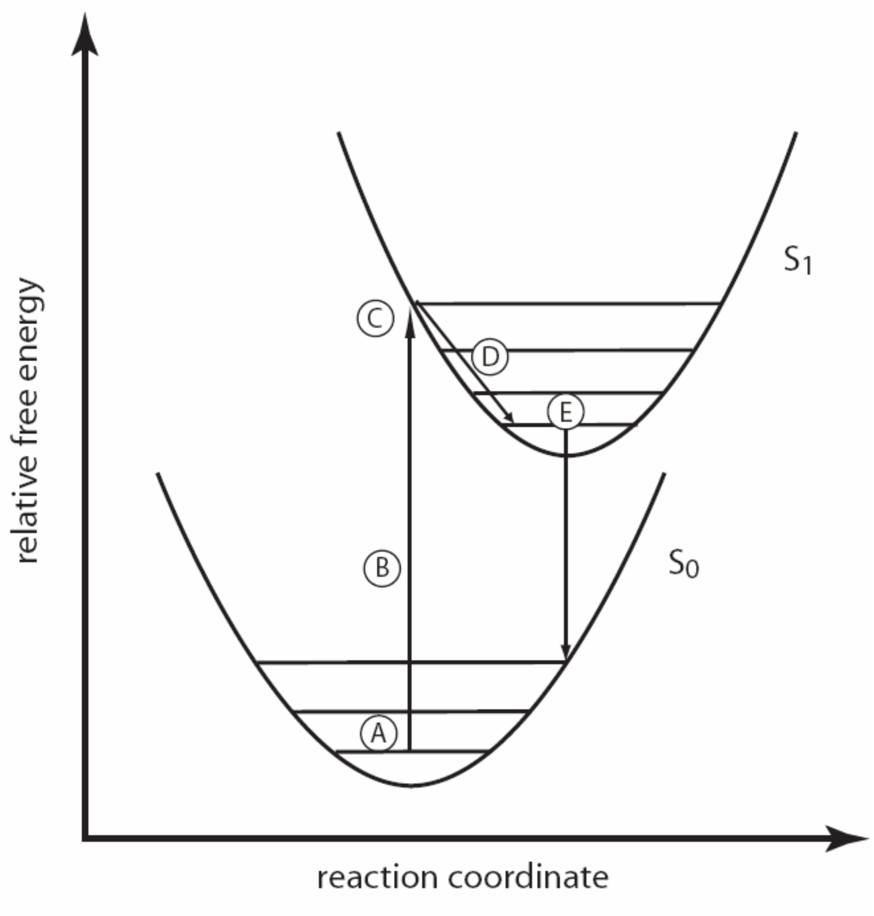

Figure 1.2: Potential energy diagram of the progression shown in Figure 1.1

polarity. Solvatochromism is caused by the interaction of solvents of differing polarity on the probe molecule. In more polar solvents the Stokes shift of a molecule with increased dipolar character in the excited states increases. The amount of change in a molecule's dipole moment can be extrapolated from a plot of the slope of Stokes shift versus solvent polarity.[3-5]

1.3 Excited State Charge Transfer

Now that we have covered the basics of solvation, lets move on to a more applicable example. Figure 1.3 displays a potential energy diagram for the case in which a molecule undergoes a change in the excited state. Examining the S_1 surface in this figure you will notice that instead of the simplest case of a single harmonic potential from Figure 1.2 the excited state now is composed of two minima. These two minima represent different configurations that can exist at different values of the reaction coordinate. Such configurations can be differently solvated molecules or a molecule that has changed its structure. Following excitation from the ground state (A), the molecule can either relax back to the ground state fluorescing a photon of the same color (B), or, depending on how much excess energy is left from the absorption of the photon and the height of the barrier, it can pass over the small barrier between the two conformations (C). Once the molecule crosses the barrier it relaxes down to the lowest vibrational level (D) by redistributing excess energy within its structure or into the local solvent molecules. The lifetime of a molecule after this sort of barrier crossing, such as the case of DCM discussed in chapter 3, can increase into the nanosecond ($1*10^{-9}$ second) range before it relaxes to the ground state ground state by emitting a photon (E)

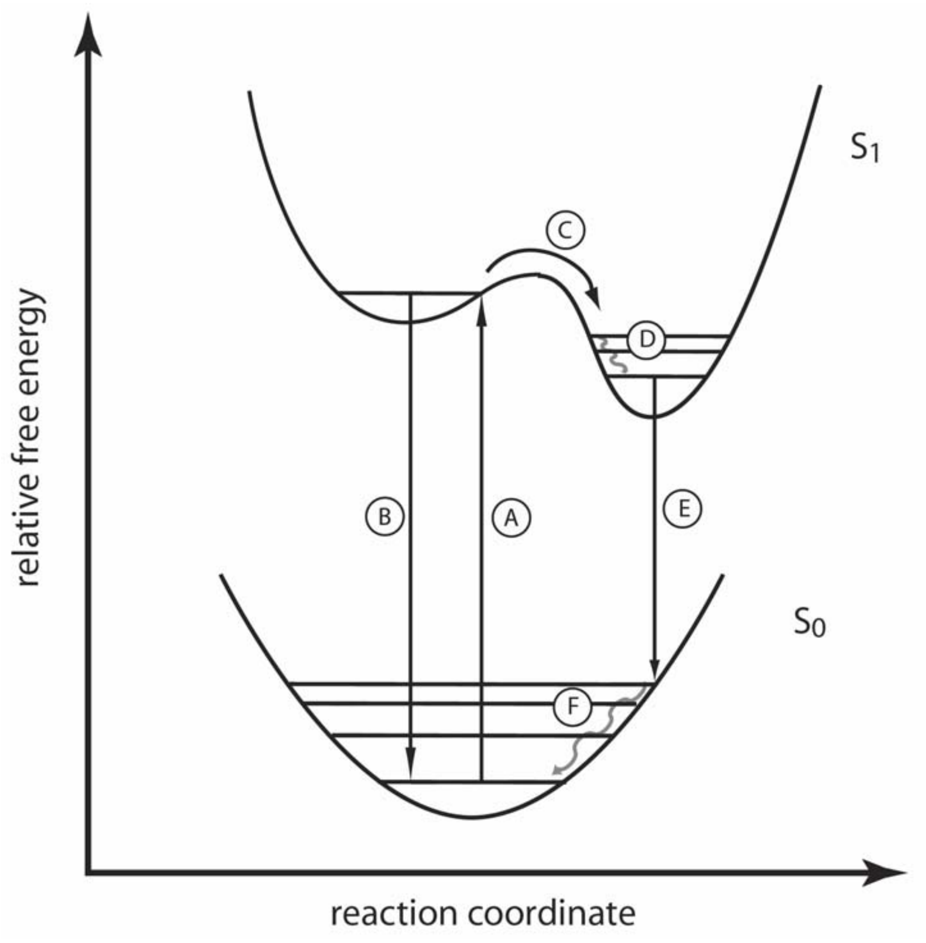

Figure 1.3: Potential energy diagram of a molecule undergoing structural evolution in the excited state

or relaxes non-radiatively back to the starting point (F). In addition to the fluorescence that occurs at point (E) in the figure, the molecule could undergo excited state chemical reactions that permanently change its properties. This comes into play in the design and application of organic light emitting diodes (OLEDs), which can use DCM (discussed in Chapter 3) and its derivative compounds as the red component. The problem with OLEDs is that because of competing processes, reactive deactivation and fluorescence, they have very short usable lifetimes. Blue OLEDs (blue is the highest energy light produced by OLEDs) are by far the least stable and in some cases their usable lifetimes are as short as 5000 hours, much less than LCD or plasma display technologies. In order to understand the process of photochemical deactivation that will enable the development of a new generation of OLED compounds, a detailed understanding of the structural dynamics involved is required, thus allowing targeted chemical modification to extend the usable lifetimes of these devices.

1.4 Electronic and Infrared Spectroscopy

All the experiments described in this dissertation are known as pump-probe experiments. A simple schematic for pump-probe is displayed in Figure 1.4. In a pump-probe experiment two light sources are used, in our case short laser pulses on the order of 100 femtoseconds. The two beams are crossed, overlapped in space and time, in the sample of interest. The more intense beam is called the pump, and the weaker beam is called the probe. A common case is to have the probe beam be ten times weaker than the pump beam. In the probe beam, we install a very accurate computerized positioning stage. This allows us to change the time delay between the

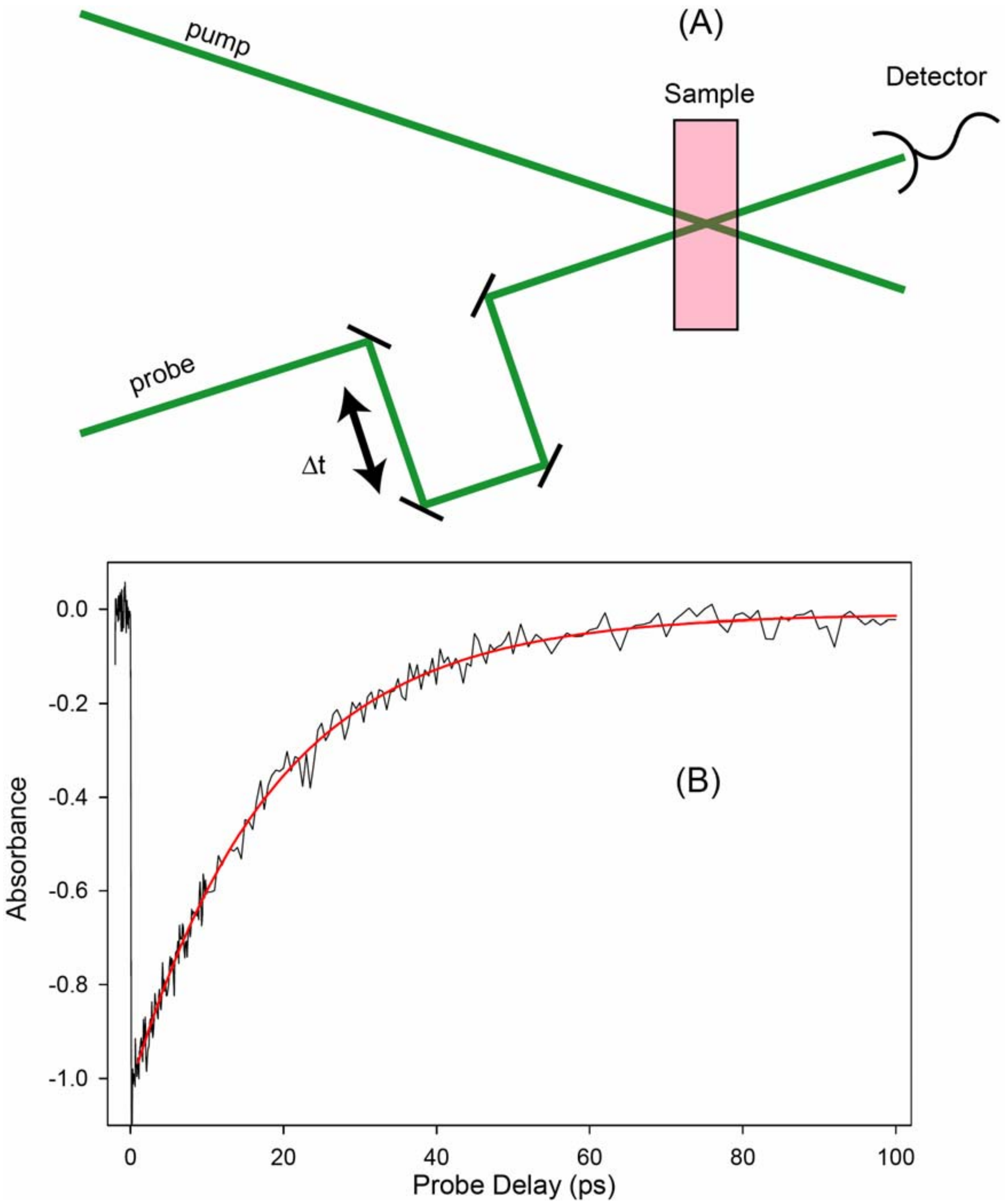

Figure 1.4: Simple diagram of a pump-probe experiment and an experimental trace corresponding to ground state recovery for the molecule β-apo-8’-carotenal, discussed in chapter 4.

beams, due to the constant speed of light.[6] For example if the two beams are exactly synchronized (so that they impinge on the sample at exactly the same time) and then we increase the path length of the probe by moving the stage back by 1 micron (0.001 millimeters) thereby increasing the amount of time it takes for the probe to reach the sample by 6.6 femtoseconds. We scan the probe beam in time and record the change in intensity of the probe beam with time delay. In the most simple case, the two beams are the same color, and we monitor the amount of time it takes to recover the original absorption. Figure 1.4 (B) presents a graph of a compound that will be discussed in chapter 4. At negative times, when the probe beam comes before the pump beam, there is no change in probe intensity due to the pump. At time zero, when the pump and probe arrive at exactly the same time, the sample absorbs a photon from the pump beam and then less probe light is absorbed by this molecule (once a molecule is no longer in the ground state it does not absorb the same color photon). This is seen as a decrease in absorbance as seen in Figure 1.4 (B). As we then increase the delay between the pump and probe so that the probe comes later and later, the change in the amount of probe beam absorbance slowly returns to 0. In the case of the trace shown, the normal absorbance of the sample returns on a single 18 picosecond timescale. This corresponds to how long it takes for the molecules excited by the pump beam to return to the ground state. This measurement is called ground state recovery. There are several other contributions that can complicate this signal, however. Figure 1.5 (A) shows an energy level scheme for electronic pump probe (both beams are in the visible region 400 to 800 nm). The arrows in red represent the probe beam; those pointing up would

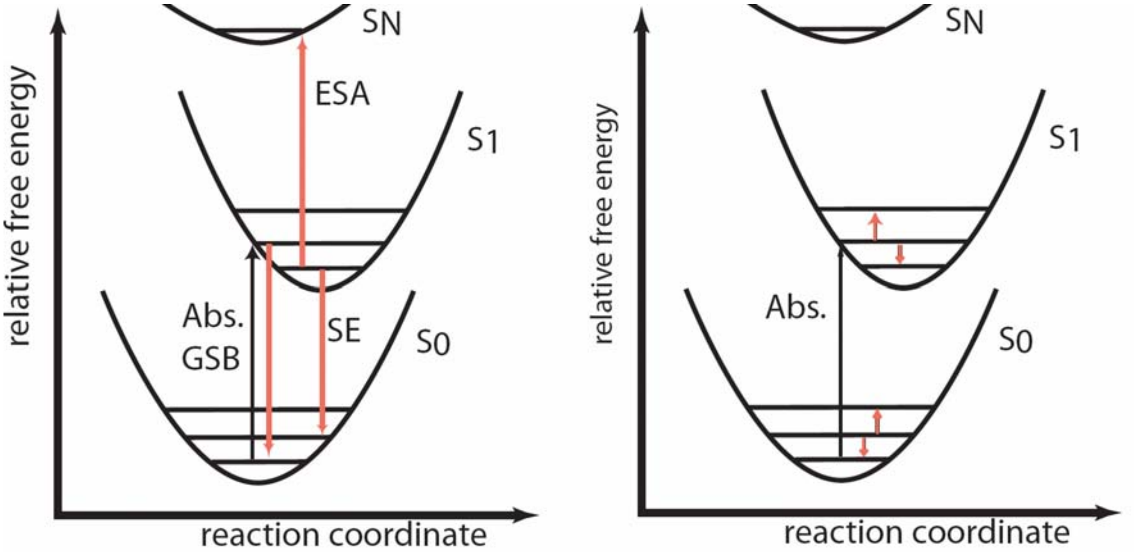

Figure 1.5: Comparison of allowed transition when changing form electronic to vibrational probe.

cause an increase in absorbance while downward facing arrows would give negative signals. After absorption of a photon (represented by the upward black arrow), you can measure signals caused by ground state recovery (GSR), excited state absorption (ESA), and stimulated emission (SE) can arise. Electronic transitions of these types are very broad, spanning hundreds to thousands of wavenumbers (cm^{-1}) and, depending on the shape of the potential surfaces can either occur at the same position/color (as in the case of absorption and ground state recovery), or be very close in wavelength, overlapping and complicating analysis of the spectrum. The same schematic diagram for an infrared probe, where we simply replace the visible probe with a mid-infrared beam is shown in Figure 1.5 (B). The use of an infrared probe is of interest because absorptions in the mid-IR (3-10 μm) are due to molecular vibrations. So instead of giving us information about how the electronic structure changes, we gain insight into the structural changes that occur following excitation, allowing direct observation of the dynamics discussed in the previous sections.

Following absorption of a photon you can observe ground state bleach in S_0 and excited state absorption in S_1, but since the photons have much less energy (on the order of 1000 to 3000 cm^{-1} for IR compared to greater than 12000 cm^{-1} in the visible) they cannot cause transitions between electronic states. The widths of transitions in the infrared are much narrower as well (~10 cm^{-1} instead of 100-1000s for electronic transitions) making it much easier to separate the contributions from different signals. Collecting the data the same way as described in the electronic case, we can build a picture of how the molecule changes shape in the excited state, by using theoretical calculations and comparing with the ground state vibrational spectrum.

1.5 Symmetry and Selection Rules

Special cases exist, for molecules that are highly symmetric, where not all transitions are allowed. Figure 1.6 shows several compounds including peridinin and β-apo-8’-carotenal, which are discussed in the last two chapters of this dissertation, as well as β-carotene, and 1,6-diphenyl-1,3,5-hexatriene. Carotenoids are large (35-40 carbon atoms) polyene chains, sometimes terminated by rings, and occur in plants, other photosynthetic organisms such as algae. β-carotene is probably the most widely recognized carotenoid and belongs to the highest symmetry group of carotenoids. This symmetry group is C_{2h} and is the group that most carotenoids belong to; they possesses: a two fold rotational symmetry axis, a C_2 axis, about which you can rotate about the center of the molecule two half turns to reach the starting position; a horizontal mirror plane, a σ_h plane, where you can imagine cutting the molecule in half in the plane of the paper and you would produce two identical pieces, and a point of inversion, known as an i operation that corresponds to rotating once about the C_2 axis and reflecting about the σ_h mirror plane. For the case of simplicity we will use a smaller molecule 1,6-diphenyl-1,3,5-hexatriene, as an example. This hexatriene belongs to the same point group as β-carotene, C_{2h}, and so will have all the same selection rules.

Figure 1.7 shows the structure of 1,6-diphenyl-1,3,5-hexatriene, its infrared (in red) and Raman, where a photon undergoes two interactions and its wavelength is shifted by a vibrational frequency, (shown in blue) spectra as well as the character table, a tool that

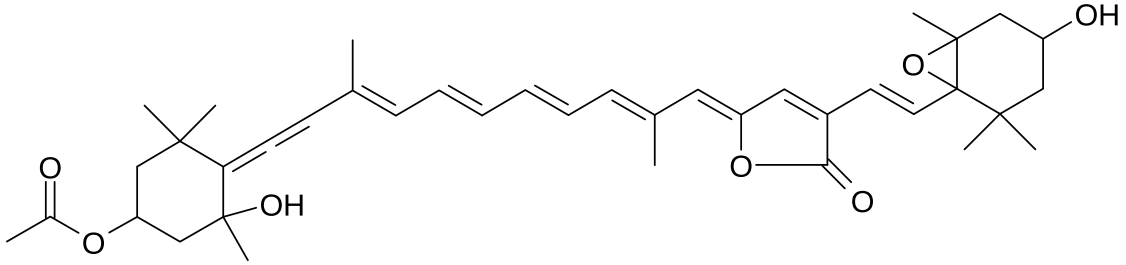

Peridinin

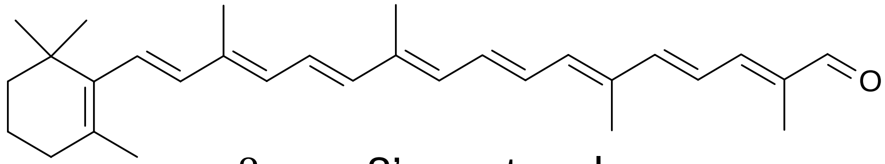

β-apo-8’-carotenal

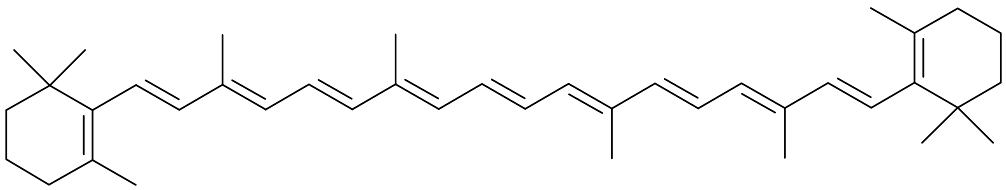

β-carotene

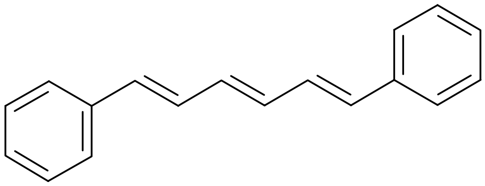

1,6-diphenyl-1,3,5-hexatriene

Figure 1.6: Structure of three carotenoids, peridinin, b-apo-8’-carotenal and β-carotene and 1,6-diphenyl-1,3,5-hexatriene, shown as a model for highly symmetric molecules.

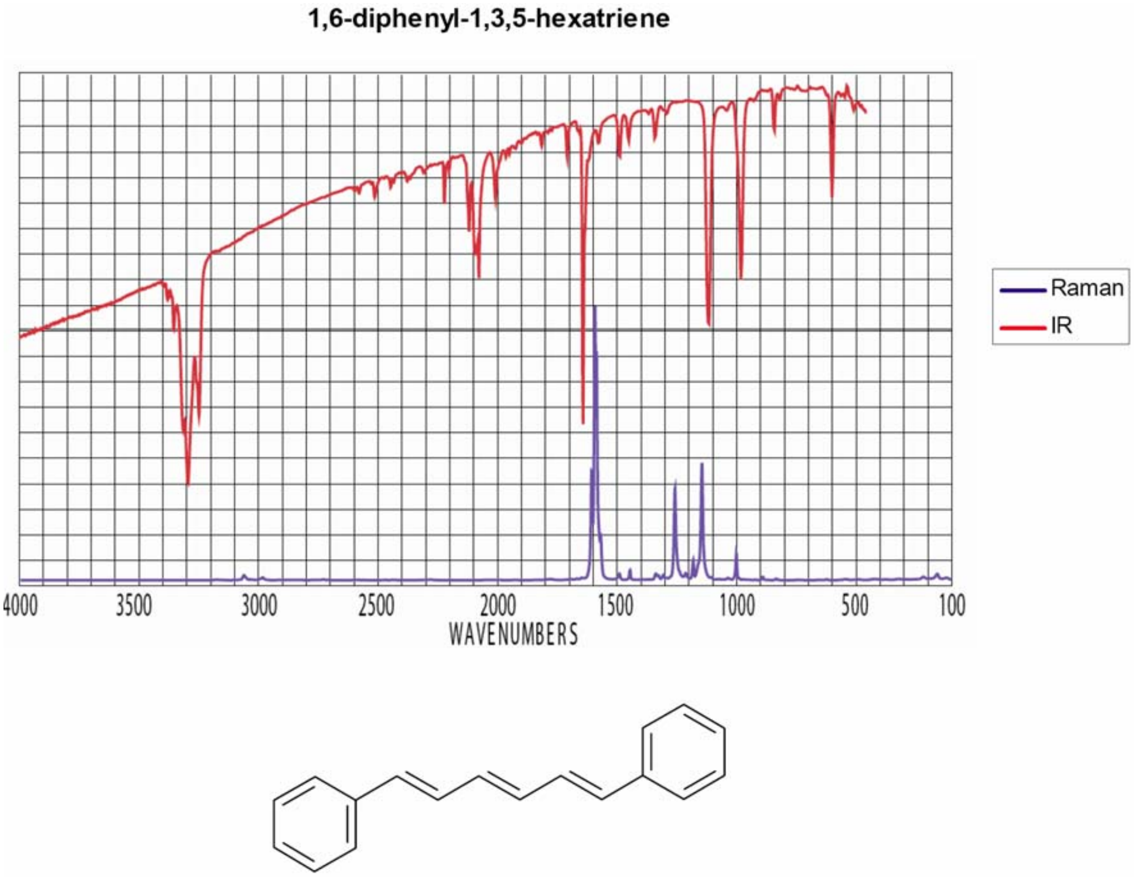

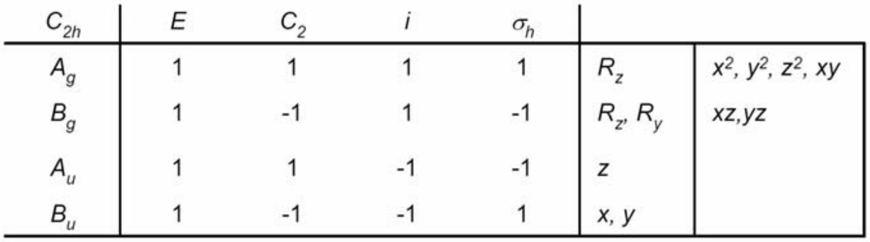

C_{2h}	E	C_2	i	σ_h		
A_g	1	1	1	1	R_z	x^2, y^2, z^2, xy
B_g	1	-1	1	-1	R_z, R_y	xz, yz
A_u	1	1	-1	-1	z	
B_u	1	-1	-1	1	x, y	

Figure 1.7: Infrared and Raman spectra of 1,6-dipheny-1,3,5-hexatriene, its structure and the C_{2h} character table.

simplifies the mathematics involved with symmetry operation, for the C_{2h} point group. The farthest left column at the top contains the name of the point group, C_{2h} in this case, and the rest of the column is populated with all the different symmetry representations that are possible. The A_g transition for example would represent a completely symmetric state. The state can be either an electronic state with transitions in the visible region, a vibrational state corresponding to changes in vibrational energy levels in the infrared region, or even a rotational state with absorption in the microwave region.

The top row represents each of the symmetry operation E, the identity operator where nothing happens; C_2, rotation about the center of the molecule by 180°; σ_h the mirror plane in the same plane as the paper; and the inversion operator I which is the combination of σ_h and C_2. The next column represents the first order combinations of Cartesian coordinates. R_x R_y and R_z represent infinitesimal rotations that transform as B_g, B_g and A_g respectively. The Cartesians x, y, and z transform as B_u, B_u and A_u respectively and are components of the dipole moment operator μ, which is represented as a vector in equation 1.1. To know if a transition is allowed, take the irreducible

$$\mu = \begin{pmatrix} x \\ y \\ z \end{pmatrix} \qquad eq\,1.1$$

representation of the final state times the irreducible representation of the dipole moment operator and multiply that by the irreducible representation of the initial state. For example, the symmetry of the ground state of 1,6-diphenyl-1,3,5-hexatriene, S_0, has symmetry that transforms as A_g. The first excited state, S_1, also transforms as A_g, and the second excited state transforms as B_u. The calculation that we need to do to know if the transition from S_0 to S_2 is one-photon allowed is $A_g * \mu * B_u$; if the piecewise product contains the totally symmetric representation, A_g, the transition is allowed. Looking on the character table and filling in the appropriate character we get equation 1.2. If we just consider the top line of the μ tensor, the x transition, and multiply them together we would get $\begin{pmatrix} 1 & 1 & 1 & 1 \end{pmatrix}$ which is the same as the A_g irreducible

$$\begin{pmatrix} 1 & 1 & 1 & 1 \end{pmatrix} * \begin{pmatrix} 1 & -1 & -1 & 1 \\ 1 & -1 & -1 & 1 \\ 1 & 1 & -1 & -1 \end{pmatrix} * \begin{pmatrix} 1 & -1 & -1 & 1 \end{pmatrix} \qquad eq.1.2$$

representation and would be allowed by a single photon transition. If we instead check the transition from S_0 to S_1 we would find the product is A_u and would not be allowed by one photon. For a two photon transition we would multiply by μ twice and the operation would be $A_g * \mu * \mu * A_g$. If you carried out the operation you would find that it comes out as A_g making it allowed by two-photon absorption and that the transition from S_0 to S_2 would not be allowed.

1.6 Carotenoids and Photosynthesis

Carotenoids are ubiquitous in photosynthesis. They play important roles in light harvesting and photoprotection[7-11]. As part of the xantholphyll cycle they protect plants from overexposure[12]. Carotenoids additionally prevent triplet chlorophyll formation by quenching toxic singlet oxygen[13]. Figure 1.8 displays the standard picture for a photosynthetic system. The carotenoid absorbs a photon of energy into the second excited state (as discussed above one photon transitions to the S_1 state are not allowed).

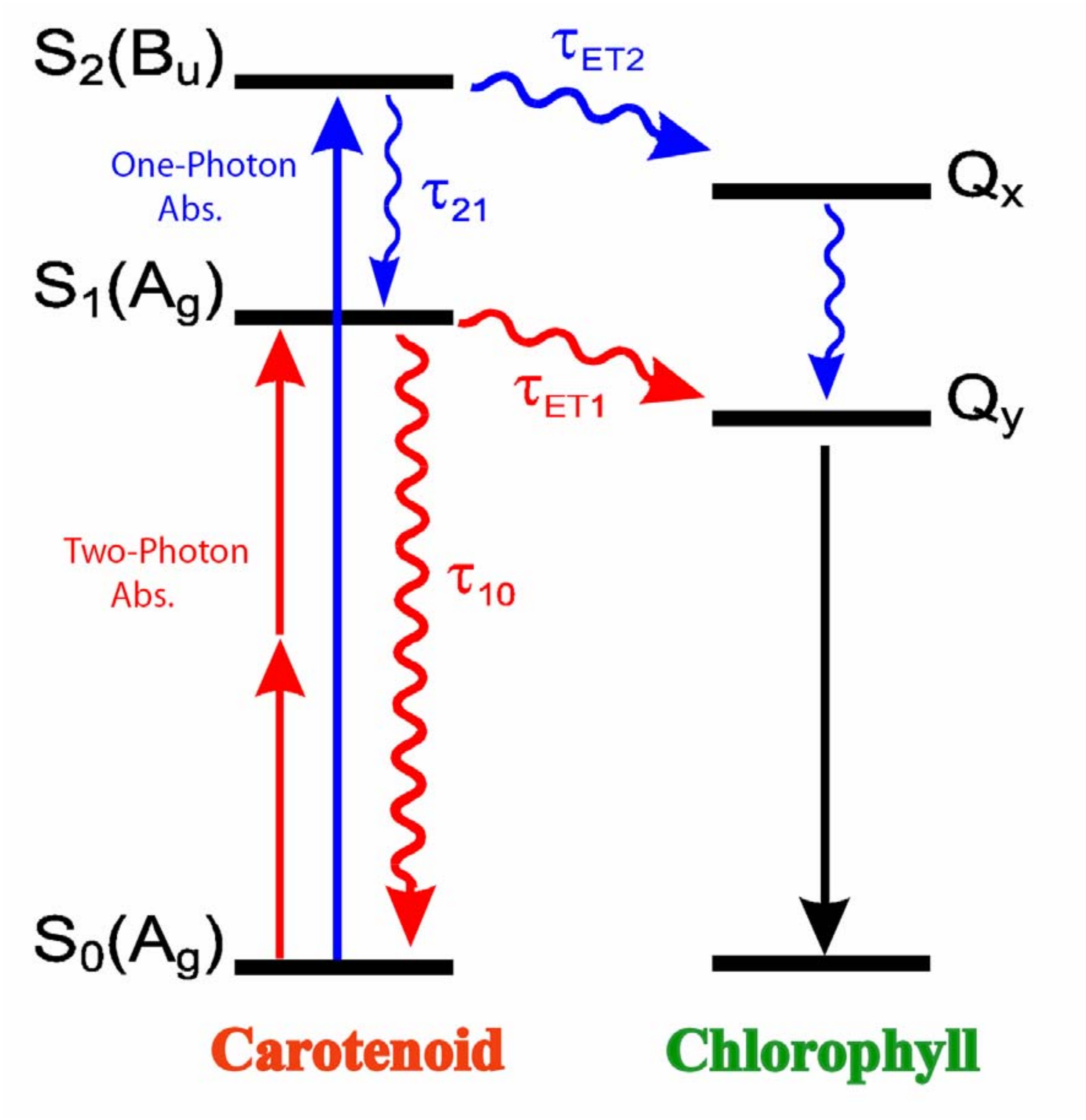

Figure 1.8: Jablonski diagram of energy transfer between carotenoids and chlorophyll in photosynthesis. Straight arrows represent absorption (upward pointing), or emission (downward pointing). Curved arrows represent non radiative transitions

Energy then redistributes itself in many ways; non radiative transitions are represented by the curved arrows. There can be energy transfer directly from the S_2 state to the Q_x state of chlorophyll; in some cases, this is the dominant pathway. From the S_2 state there is also fast relaxation into the S_1 state followed by energy transfer to the Q_y band of chlorophyll. The last possibility is that the carotenoid relaxes back to ground state without transferring its energy. For the case of peridinin-chlorophyll protein (PCP), discussed in chapter 5, nearly all the energy is transferred to the chlorophyll. More than 50 % of the energy transferred to the chlorophyll actually comes from the S_1 state in PCP.[14] This fact makes understanding the dynamics in the S_1 state, which cannot be accessed directly, extremely important to understanding the function of peridinin as a light harvester. The most simple way to study the S_1 state is excite the S_2 state with one photon and then wait for the fast relaxation to S_1 where we can probe the dynamics. The problem with this approach is that by exciting to S_2 the molecule relaxes to the S_1 state with huge amounts of excess energy (about 5000 cm^{-1} worth; for comparison the amount of thermal energy in a molecule at room temperature is only 200 cm^{-1}), which can complicate the results from an infrared probe. In order to avoid this extra energy, as discussed in a later chapter, you can populate the carotenoid by using two photons of lesser energy and study the dynamics without the excess energy.

1.7 Dissertation Outline

The remainder of this dissertation is organized as follows:

Chapter 2 describes the development and construction of the experimental apparatus used throughout the remainder of this dissertation.

Chapter 3 will discuss the case of DCM, a laser dye with a fluorescence signal resulting from a charge transfer state. By studying the dynamics of DCM and of its methyl deuterated isotopomer (an otherwise identical molecule), we are able to investigate the origins of the charge transfer state and provide evidence that it is of the controversial twisted intramolecular (TICT) type.

Chapter 4 introduces the use of two-photon excitation to the S_1 state, combined with one-photon excitation to the S_2 state of the carotenoid β-apo-8'-carotenal. These investigations show evidence for the formation of solitons, previously unobserved in molecular systems and found only in conducting polymers

Chapter 5 is an investigation of the excited state dynamics of peridinin, the carotenoid responsible for the light harvesting of dinoflagellates. This investigation allows for a more detailed understanding of the importance of structural dynamics of carotenoids in light harvesting.

1.8 References

1. R. L. Fork, B. I. Greene and C. V. Shank, *Applied Physics Letters*, 1981, **38**, 671-672.
2. M. T. Asaki, C. P. Huang, D. Garvey, J. P. Zhou, H. C. Kapteyn and M. M. Murnane, *Optics Letters*, 1993, **18**, 977-979.
3. E. Lippert, *Z. Naturforsch., A: Phys. Sci.*, 1955, **10**, 541-545.
4. N. Mataga, Y. Kaifu and M. Koizumi, *Bull. Chem. Soc. Jpn.*, 1956, **29**, 465-470.
5. Y. Ooshika, *J. Phys. Soc. Jpn.*, 1954, **9**, 594-602.
6. A. Einstein, *Ann. Phys.-Berlin*, 1912, **38**, 355-369.

7. C. S. Foote, *Science*, 1968, **162**, 963-&.

8. H. A. Frank and R. J. Cogdell, *Photochemistry and Photobiology*, 1996, **63**, 257-264.

9. H. A. Frank, C. A. Violette, J. K. Trautman, A. P. Shreve, T. G. Owens and A. C. Albrecht, *Pure and Applied Chemistry*, 1991, **63**, 109-114.

10. T. Ritz, A. Damjanovic, K. Schulten, J. P. Zhang and Y. Koyama, *Photosynthesis Research*, 2000, **66**, 125-144.

11. H. van Amerongen and R. van Grondelle, *J. Phys. Chem. B*, 2001, **105**, 604-617.

12. I. Szabo, E. Bergantino and G. M. Giacometti, *Embo Reports*, 2005, **6**, 629-634.

13. R. Schmidt, *Journal of Physical Chemistry A*, 2004, **108**, 5509-5513.

14. D. Zigmantas, R. G. Hiller, V. Sundstrom and T. Polivka, *Proc. Natl. Acad. Sci. U. S. A.*, 2002, **99**, 16760-16765.

Chapter 2: Design and Implementation of Femtosecond Electronic Pump, Structural Probe Instrument

2.1 Abstract

This chapter presents a laser system capable of producing <40 fs pulses centered at 800 nm providing ~400 μJ per pulse. This beam is used to pump 1) a mid-infrared (mid-IR) optical parametric amplifier (OPA) capable of producing a continuously tunable beam between 3000 and 7000 nm of ~100 fs and 1-2 μJ per pulse, and 2) used as either the fundamental, second harmonic, or seed of a TOPAS (Quantronix) near-IR optical parametric amplifier (OPA) which produces tunable pulses between 1150 and 2600 nm with pulse duration of ~60 fs and combined energy of signal and idler of ~20 μJ.

2.2 Introduction

Femtosecond light sources require complex optical components to allow for generation, amplification, and wavelength conversion of pulses with durations in the femtoseconds regime. Also required is long term stability as for many experiments, there are multiple time delays to be scanned, various spectral regions that need to be collected. Overall the infrared transient signal can require several hours to acquire. As solid state lasers have progressed, the use of dye lasers to produce different pump wavelength have become less common. The stability and relative decrease in power consumption for solid state laser systems allow their operation continuously for weeks without changes in performance. The additional need for multiple powerful compressed femtosecond pulses at different frequencies for non degenerate spectroscopies like the visible pump and infrared probe technique discussed in this dissertation require a carefully planned experimental layout to allow the most efficient data collection.

2.3 Femtosecond Pulse Source

The ultrafast pulses train used in these experiments were generated by several sources. The first is based on the common mode locked Ti:Sapphire oscillator pumped with a 5 W Coherent Verdi. Initial experiments on DCM were performed using this home built Ti:Sapphire oscillator based on the design of Asaki et al.[1, 2] This oscillator produced short pulses (~15 fs), at an 88 MHz repetition rate, which were used to seed the amplifier. This seed laser was later replaced with a commercial chirped mirror dispersion controlled Ti:Sapphire oscillator (Femtolasers Femtosource Compact Pro) which produced sub-10 fs laser pulses at a 76 MHz repetition rate. The Femtosource uses chirped mirrors instead of prisms to compensate for dispersion from the cavity. The schematic of both oscillators are shown in Figure 2.1.

Although recently available commercial femtosecond laser amplifiers have made considerable advancement, allowing for off-the-shelf systems with pulse durations around 40 fs, at the time of construction of this laser system the specification os the best commercial systems had 80 fs pulses for output energies on the millijoule level. The need for shorter pulses thus required the construction of a custom amplifier system. Our amplifier was made with a home built resonator and a modified kit-based stretcher and compressor (Kapteyn-Murnane Laboratories). The system uses a chirped pulse amplification scheme where the femtosecond seed pulse is

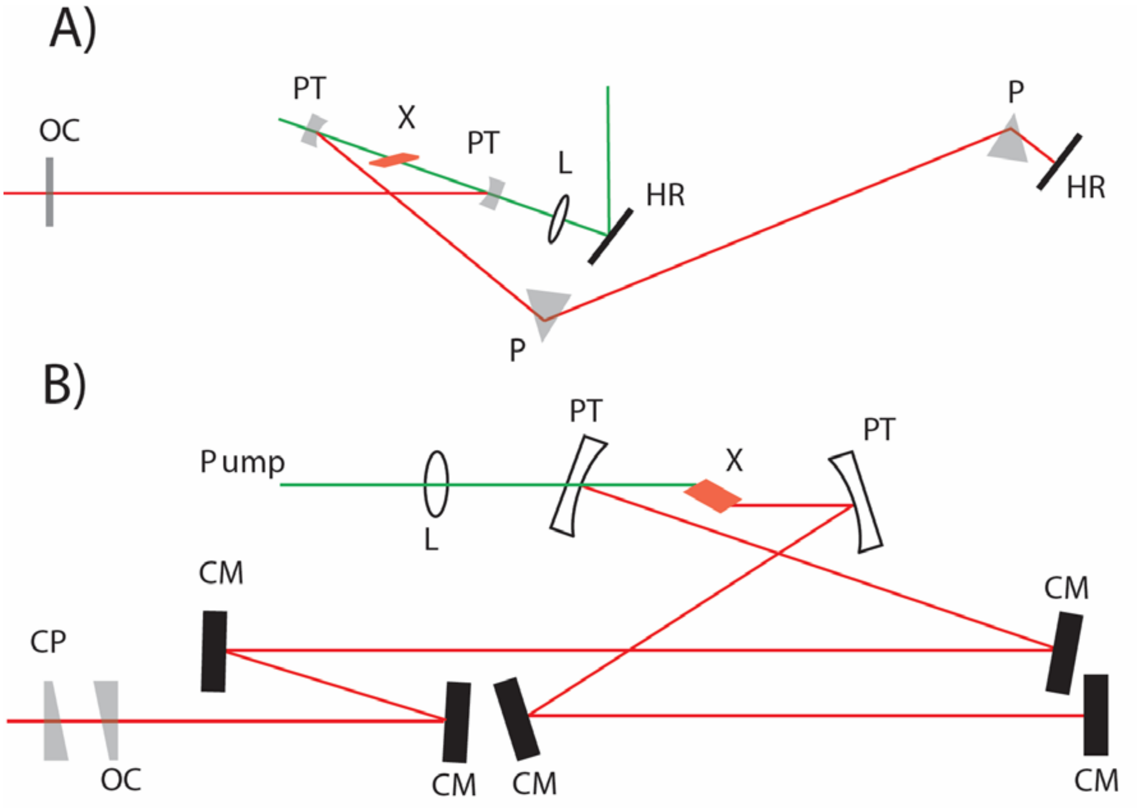

Figure 2.1 Optical schematic for A) standard Ti:Sapphire oscillator, and B) Femtosource Compact Pro oscillator. HR high reflector, P prism, X Ti:Sapphire Crystal, PT pump through mirrors, L pump focusing lens, CM chirped mirrors, OC output coupler, CP compensation plate.

stretched to hundreds of picoseconds, amplified from the nanojoule to the millijoule level, and compressed back to femtosecond duration.[3] The final output pulse duration is limited by the spectral width of the amplified, gain narrowed pulse, and the ability of the compressor to compensate for the phase induced by the materials in the amplifier.

The resonator was a V-shaped system with the layout as shown in Figure 2.2 along with all injection optics. The amplifier was pumped on axis with a Positive Light Evolution laser with ~6 watts of power reaching the crystal. Because of the poor mode quality of the pump laser, lenses marked as PL were used to decrease the focus size in the crystal by expanding it to approximately 5 cm in diameter using a 2 lens telescope before it is focused in the crystal with a 50 cm lens. The mirrors labeled PT are shortwave pass pump-through mirrors to allow for on-axis pumping. Pump light not absorbed by the crystal is focused back into the crystal with 50 cm radius mirror labeled PR. The maximum output power of the system is not increased by this but it does improve the efficiency, allowing us to reduce the number of round trips needed in the cavity. A thorough discussion of the calculation involved in constructing this amplifier can be found in the thesis of Bradley S. Prall.[4]

This amplifier system has been found to generate sub 40 fs pulses at a 1 kHz repetition rate with approximately 400 microjoule per pulse output energy centered at 800 nm. A characteristic autocorrelation trace, following compression, is shown in Figure 2.3. A 10 percent beam splitter is used to select a beam with enough power to pump a separate experiment. For example this 40 microjoule beam is sufficient to pump two visible optical parametric amplifiers necessary to conduct two color three pulse photon echo experiments covering much of the visible region.[4, 5]

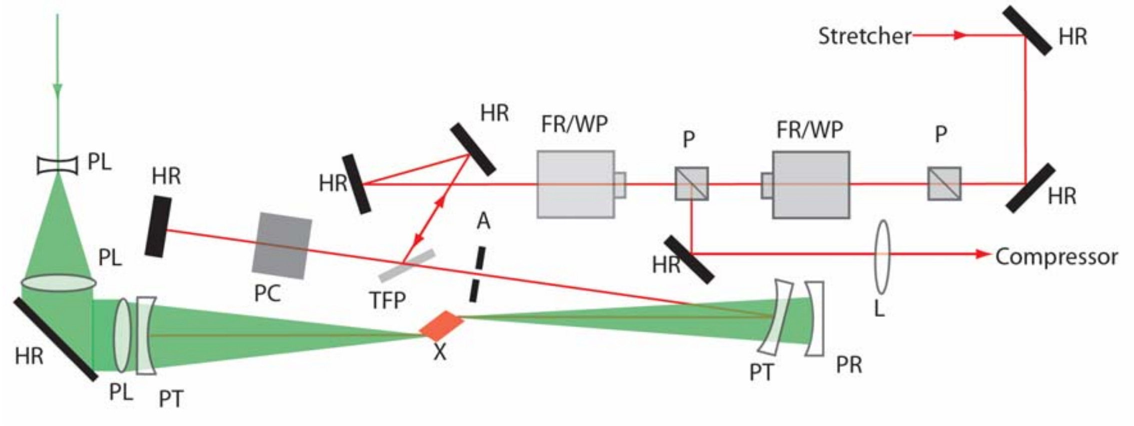

Figure 2.2 Optical layout for 1 kHz amplifier. PL lenses for adjusting pump laser focal spot size, PT pump through mirrors for laser cavity, X Ti:Sapphire crystal, PR curved mirror to reflect unabsorbed pump beam back through crystal, HR high reflector, A aperture for control of amplifier mode, TFP thin film polarizer, PC Pockels cell, FR/WP Faraday rotator and waveplate, P polarizer, L lens for collimation of amplified beam

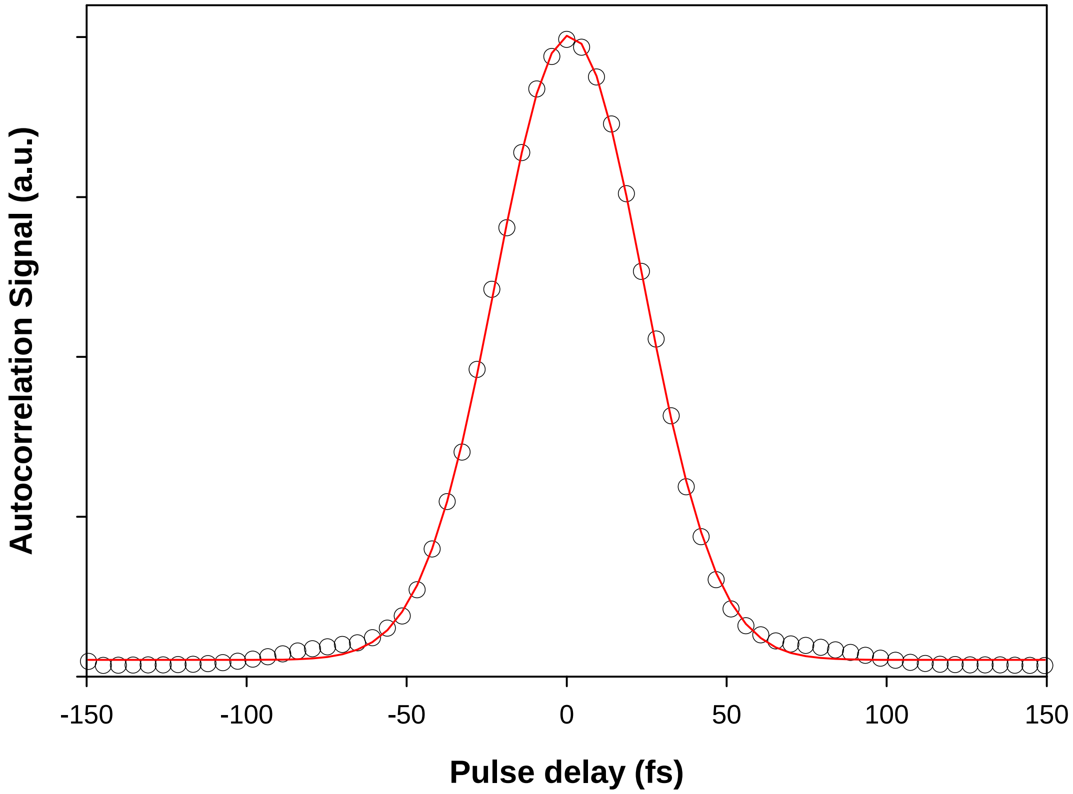

Figure 2.3 Regenerative amplifier intensity autocorrelation trace. Circles are experimental measurements. The red line is the 54 fs Gaussian fit to the data. The fit yields an intensity full width at half maxinum of 38 fs when assuming a Gaussian pulse shape.

The remaining amplifier power (~360 μJ) is split into two beams of equal power one being used as seed for the pump source, the other being used as the seed for the mid-infrared OPA discussed in the next section. For samples that required pump wavelengths of 800 nm the beam was polarization was rotated and controlled by a polarizer and half wave plate. For pump wavelengths of 400 nm the amplifier beam was doubled in a 0.1 mm β-barium borate crystal (BBO) followed by prism compression. For experiments involving spectral pump regions other than around 800 or 400 nm, pulses were generated using a Quantronix TOPAS (traveling-wave optical parametric amplifier of superfluorescence). The TOPAS is a five pass 800 nm pumped BBO based OPA which produces s-polarized output tunable between 1150 and 1600 nm, and collinear p-polarized.idler output between 1600 and 2600 nm. Selection of an individual beam is achieved by means of dichroic beamsplitters and long or short pass filters. Polarization is controlled by means of half wave plates.

2.4 Infrared Generation

The infrared pulse source used through this thesis was originally based on the design published by Hamm and Stenger.[6, 7] The schematic of the setup is shown in Figure 2.4. Of the input 250 μJ 2% (5 μJ) is sent through a half wave plate to rotate the polarization and passes through an iris to control the mode that is focused onto a 1mm sapphire crystal. The white light is focused and passes along path A to be used as a seed in parametric generation. An additional 10 percent of the input beam passes along B, focused by a 50 cm lens. Beams on path A and B are combined using a dichroic mirror (DC1; R=800 p T= 1300 S)

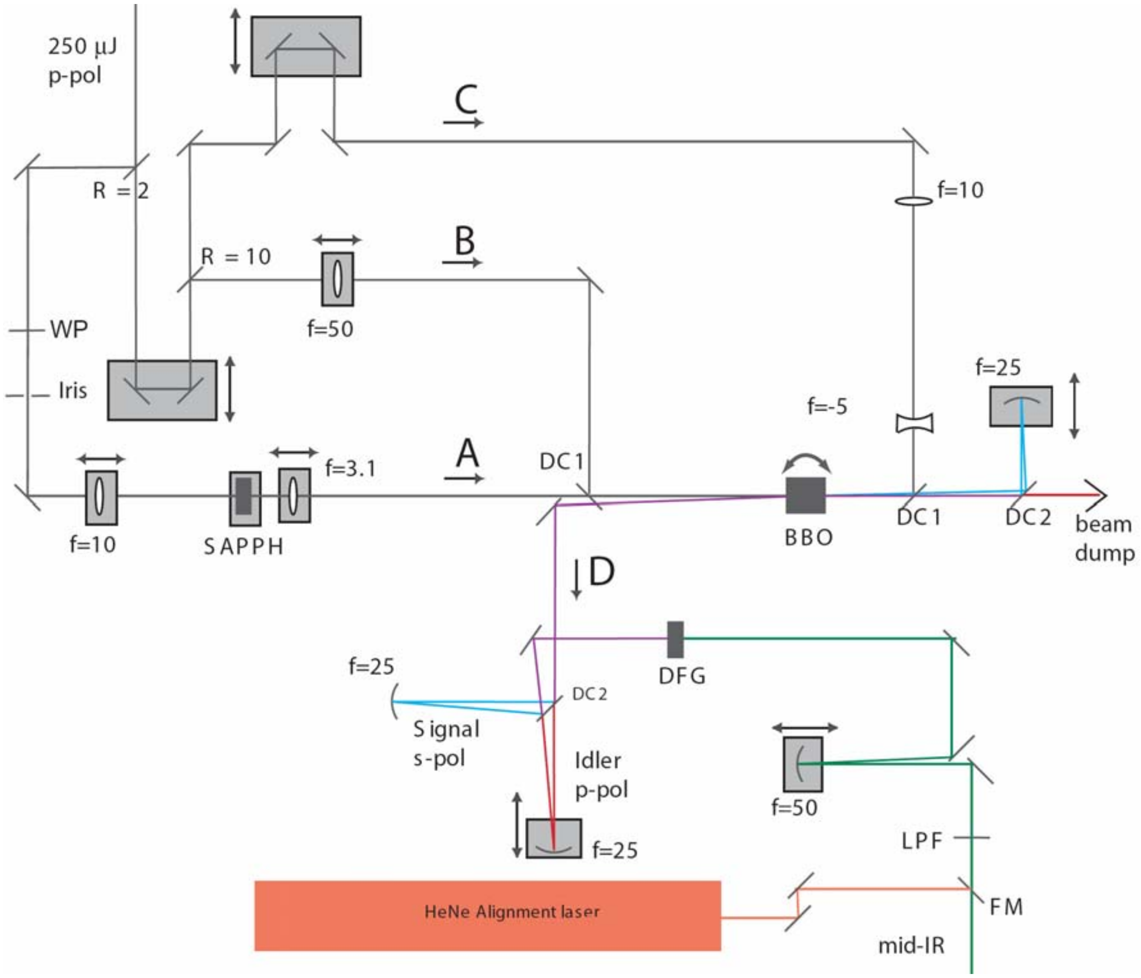

Figure 2.4 Mid-IR OPA schematic. All mirror and lens focal lengths (f) are in cm. Partial reflectors are listed (R) in percent. Path A is the white light seed, B is the first pass pump, C is the second pass pump, D is the exit path into difference frequency stage. See text for a complete description. DC1, DC2 dichroic mirrors, DFG difference frequency crystal, WP waveplate, LPF long pass filter, FM flipper mirror, BBO β-barium borate, SAPPH, sapphire crystal.

onto a 4mm type II BBO crystal (θ=26.7° ϕ=0°). The tight focus of the first pass pump (path B) acts to spatially filter the white light seed improving the beam quality of the signal beam. This first OPA stage passes through a second DC1, the idler beam is discarded using a second dichroic beamsplitter (DC2; R=1300 s T=1800 p), and the signal beam is collimated using a 25 cm focal length gold mirror. The signal is then reflected back to be pumped by the remainder of the beam. The remaining pump power (~210 μJ) passes along path C and through a 2 to 1 telescope to match the spot size of the signal beam. The original design provided by Stenger[7] lacked the delay stage in path C, and as a result all fine tuning of the time delay was controlled by the first pass collimating mirror. By adding the delay, we remove the necessity to change the collimation of the first pass, allowing for improved final conversion efficiency. The second pass amplified beam is displaced vertically and picked off by a square gold mirror and passed into the difference frequency setup. The combined power of the signal and idler is ~50-60 μJ.

In the difference frequency section of the apparatus (path D), the signal and idler are separated by an identical DC2 beamsplitter, and independently focused and synchronized onto a 1.0 mm type I $AgGaS_2$ crystal (θ=37.1° ϕ=45°) difference frequency crystal. To improve collimation of the resulting mid-IR beam, an additional concave gold mirror with a 50 cm focal length is used. Residual light from the signal and idler beams are blocked with a 2.5 μm long pass filter, and overlapped with a HeNe tracer beam using a flipper mirror (FM). This apparatus produces a mid-IR beam tunable between 3 and 7 μm with pulse energy of ~1-2 μJ with pulse duration of ~90-100 fs. An interferometric autocorrelation of a 5.0 μm beam is shown to Figure 2.5.

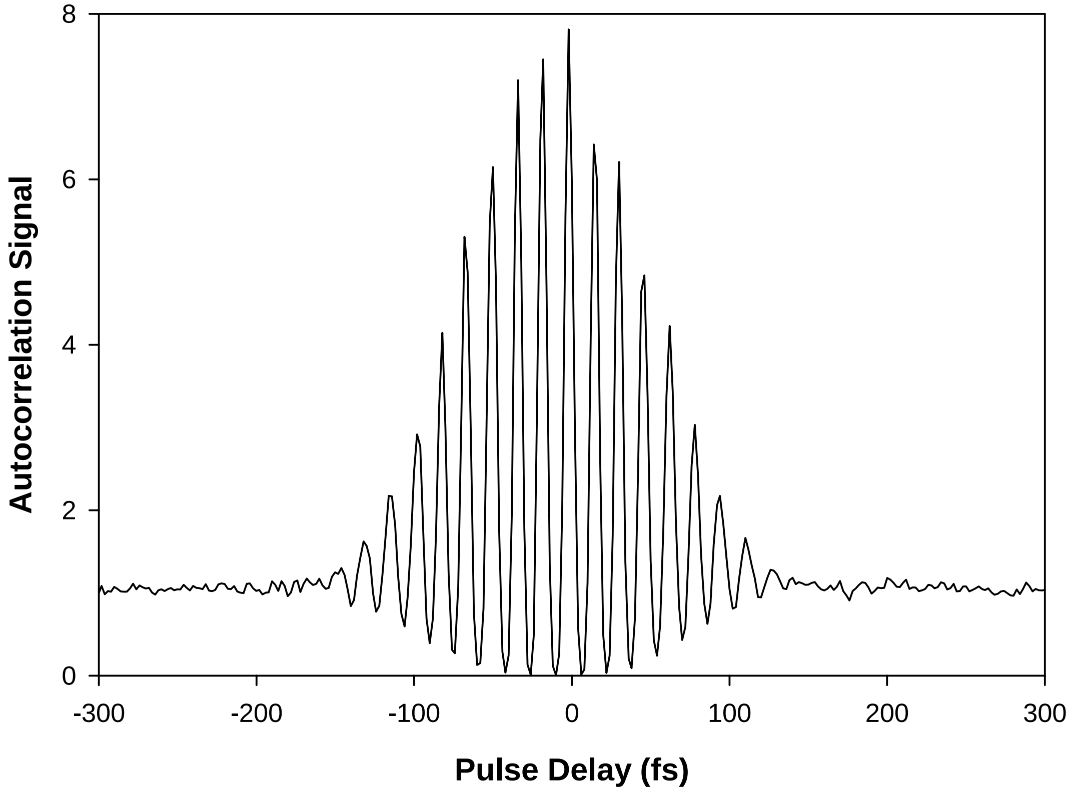

Figure 2.5 Interferrometric autocorrelation of 5000 nm pulse. This plot is unscaled and gives the proper 8:1 ratio. Fits to a gaussian pulse duration FWHM of 95 fs.

The near-IR portion of the OPA produces beams capable of DFG beyond 10 μm, if a suitable DFG crystal were used.

2.5 Experimental Layout

Figure 2.6 displays the setup to produce the pump beam for our experiments. This setup allows pumping with 800 nm, 400 nm, TOPAS signal and idler (1150-2600 nm) and TOPAS signal and 800 sum frequency (475-525 nm). To use 800 and 400 nm pump, removable mirrors RM1 and RM2 remain in the beam. Beam polarization and power are controlled by means of a waveplate (WP) and polarizer (P). To use the fundamental of the TOPAS as a pump source RM1 and RM3 are removed. A short pass filter (SPF) is used so that only the signal beam is incident on the sample. For TOPAS, 800 nm sum frequency pump source, RM3 is replaced, RM4 is removed and the 800 nm blocking filter is removed from the TOPAS. The 800 nm beam polarization is rotated and made collinear with the signal beam using two dichroic beamsplitters (DC; R=800 T=1300) and focused onto a sum frequency crystal (BBO-SF; 0.1mm, θ=20.9° ϕ=0°), followed by compression using a fused silica prism pair. For pulse autocorrelation of the TOPAS and the sum frequency beam, RM5 is placed in the beam to align into the second harmonic autocorrelator (SHG-AC).

The pump beam is then passed into the experimental box along with the mid-IR beam. The box, shown in Figure 2.7, is capable of being sealed and nitrogen purged when necessary. The mid-IR beam enters from the left, RM1 is used to align the OPA beam into an interferometric autocorrelator. Without RM1 in place the beam passes through a 50 percent beamsplitter. The reflected beam (shown in blue) is used as the

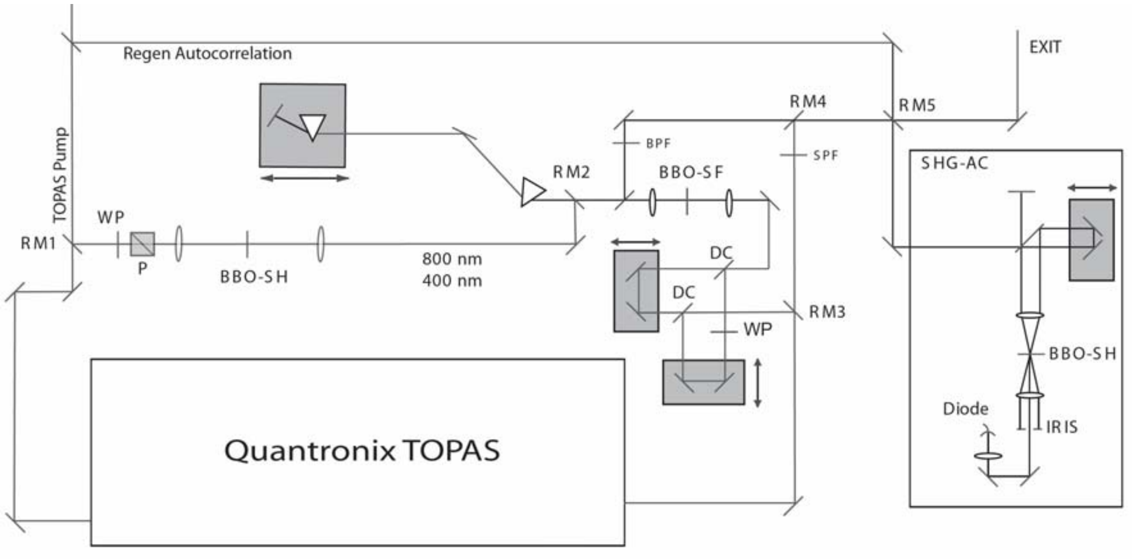

Figure 2.6 Experimental setup for pump pulse production. The TOPAS output can be used directly, or mixed with 800 nm, and compressed, using a BBO crystal (BBO-SF). Beam are autocorrelated using the second harmonic autocorrelator (SHG-AC). Typical TOPAS autocorrelations are ~60 fs, sum frequency autocorrelations are ~80 fs. RM removable mirror, WP waveplate, P polarizer, BBO-SH second harmonic crystal, SPF short pass filter, BPF band pass filter.

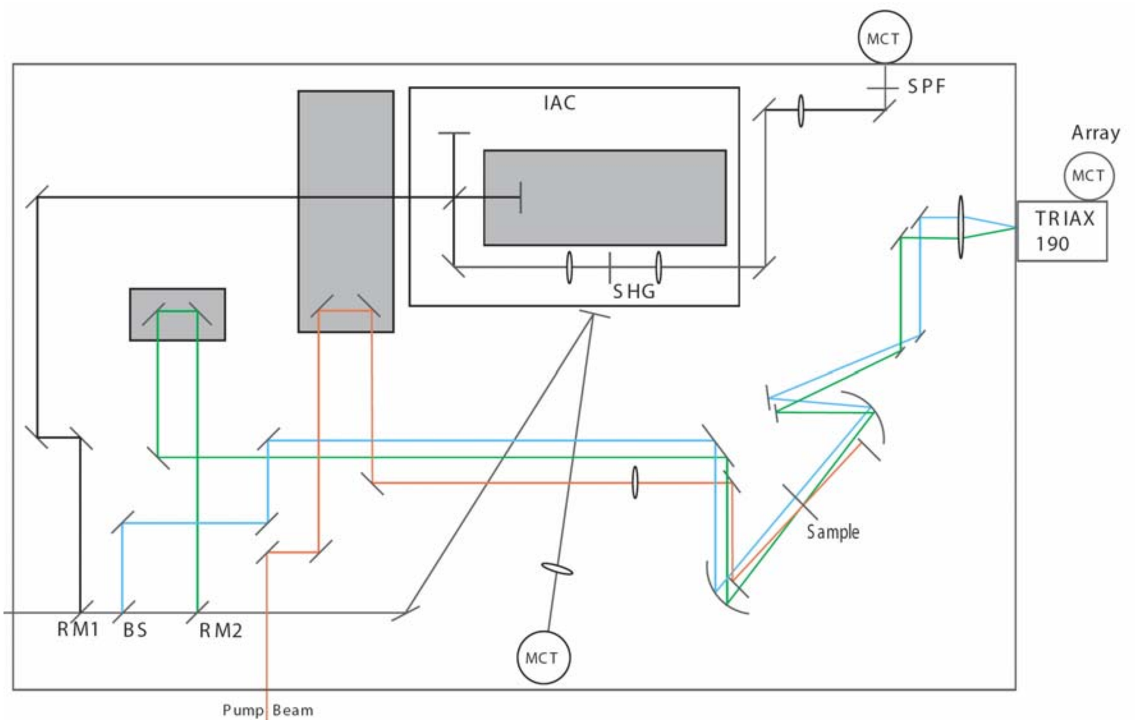

Figure 2.7 Experimental setup for pump-probe. The mid-IR beam is using a beamsplitter (BS) and the signal (green) and reference (blue) beams are passed through the sample. The signal is overlapped with the pump beam (red). Removable mirrors (RM1 and RM2) are used to tune up the OPA (RM2) and pass the IR beam into an interferometric autocorrelator (RM1). IAC interferrometric autocorrelator, SHG second harmonic generation crystal, MCT HgCdTe detector.

reference beam. The reflected beam reflects from RM2 and is used as the signal beam. Both beams are focused using a 15 cm focal length off-axis parabolic to approximately 150 μm spot size, recollimated using another off axis parabolic mirror, displaced vertically and focused into a TRIAX 190 (HORIBA Jobin Yvon Inc.) imaging spectrometer. The beams are detected using a 2x32 element HgCdTe array detector, allowing us to detect signals on the order of 0.5 mOD. RM2 can be removed in order for the OPA to be optimized. The pump beam enters from the bottom and is focused onto the sample using a 40 cm fused silica lens, which is adjusted laterally to optimize the excitation spot size. The delay between the pump and probe is controlled with a Newport PM500-8M delay stage, time zero is found by replacing the back window of the sample cell with a 2 mm ZnSe window.

2.6 References:

1. M. T. Asaki, C. P. Huang, D. Garvey, J. P. Zhou, H. C. Kapteyn and M. M. Murnane, *Opt. Lett.*, 1993, **18**, 977-979.
2. M. M. Murnane, H. C. Kapteyn, C. P. Huang and M. T. Asaki, *Mode-Locked Ti:Sapphire Laser* 1.7 edn., Department of Physics Washington State, Pullman, WA, 1994.
3. D. Strickland and G. Mourou, *Opt. Commun.*, 1985, **56**, 219-221.
4. B. S. Prall, University of California, Berkeley, 2005.
5. D. Y. Parkinson, University of California, Berkeley, 2006.
6. P. Hamm, R. A. Kaindl and J. Stenger, *Opt. Lett.*, 2000, **25**, 1798-1800.
7. J. Stenger, Humboldt University, 2002.

Chapter 3: Investigation of the Excited State Structure of DCM via Ultrafast Electronic Pump / Vibrational Probe

Reproduced with permission from A.J. Van Tassle, M.A. Prantil and G.R. Fleming, *J. Phys. Chem. B.*, **100**, 10898 (2006).

3.1 Abstract

Time resolved visible pump, infrared probe transient absorption measurements of the solutes 4-dicyanomethylene-2-methyl-6-(p-(dimethylamino)styryl)-4*H*-pyran (DCM) and its isotopomer DCM-d6 are employed to probe the dynamics of charge transfer state formation in dimethylsulfoxide (DMSO) and acetonitrile (MeCN). We observe a two stage charge transfer (CT): the first step of which is an instrument response-limited charge separation to the dicyanomethylene group, and the second involves a structural evolution of the dimethylamino group. Theoretical calculations and isotopic substitution indicate that the observed vibration is due to the dimethylamino group twisting out of plane, stabilizing the charge separation.

3.2 **Introduction**

The photophysical and photochemical behavior of organic molecules is strongly influenced by charge transfer between electron donating and electron accepting groups following electronic excitation. The way in which the electronic structure evolves, is influenced by the solvent, and in turn influences the molecular structure and is very difficult to discern from electronic pump-probe or fluorescence spectroscopy.. The combination of ultrafast infrared (IR) probing with electronic excitation has the potential to reveal much greater detail about the excited state evolution after initial excitation, and has been used successfully on several systems.[1-7] In this paper we employ ultrafast electronic excitation and broadband IR probing to study the excited state structural evolution of DCM, a laser dye of analogous structure to 4,4’-disubstituted push-pull stilbenes and dimethylaminobenzonitrile (DMABN). DCM has previously been studied, along with several derivatives, for possible use in new graphical displays and organic light emitting diodes.[8-12]

Many of the interesting properties of DCM arise from the charge transfer that occurs in the excited state formed by charge separation between the electron donating dimethylamino group and the electron accepting cyanomethylene groups. Because of the considerable charge separation, the molecule possesses a large, solvent polarity-dependent Stokes shift and has a drastic change in dipole moment (20.7 Debye) from the ground to the excited states.[13-16]

The evolution of DCM from a locally excited electronic state to a charge transfer state has been investigated by numerous authors[13, 17-24] who attribute its behavior to one or more of the possible configurational changes, which produce the twisted (TICT), conformationally relaxed (CRICT), re-hybridized (RICT), and planar (PICT) intramolecular charge transfer states.[4, 19, 25-33] Previous investigations of DCM[19, 23, 34] considered the formation of a TICT state involving rotation about the C-N bond linking the dimethylamino group to the aromatic ring, or rotation of the dimethylaminobenzyl moiety, but these experiments lacked any direct probe of structural change. Another proposed state is one analogous to the P* state [26, 30, 35] of stilbenes in which the molecule adopts a perpendicular conformation about the central double bond as an intermediate between cis and trans configurations. Electronic structure calculations for DCM using CS INDO have been able to locate a singlet state with a dipole moment large enough match the experiment, and in this state DCM adopts a configuration in which the dimethylamino moiety is perpendicular to the aromatic ring.[19]

Recent detailed electronic structure studies of DMABN by Robb and coworkers lead to the conclusion that optical excitation initially populates the S_2 state and that radiationless decay via a conical intersection seam can lead to both local and CT states being directly populated, followed by equilibration taking place on the S_1 surface.[36]

The use of IR wavelengths for probing, combined with selective isotopic substitution of DCM, opens up the prospect of determining which functional groups in DCM are involved in the excited state dynamics, and thus enabling discrimination between the various possible conformers. By changing the solvent polarity the role of solvent in the excited state evolution can also be elucidated.

3.3 Materials and Methods

Transient absorption experiments were performed with laser pulses from a home built regenerative amplifier seeded by a Femtosource Compact Pro Ti:Sapphire oscillator (Femtolasers, Inc). This system produces pulses of 35 fs and 400 μJ/pulse at 1 kHz. The pulse was split with 200 μJ being sent into a home built mid-infrared (mid-IR) optical parametric amplifier (OPA), based on the design of Hamm et al..[37] The design is comprised of a two pass 800 nm pumped near-IR OPA followed by difference frequency generation. Briefly, a white light continuum seed and two sequential amplifier pulses pass through a BBO crystal followed by a separation, independent focus and time-syncing of the signal and idler pulses onto a 1 mm $AgGaS_2$ difference frequency crystal. The OPA produces mid-IR pulses tunable between 3 and 7 microns (3300-1400 cm^{-1}) with pulse durations of 95 fs at 5 μm and 1-2 μJ/pulse. The remainder of the amplifier pulse was frequency doubled by means of a 0.1 mm BBO crystal and compressed with a pair of fused silica prisms to a final pulse duration of 80 fs and pulse energy reduced to 1 μJ/pulse by means of a λ/2 waveplate and polarizer placed prior to the doubling crystal. The 400 nm and mid-IR pulses were focused onto a 100 μm thick flowing or spinning sample cell with 2 mm calcium fluoride windows. The pulses were arranged in a parallel polarization configuration and temporal overlap was found by replacing the back window of the sample cell with a ZnSe window, resulting in a large, long lived transient absorption signal. The signal was spectrally resolved using a Triax 180 imaging spectrometer (Jobin-Yvon Horiba) with grating appropriate to supply 4 cm^{-1} resolution. Detection of the mid-IR pulses was done with a 32 element HgCdTe array detector (Infrared Associates) attached to an IR32-16 multichannel laser pulse system (Infrared Systems Development Corp.). The detection was triggered by the fundamental laser repetition rate and an output frequency of a phase locked chopper inserted into the pump beam. One point to take into consideration in our experiments is that while in electronic spectroscopy one is able to directly correlate signal intensity with electronic state population, when using the mid-IR as the probe wavelength signal intensity can also arise from the changes in dipole strength by time dependent electron density modulations.

Steady state absorption spectra were measured using a Shimadzu UV-1601 spectrometer. Steady state fluorescence data was collected using a Spex Fluorolog-τ2 with a red extended Hamamatsu photomultiplier tube (model #R2659). The concentrations used for the transient absorption experiments were low (typically 1 mg/mL, ~ 1×10^{-4} M), so as to avoid the formation of bicimers.[27, 32] The presence of cis isomers, which we want to avoid, is also concentration dependent[38]. The steady state absorption spectra were collected with sample concentrations so as to produce a maximum absorption of ~0.5. The steady state fluorescence spectra were obtained by diluting the samples used for absorption by a factor of 10.

Time resolved fluorescence measurements were performed using a time correlated single photon counting (TCSPC) apparatus set at the magic angle polarization. A Coherent Inc. mode locked femtosecond laser (Mira 900) with a diode pumped, frequency doubled Nd:YVO_4 (Verdi V-10, Coherent) was used as the excitation source. The output beam was frequency doubled using a 1.5mm thick BBO crystal. The repetition rate was reduced from 76 MHz to 3.8 MHz using an extra cavity pulse picker giving a center wavelength of 400 nm and pulse energy of ~3 nJ. Emission was selected using a double grating monochromator (DH10 VIR, Jobin Yvon) with a spectral bandpass of 4 nm at the emission maximum in a 1 cm path length stirred sample cell. The signal was collected by means of a multi channel plate (Hamamatsu MCP model # R28094-01) and a single photon counting card (Boston Electronics SPC-630) set for 5.5 ps/channel. All standard solvents were used as received from Sigma Aldrich and were of best spectroscopic grade available. Deuterated solvents were used as obtained from Cambridge Isotope Labs. DCM was obtained from Exciton without further purification, HPLC of fresh samples of DCM solution exhibit only one elutant peak, which is attributed to the trans form of DCM.[18, 38] Upon equilibration in room light for 24 hours the elutant peak from the trans form splits into two distinct visible absorptions and the newly arising peak is assigned to the cis form of DCM which has slightly stronger absorption to the blue side of the trans absorption. Transient absorption experiments performed using either fresh or light equilibrated samples, show no difference in lifetimes, intensities, or dynamics of the vibrational bands observed.

Visualization of the vibrational modes is made possible by calculating the vibrational spectrum with density functional theory (DFT) using the BLYP 6-31G(d) basis set in the QChem package,[39] extracting the vibrational normal modes, and viewing them using the Molekel molecular graphics package.[40]

3.4 Synthesis of DCM-d6

The synthesis of DCM-d6 primarily followed a previously reported synthesis[41], a short summary follows. (2,6-Dimethyl-4*H*-pyran-4-ylidene)-malononitrile was synthesized by refluxing 2,6-dimethyl-γ-pyrone and malononitrile in the presence of acetic anhydride for 45 min followed by removal of the resultant acetic acid under vacuum and recrystallization from cyclohexane[42]. Dimethylaniline-d6 was synthesized from freshly distilled aniline and d3-iodomethane in the presence of sodium carbonate[43]. To form the aldehyde, dimethylaniline-d6 underwent a Vilsmeir formylation with pyrophosphoryl chloride and dimethyl formamide and was sublimed in a Kugelrohr apparatus to give 4-dimethylaminobenzaldehyde-d6[44]. DCM-d6 was formed by the reaction of 4-dimethylaminobenzaldehyde-d6 and (2,6-Dimethyl-4*H*-pyran-4-ylidene)malononitrile in the presence of piperidine. The final purification was done without recrystallization, and the retention factor of DCM was found to be 0.9 for chloroform on Whatman PK6F TLC plates, by co-spotting with the commercial DCM, contrary to the retention factor of 0.1 that was reported in ref 40.

3.5 Results

The effect of the deuterium substitution on the ground state infrared absorption frequencies along with the structures of both isotopomers are depicted in Figure 3.1. The FTIR spectra shown in Figure 3.1 illustrate the presence of a new absorption band at ~2050 cm^{-1} in DCM-d6 which is red shifted from ~3000cm^{-1} in DCM due to the change in reduced mass of the C-D bond.

A summary of all steady state measurements is presented in Table 3.1 for the solvents DMSO and MeCN. As shown in the table, the visible absorption spectrum of DCM undergoes a slight red shift upon deuteration (~175-250 cm^{-1}), but the center frequency of the fluorescence spectrum remains unchanged between DCM and DCM-d6. This shift in absorption can simply be attributed to a change in the zero point energy upon deuterium substitution, and the difference between the anharmonicities of the ground and locally excited (LE) state. The fluorescence quantum yield of DCM-d6, however, is decreased quite substantially; by 24% in DMSO and 17% in acetonitrile compared to DCM. Figure 3.2 shows that the steady state absorption spectra for both DCM and DCM-d6 in MeCN have similar lineshapes. The fluorescence spectra for both molecules however remain unaffected in both solvents we studied. The average fluorescence lifetimes (τ_{av}) listed in Table 3.1 were determined from Equation 3.1;

$$\langle \tau \rangle = \frac{a_1}{a_1 + a_2}\tau_1 + \frac{a_2}{a_1 + a_2}\tau_2 \qquad \text{eq 3.1}$$

Table 3.1: Steady State Spectral Data for DCM and DCM-d6

Solvent					
DMSO	**Abs Max (nm)**	**Abs Diff (cm^{-1})**	**Fluor Max (nm)**	**τ_{av} (ns)**	**Φ(d6)/Φ(h6)**
DCM	479.5	258	634	2.13	0.76
DCM-d6	485.5		634	2.40	
CH_3CN					
DCM	460.4	178	615	1.65	0.83
DCM-d6	464.2		615	1.80	

Abs Diff : Difference in absorption maxima between isotopomers

τ_{av} : Average fluorescence lifetime determined via Eq. 1

Φ(d6)/Φ(h6) : Ratio of fluorescence quantum yields for the isotopomers

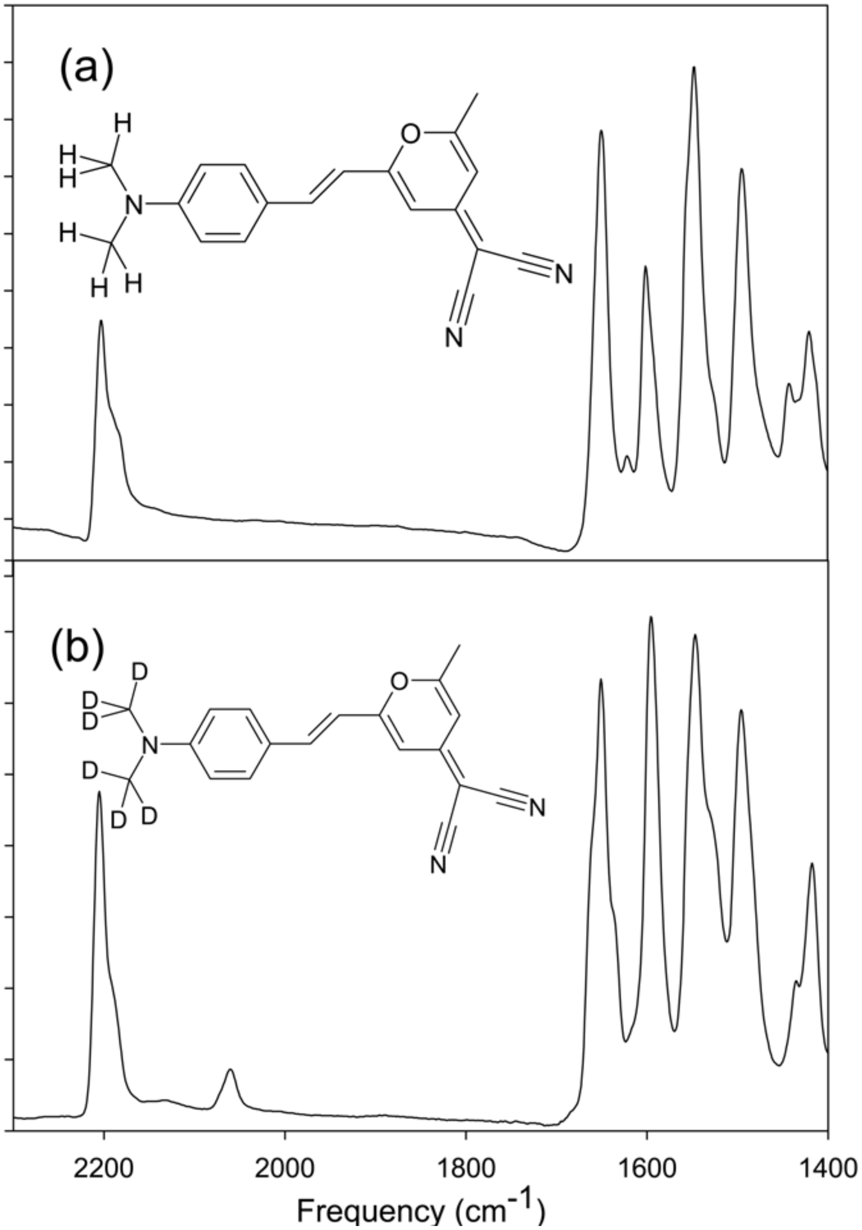

Figure 3.1: Infrared spectra of DCM (a) and its isotopomer DCM-d6 (b). The structure of both molecules are shown above their respective spectra.

where a is the amplitude of the exponential component and τ is the lifetime. This equation was applied to the results of fits to the TCSPC traces which contained three timescales; a rapid rise, with a timescale of approximately one quarter of the instrument response of our apparatus, and two decay components. The rise times were excluded from the calculation of the average fluorescence lifetime; since the lifetime of this component is so short the values of τ_{av} calculated using this rise were altered by no more than ~1%.

The mid-IR (shown from 1440 cm^{-1} to 1620 cm^{-1}) transient absorption contour plots presented in Figure 3.3 were collected by calculating the change in optical density (ΔOD) induced by 400 nm excitation of DCM using an average of 200 pulses per delay time and taking at least 10 scans over the entire delay timescale, up to a maximum of 500 ps. Deuterated solvents were chosen so as to avoid overlap with the solute peaks of interest by shifting the solvent absorptions to lower frequencies. The spectra in acetonitrile and DMSO contain several distinct absorption features: a peak at ~1440 cm^{-1} that has an instrument response limited rise and undergoes almost solely relaxation (decay) dynamics, and a higher frequency peak (~1495 cm^{-1}) that undergoes a blue shift of its center frequency as well as more complex intensity changes. The other absorptions in these spectra are at 1520 and 1590 cm^{-1} whose center frequencies do not shift but undergo changes on the same timescales as those of the 1495 cm^{-1} band. Fits of the intensity dependence of the 1495, 1520, and 1590 cm^{-1} peaks require multiple exponential

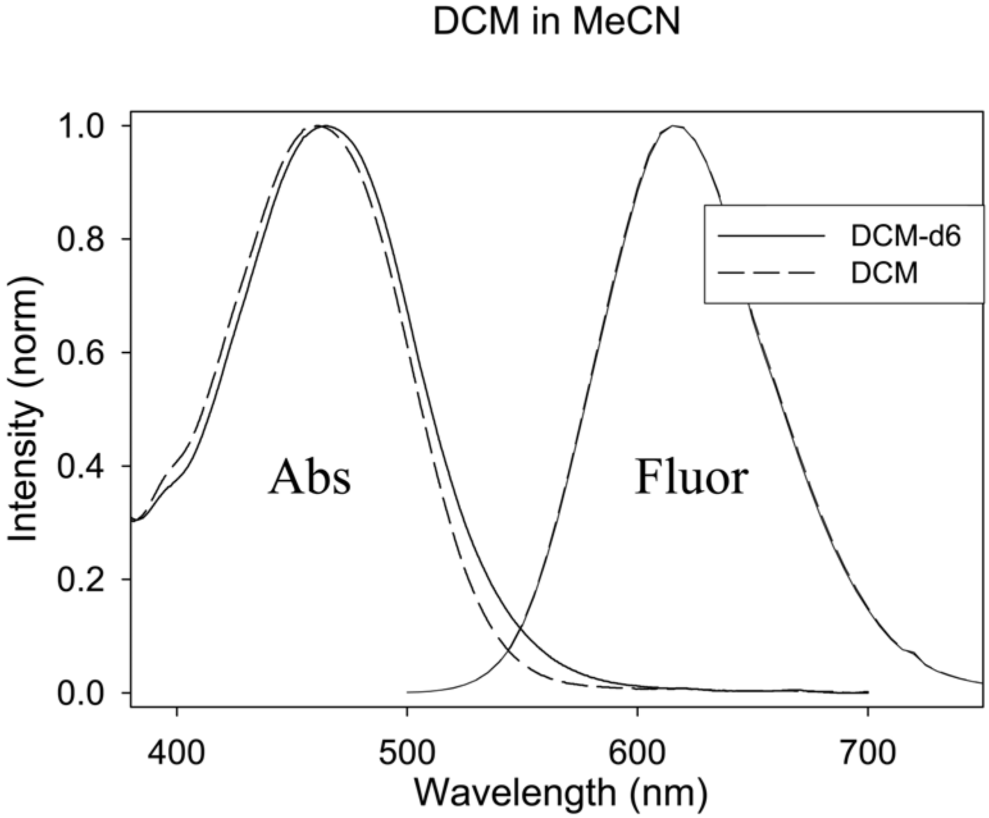

Figure 3.2: The absorption and fluorescence spectra of DCM (solid line) and DCM-d6 (dashed) in MeCN-d3. DCM-d6 absorption is red shifted 178 cm^{-1} from DCM while the fluorescence spectra are indistinguishable.

components, with both positive and negative amplitudes. The band at 1440 cm^{-1} with its instrument response limited rise is assigned to the LE state of DCM while the higher frequency absorptions (1495, 1520, and 1590 cm^{-1}) are assigned to the CT state. The plots in Figures 3.3 and 3.4 also show a slight solvent dependence of the center frequency of the absorption bands. The terminal frequency of all the excited state bands scale linearly with the Ooshika-Lippert-Mattaga solvent polarity function[13-16] which is a function of the dielectric constant and index of refraction of the solvent, the slope of these fits are 1.5 times greater for the CT bands than for the LE band. This strong solvent influence on the CT bands is most likely due to the increase in dipole moment in the CT state.

Figure 3.4 shows frequency slices of all features in the fingerprint region (from 1440 to 1620 cm^{-1}) to emphasize the dynamics, specifically the fast initial decay of the LE band (~1-2 ps) and the sharp rise (and frequency shift for the 1495 cm^{-1} band) in the CT absorption bands. We attribute the fast rise in the CT bands to the rapid evolution of the LE state into the CT state. No excited state features were observed between the region shown and the CN stretch at 2208 cm^{-1}.

These spectra were fit by a sum of Gaussians to more accurately separate the contributions to the peak intensity from linewidth changes and center frequency shifting from rise and decay. The kinetic traces shown in Figure 3.5 are constructed from these Gaussian fits. Figures 3.5 (a) and (c) show the Gaussian normalized amplitude of the ~1495 cm^{-1} feature for MeCN-d3 and DMSO-d6 solvents respectively, while (b) and (d) show the center frequency of this band versus probe delay times in the same solvents.

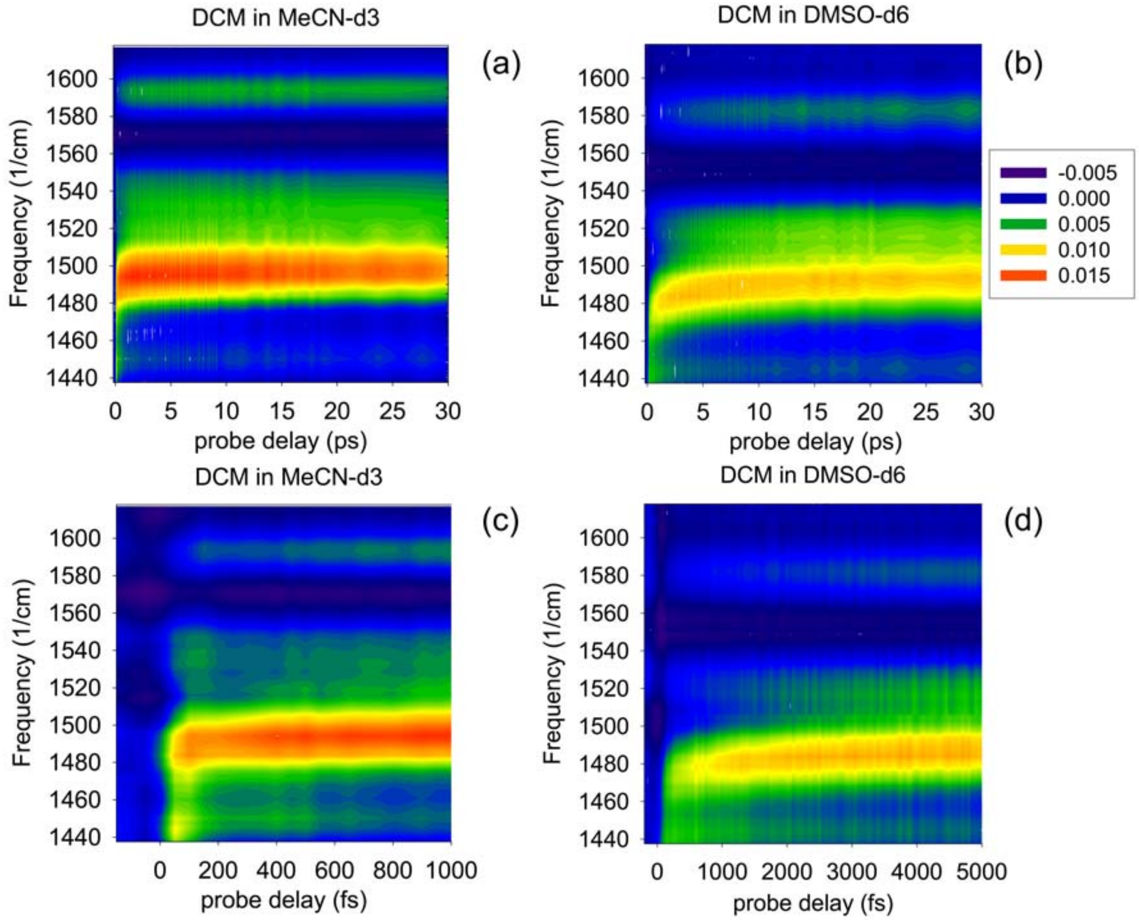

Figure 3.3: Transient infrared absorption contour plots of frequency vs. probe delay for DCM in (a) MeCN-d3 and (b) DMSO-d6. Plots (c) and (d) show the same data as (a) and (b) respectively but on shorter timescales to show the fast shifting of the 1495 cm^{-1} band. Note the time axes of panels (c) and (d) differ.

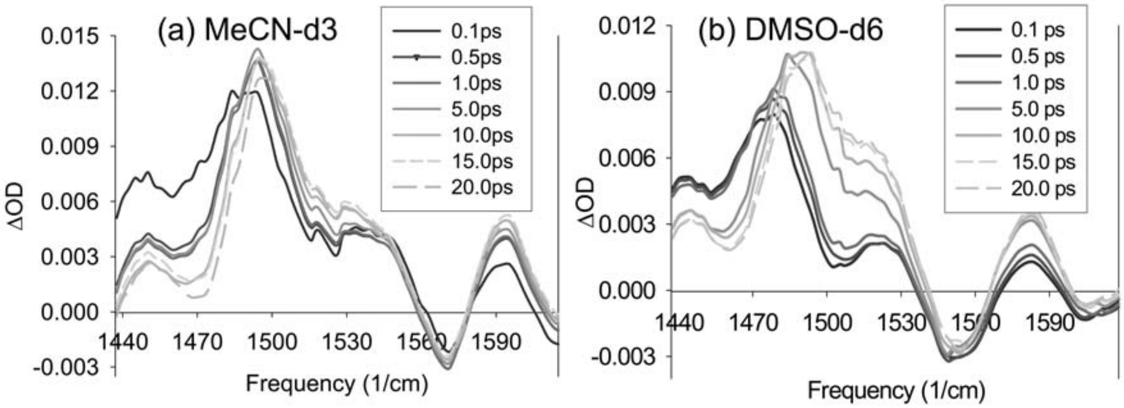

Figure 3.4: ΔOD vs. frequency slices through the surfaces in Fig. 3 at multiple probe delays for DCM in (a) MeCN-d3 and (b) DMSO-d6.

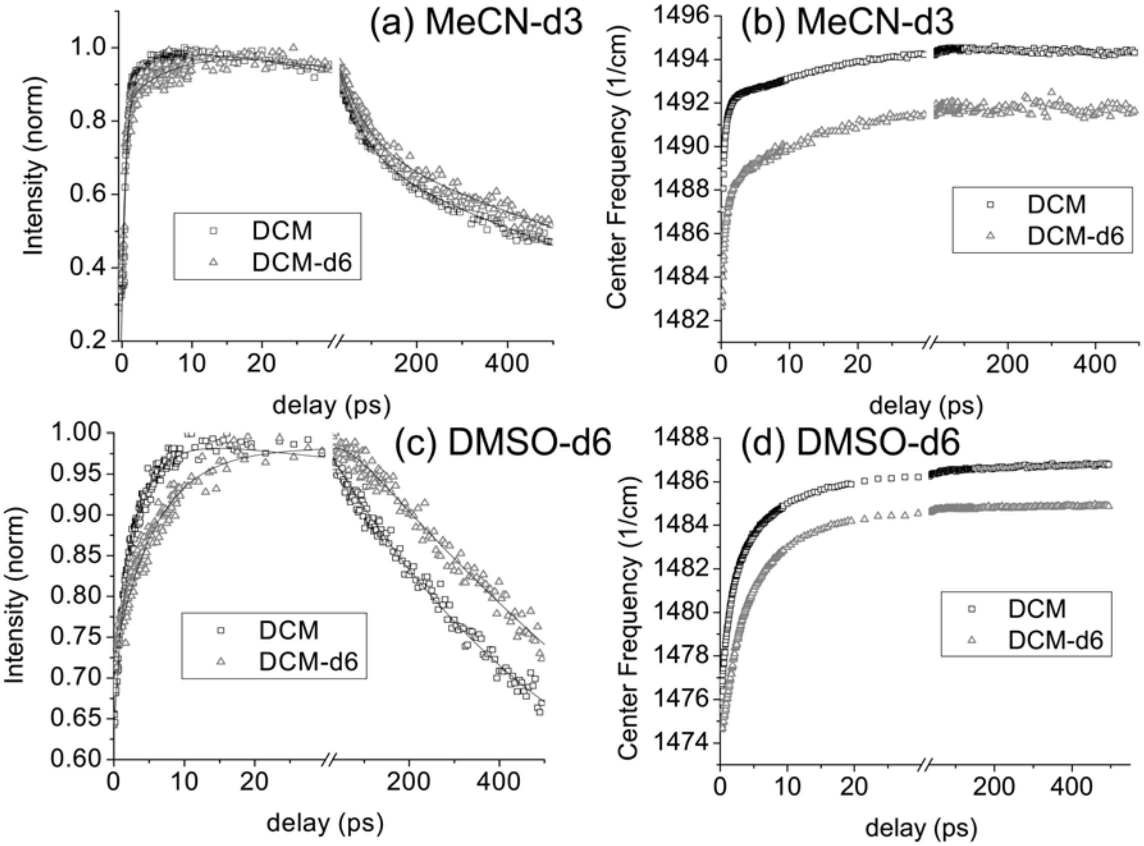

Figure 3.5:

The decay of the maximum of the ~1495 cm^{-1} peak is shown for DCM in (a) MeCN-d3 and (c) DMSO-d6. The center frequency of the ~1495 cm^{-1} peak is shown in (b) for MeCN-d3 and in (d) for DMSO-d6. Note the break in the time axes.

The center frequencies of the 1520 and 1590 cm^{-1} bands were not affected by the methyl deuteration. The plots of the intensity of the 1495 cm^{-1} band versus time in Figures 3.5a) and c) both show a fast rise (~1-3ps), a mid range growth (~10-30ps), especially notable in DMSO-d6, and long time (>500 ps) decay of the absorption in both DCM and DCM-d6. It is interesting to note that the shifting timescale of the band is also markedly faster in DCM than in DCM-d6, this is the most apparent in the case of MeCN-d3 solution due to the extremely short solvation timescales as shown in Figures 3.5 (b) and (d) showing that both molecular structure and solvation play a role in determining the timescale of CT formation. Table 3.2 collects the parameters obtained from fits of the data presented in Figure 3.5 for both the shifting of the center frequency and population dynamics as well as solvation timescales for both solvents measured by Maroncelli and Fleming using coumarin 153 as the probe.[45]

Figure 3.6 shows kinetic traces in DMSO-d6 (a) for the CN triple bond symmetric stretch ground state bleach dynamics at 2208 cm^{-1} and (b) the excited state dynamics at 2182 cm^{-1} for both DCM and DCM-d6 (scaled for comparison). There is a second excited state absorption band at 2158 cm^{-1} which has identical kinetics to the 2182 cm^{-1} band shown in Figure 3.6 (b), as it arises from the accompanying asymmetric stretch of the dicyano group, but the analogous stretch in the ground state does not appear in the spectra because it is masked by the large cross section of the ground state symmetric stretch. The kinetics for DCM and DCM-d6 are very similar for these frequencies with the excited state absorption band showing a sharp spike arising from the solvent (and present in pure

Table 3.2: 1495 cm-1 Band Dynamics and Solvation Timescales

DMSO-d6			**Solvation Times[(1)]**		**MeCN-d3**			**Solvation Times[(1)]**	
Shift	a_i (cm^{-1})	t_i (ps)	a_i	t_i (ps)	**Shift**	a_i (cm^{-1})	t_i (ps)	a_i	t_i (ps)
DCM	6.6	1.6	0.5	0.21	DCM	9.5	0.34	0.69	0.089
	4.5	10	0.41	2.3		2.6	13	0.31	0.63
	$\langle\tau\rangle$	5.0 ± 2.1	0.092	11		$\langle\tau\rangle$	3.1 ± 1.5	$\langle\tau\rangle$	0.26
DCM-d6	8.2	3.4	$\langle\tau\rangle$	2.0	DCM-d6	6.0	0.57		
	2.7	14				3.9	12		
	$\langle\tau\rangle$	6.0 ± 2.4				$\langle\tau\rangle$	5.1 ± 2.5		
Decay	a_i	t_i (ps)			**Decay**	a_i	t_i (ps)		
DCM	-0.31	2.6			DCM	-0.67	0.54		
	-0.062	34				-0.19	7.9		
	$\langle\tau\rangle$ rise	7.8 ± 0.9				$\langle\tau\rangle$ rise	2.20 ± 0.17		
	0.14	120				0.39	59		
	0.90	1730				0.91	1130		
	$\langle\tau\rangle$ decay	1500 ± 300				$\langle\tau\rangle$ decay	810 ± 190		
DCM-d6	-0.25	6.6			DCM-d6	-0.85	0.47		
	-0.066	40				-0.27	11		
	$\langle\tau\rangle$ rise	13.5 ± 1.5				$\langle\tau\rangle$ rise	3.5 ± 1.1		
	0.046	100				0.36	59		
	1.0	1750				0.76	1250		
	$\langle\tau\rangle$ decay	1700 ± 1100				$\langle\tau\rangle$ decay	900 ± 500		

a_i : amplitude of the exponential component

τ_i : lifetime of exponential component

$\langle\tau\rangle$: average lifetime determined via Eq. 1

(1) The timescales of solvation for DMSO and MeCN are taken from Maroncelli and co-workers.[46]

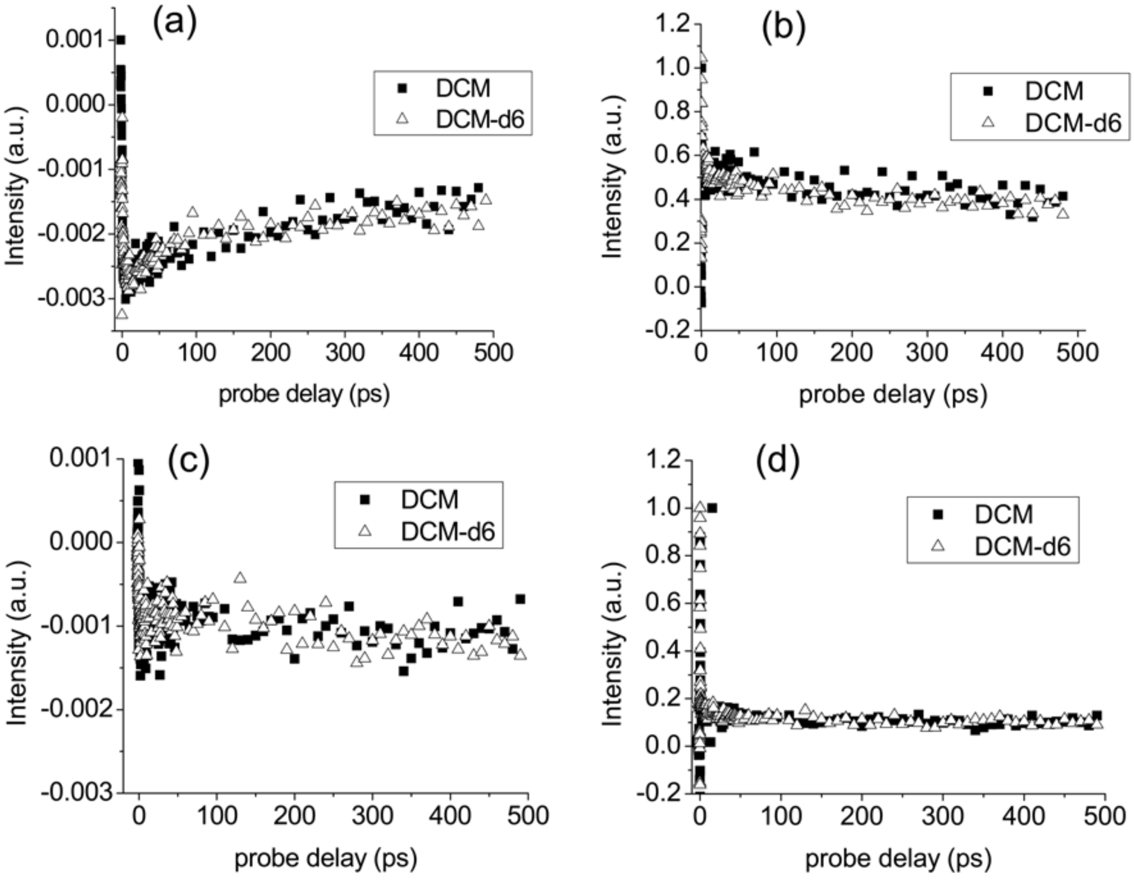

Figure 3.6: (a) and (c): Intensity vs. probe delay at 2208 cm^{-1} (ground state CN stretch) of DCM and DCM-d6 in DMSO-d6 (a) and MeCN-d3 (c). (b) and (d): Intensity vs. probe delay at 2182 cm-1 (excited state CN stretch) in DMSO-d6 (b) and MeCN-d3 (d).

solvent), followed by a very slow decay (~10% in 500 ps).

3.6 Discussion

The time resolved infrared spectra of DCM in polar solvents clearly show that the excited state electronic structure evolves in a solvent-dependent manner from that created directly by optical excitation. The instrument limited change in the CN triple bond symmetric stretch frequency suggests charge separation and localization on the cyanomethylene acceptor groups occurs immediately upon excitation. The fact that no further changes in the CN stretch frequency are observed suggests that the RICT state, like that proposed for DMABN[4], in which the cyano carbon becomes sp^2 hybridized is not accessible for DCM.

We have no direct evidence to suggest that the S_1 LE state is the one populated by optical excitation rather than via radiationless relaxation from S_2 as appears to be the case for DMABN.[36] However, the solvent-dependent evolution of the IR spectra do imply that if S_1 is populated via S_2 motion through the conical intersection, this does not lead to a wide range of torsional angles for the dimethyl amino group being populated at very short times, since this would lead to a broad range of frequencies for the 1495 cm^{-1} region.

The short-time evolution we see involves the dimethyl amino group most likely rotating out of place (and pyramidalizing[4, 47]) giving rise to a deuterium- and solvent-dependent frequency shift of the 1495 cm^{-1} band. Since the center frequencies of the 1520 and 1590 cm^{-1} bands do not shift their modes must be independent of the torsional angle of the dimethylamino group within our model. Yoshizawa et al, using a stimulated

Raman method in DMSO solution report vibrational bands at 1470 and 2150 cm^{-1} which they assign to a state intermediate between trans and cis.[48] However, their time and spectral resolutions of 250 fs and 25 cm^{-1}, respectively, are inadequate to reveal the short time dynamics shown in Figures 3.3 through 3.5.

The identity of the 1495 cm^{-1} band is not trivial to establish unambiguously. Figure 3.7 shows the displacement vectors for the calculated mode in the ground state of DCM that serves as the most likely candidate from our calculations. It involves considerable motion of the carbon skeleton of the molecule and has no contribution from the CN groups. In Table 3.2, we compare the timescales of the shift in frequency of the 1495 cm^{-1} band for DCM and DCM-d6 with solvation times for DMSO-d6 and MeCN-d3 obtained from Stokes shift measurements by Maroncelli and coworkers.[45, 46] We find a very fast component in the shift for acetonitrile solution, consistent with the amplitude of ~100 fs relaxation in the solvation response in acetonitrile, while for DMSO we do not observe an ultrafast component in the shift although a ~ 200 fs component is present in the solvation reponse. The average shifting time $\langle \tau \rangle$, presented in Table 3.2, is determined using Equation 1. The average shifting time is shorter in acetonitrile than DMSO (3.1 ps vs. 5.0 ps), and in each case $\langle \tau \rangle$ is smaller for DCM than for DCM-d6. The comparison of solvation timescales with the shift timescales is complex for several reasons: first the frequency change results from motion on the excited state potential surface, and its timescale will be set by the shape of the surface as well as the solvent timescales. In addition, the strength of the IR transition may change during the relaxation, and it may change differently for DCM and DCM-d6 since the nature of the

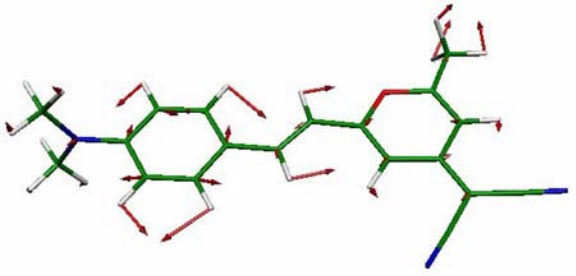

Figure 3.7: The calculated displacement vectors in the ground state of DCM for the mode that we suggest to give rise to the 1495 cm^{-1} band. (see Materials and Methods)

mode (and its couplings to other modes) is different in the two molecules. Table 3.2 shows that the average shift times and rise times for the intensity of the mode are, however, quite similar and show the same trends with deuteration and change of solvent suggesting these times can, at least roughly, be associated with population changes. We therefore, associate the timescale of 5-8 ps (DMSO-d6) and 2-3 ps (MeCN-d3) with formation of the TICT state in DCM. Similarly, the timescales of 6-14 ps, and 3-5 ps correspond to TICT formation in DCM-d6 in DMSO-d6 and MeCN-d3, respectively. Following the calculations of Gomez et al.[36] we expect the TICT state to involve both twisting and pyramidalization of the C-N(Me$_2$) group. The average decay times for the CT modes are quite similar for DCM and DCM-d6 in each solution (with the d6 molecule having slightly slower decays in both solvents), but vary by a factor of two from DMSO-d6 to MeCN-d3. The average fluorescence lifetimes (Table 3.1) are longer than the vibrational "lifetimes" listed in Table 3.2 and the difference between DMSO-d6 and MeCN-d3 solutions is much smaller (14% vs 47%). Clearly this hints at more complex excited state behavior than simple LE-TICT equilibration and subsequent decay on a ~2 ns timescale, but equilibration and IVR within the TICT minimum presumably leads to configurations with much weaker oscillator strength for the 1495 cm^{-1} mode.

If the observed spectral dynamics involves rapid LE to CT conversion we must also consider the role of excess vibrational energy on the spectra, following the transition. Previous studies of 2-(2'-hydroxyphenyl)benzothiazole[6] and trans-stilbene[49] have found similar blue shifts in all the bands of their vibrational spectra as a result of vibrational relaxation. The timescales of these shifts were compared in solvents of varying thermal diffusivity and as might be expected, the relaxation rate increased with increasing thermal diffusivity. While this general trend holds for the 1495 cm^{-1} mode, if the average lifetimes are compared, the amplitudes of the shift are much larger than those found in stilbene and benzothiazole, the lifetimes of which are much shorter (by nearly an order of magnitude in the case of the longest timescales). In addition, only a single band shows the upshifting while all other observed bands have only amplitude changes. Also, we do not expect a significant amount of vibrational energy to be released in the LE to CT transition since the process occurs on a few picoseconds timescale. We therefore conclude that vibrational relaxation can be ruled out as the cause of the shift we observe. If the shift was a manifestation of vibrational cooling we would expect to also observe shifts in the 1440, 1520, 1590, and 2182 cm^{-1} bands, which is not the case.

The fluorescence quantum yield is significantly lower in DCM-d6 than DCM (Table 3.1), even though the average fluorescence lifetime is very similar in both isotopomers. This means that the radiative rate decreases by almost the same amount that the non-radiative rate increases in DCM-d6. A change of ~ 10% in each is consistent with the measurements. In a conventional relaxation process the excited state energy is converted into C-H stretch energy and subsequently transferred into the local solvent modes. One would normally expects that the deuterium substitution would increase the lifetime because it would slow the internal conversion, in contrast to our observation.

Up to this point we have not discussed the second pathway of excited state decay, trans to cis isomerization. The quantum yield of this process has measured for both DMSO and MeCN solutions as 0.014 and 0.011, respectively.[18, 20] With such a small yield it seems unlikely that the strong IR bands described result from this process.

3.7 Conclusion

In this study we have presented mid-IR transient absorption experiments on DCM and its deuterated isotopomer DCM-d6 in two solvents of differing polarity and solvation timescales. Our goal in this experiment was to gain insight into the structural dynamics of the CT species responsible for the long lived fluorescence. Our data on the CN excited and ground state stretches clearly show that the CT state does not involve twisting or some other molecular reshaping occurring at the cyanomethylene end of the molecule. The striking shift in frequency and change in amplitude of the 1495 cm^{-1} mode that occurs subsequent to the formation of the excited state we attribute to formation of the charge transfer state via twisting and pyramidalization of the C-N(Me)$_2$ group, and concomitant changes in C-C bonding character throughout the molecule. The remarkable insensitivity of the frequencies of the CN modes and the 1440 cm^{-1}, 1520 cm^{-1}, and 1590 cm^{-1} modes after excitation along with the solvent-dependent timescales for the shift and amplitude changes in the 1495 cm^{-1} model lead us to rule out vibrational relaxation as the origin of the observed effects. A more quantitative analysis requires much more detailed confrontation of theory and experiment. We hope that the type of sophisticated calculation described by Robb and co-workers for DMABN[36] can be extended, via trajectory studies, to explore the evolution of the vibrational spectra of prototypical molecules exemplifying the complex electronic and structural dynamics exhibited by DCM and DMABN, for example. Such a comparison should enable much closer connection of theory and experiment in the area of conical intersection-mediated excited state dynamics, an area that is revolutionizing the understanding of organic photochemistry.[50]

3.8 Acknowledgements

This work was supported by the NSF. We thank Justin Mynar and Jean M. J. Fréchet for their generous donation of lab space and assistance with the synthesis of the DCM-d6 compound.

3.9 References

1. J. Herbst, K. Heyne and R. Diller, *Science*, 2002, **297**, 822-825.
2. C. Chudoba, A. Kummrow, J. Dreyer, J. Stenger, E. T. J. Nibbering, T. Elsaesser and K. A. Zachariasse, *Chem. Phys. Lett.*, 1999, **309**, 357-363.
3. C. Chudoba, E. T. J. Nibbering and T. Elsaesser, *Phys. Rev. Lett.*, 1998, **81**, 3010-3013.
4. J. Dreyer and A. Kummrow, *J. Am. Chem. Soc.*, 2000, **122**, 2577-2585.
5. C. Ma, W. M. Kwok, P. Matousek, A. W. Parker, D. Phillips, W. T. Toner and M. Towrie, *J. Raman Spectrosc.*, 2001, **32**, 115-123.
6. M. Rini, J. Dreyer, E. T. J. Nibbering and T. Elsaesser, *Chem. Phys. Lett.*, 2003, **374**, 13-19.
7. E. T. J. Nibbering, H. Fidder and E. Pines, *Annual Review of Physical Chemistry*, 2005, **56**, 337-367.
8. Z. G. Liu, Z. J. Chen and Q. H. Gong, *Chin. Phys. Lett.*, 2005, **22**, 1536-1539.

9. B. C. Wang, H. R. Liao, W. H. Chen, Y. M. Chou, J. T. Yeh and J. C. Chang, *Theochem-J. Mol. Struct.*, 2005, **716**, 19-25.

10. D. Berner, H. Houili, W. Leo and L. Zuppiroli, *Phys. Status Solidi A-Appl. Res.*, 2005, **202**, 9-36.

11. T. Mori, H. G. Kim, T. Mizutani and D. C. Lee, *Jpn. J. Appl. Phys. Part 1 - Regul. Pap. Short Notes Rev. Pap.*, 2001, **40**, 5346-5349.

12. C. H. Cheon, S. H. Joo, K. Kim, J. I. Jin, H. W. Shin and Y. R. Kim, *Macromolecules*, 2005, **38**, 6336-6345.

13. M. Meyer and J. C. Mialoco, *Opt. Commun.*, 1987, **64**, 264-268.

14. Y. Ooshika, *J. Phys. Soc. Jpn.*, 1954, **9**, 594-602.

15. N. Mataga, Y. Kaifu and M. Koizumi, *Bull. Chem. Soc. Jpn.*, 1956, **29**, 465-470.

16. E. Lippert, *Z. Naturforsch., A: Phys. Sci.*, 1955, **10**, 541-545.

17. M. Meyer, J. C. Mialocq and M. Rougee, *Chem. Phys. Lett.*, 1988, **150**, 484-490.

18. M. Meyer, J. C. Mialocq and B. Perly, *J. Phys. Chem.*, 1990, **94**, 98-104.

19. S. Marguet, J. C. Mialocq, P. Millie, G. Berthier and F. Momicchioli, *Chem. Phys.*, 1992, **160**, 265-279.

20. J. C. Mialocq, X. Armand and S. Marguet, *J. Photochem. Photobiol., A*, 1993, **69**, 351-356.

21. M. M. Martin, P. Plaza and Y. H. Meyer, *Chem. Phys.*, 1995, **192**, 367-377.

22. T. Gustavsson, G. Baldacchino, J.-C. Mialocq and S. Pommeret, *Chem. Phys. Lett.*, 1995, **236**, 587-594.

23. S. Pommeret, T. Gustavsson, R. Naskrecki, G. Baldacchino and J. C. Mialocq, *J. Mol. Liq.*, 1995, **64**, 101-112.

24. H. Zhang, A. M. Jonkman, P. Vandermeulen and M. Glasbeek, *Chem. Phys. Lett.*, 1994, **224**, 551-556.

25. K. Dahl, R. Biswas, N. Ito and M. Maroncelli, *J. Phys. Chem. B*, 2005, **109**, 1563-1585.

26. E. Abraham, J. Oberlé, G. Jonusauskas, R. Lapouyade and C. Rullière, *Chem. Phys.*, 1997, **214**, 409-423.

27. E. Gilabert, R. Lapouyade and C. Rullière, *Chem. Phys. Lett.*, 1991, **82**, 82-86.

28. M. Hashimoto and H.-O. Hamaguchi, *J. Phys. Chem.*, 1995, **99**, 7875-7877.

29. W. M. Kwok, C. Ma, P. Matousek, A. W. Parker, D. Phillips, W. T. Toner, M. Towrie and S. Umapathy, *J. Phys. Chem. A*, 2001, **105**, 984-990.

30. R. Lapouyade, A. Kuhn, J.-F. Letard and W. Rettig, *Chem. Phys. Lett.*, 1993, **208**, 48-58.

31. W. Rettig and W. Majenz, *Chem. Phys. Lett.Chem. Phys. Lett.*, 1989, **154**, 335-341.

32. J.-M. Viallet, F. Dupuy, R. Lapouyade and C. Rulliere, *Chem. Phys. Lett.*, 1994, **222**, 571-578.

33. J. Oberlé, E. Abraham, G. Jonusauskas and C. Rullière, *J. Raman Spectrosc.*, 2000, **31**, 311-317.

34. W. Rettig and W. Majenz, *Chem. Phys. Lett.*, 1989, **154**, 335-341.

35. E. Abraham, J. Oberlé, G. Jonusauskas, R. Lapouyade and C. Rullière, *J. Photochem. Photobiol., A*, 1997, **105**, 101-107.

36. I. Gomez, M. Reguero, M. Boggio-Pasqua and M. A. Robb, *J. Am. Chem. Soc.*, 2005, **127**, 7119-7129.

37. P. Hamm, R. A. Kaindl and J. Stenger, *Opt. Lett.*, 2000, **25**, 1798-1800.

38. J. M. Drake, M. L. Lesiecki and D. M. Camaioni, *Chem. Phys. Lett.*, 1985, **113**, 530-534.

39. J. Kong, C. A. White, A. I. Krylov, D. Sherrill, R. D. Adamson, T. R. Furlani, M. S. Lee, A. M. Lee, S. R. Gwaltney, T. R. Adams, C. Ochsenfeld, A. T. B. Gilbert, G. S. Kedziora, V. A. Rassolov, D. R. Maurice, N. Nair, Y. H. Shao, N. A. Besley, P. E. Maslen, J. P. Dombroski, H. Daschel, W. M. Zhang, P. P. Korambath, J. Baker, E. F. C. Byrd, T. Van Voorhis, M. Oumi, S. Hirata, C. P. Hsu, N. Ishikawa, J. Florian, A. Warshel, B. G. Johnson, P. M. W. Gill, M. Head-Gordon and J. A. Pople, *J. Comput. Chem.*, 2000, **21**, 1532-1548.

40. H. P. L. P. Flükiger, S. Portmann, J. Weber, 2000.

41. J. Bourson and B. Valeur, *J. Phys. Chem.*, 1989, **93**, 3871-3876.

42. L. L. Woods, *J. Am. Chem. Soc.*, 1958, **80**, 1440-1442.

43. S. Bertrand, N. Hoffmann, S. Humbel and J. P. Pete, *J. Org. Chem.*, 2000, **65**, 8690-8703.

44. I. M. Downie, M. J. Earle, H. Heaney and K. F. Shuhaibar, *Tetrahedron*, 1993, **49**, 4015-4034.

45. M. Maroncelli and G. R. Fleming, *J. Chem. Phys.*, 1987, **86**, 6221-6239.

46. M. L. Horng, J. A. Gardecki, A. Papazyan and M. Maroncelli, *J. Phys. Chem.*, 1995, **99**, 17311-17337.

47. W. Rettig and B. Zietz, *Chem. Phys. Lett.*, 2000, **317**, 187-196.

48. M. Yoshizawa, M. Kubo and M. Kurosawa, *J. Lumin.*, 2000, **87-9**, 739-741.

49. K. Iwata and H. Hamaguchi, *J. Phys. Chem. A*, 1997, **101**, 632-637.

50. A. Migani, Olivucci, M., in *Conical Intersections: Electronic Structure, Dynamics and Spectroscopy*, ed. W. Domcke, Yarkony, D.R., Köppel, H., World Scientific, London, Editon edn., 2004, vol. 15, pp. 271-320.

Chapter 4: Excited State Dynamics of β-apo-8’-carotenal: An Ultrafast Electronic and Vibrational Study

4.1 Abstract.

Results of infrared and visible transient absorption measurements following either two-photon excitation (2PE) to the forbidden S_1 state or one-photon excitation (1PE) to the S_2 state of the carotenoid β-apo-8’-carotenal (Bapo) are presented. The goal of the optical pump mid-Infrared probe technique presented here is to enables the study and comparison of subsequent structural dynamics with and without interference from higher states. The S_1 lifetime of Bapo in chloroform solution is 18 ps following 1PE to S_2, as determined by both visible and infrared transient absorption. A component separate from the S_1 state absorptions was observed in both the electronic and vibrational probe following 2PE directly to the S_1 state. This components of the 2PE absorption spectra had a lifetime of 340 ps in carbon tetrachloride, and was too long-lived to measure in chloroform. This long lived component is not believed to be from triplet formation but instead to be due to radical cation or soliton formation from the S_1 state. The spectra obtained with 1PE to the strongly allowed S_2 state show no measurable signal past 75 ps which is in strong contrast to the directly prepared S_1 state spectra in which we collected strong absorptions at long times but were limited by the 750 ps physical scanning extent of our translation stage. The electronic probe spectra have three absorption peaks between 650-850 nm but have drastically different relative peak heights, suggesting that the S_1 state potential energy surface does not allow populations prepared by one and two photon excitation to reach the same regions of the surface.

4.2 Introduction

Carotenoids play many roles in nature, depending on the structure, properties and integration into protein structures; in plants, they are important in photoprotection,[1, 2] and light-harvesting,[3-5] while in humans they act as antioxidants and provide photoprotection in vision.[6, 7] β-apo-8'-carotenal (Bapo), also known as 8O1β1 using the nomenclature of Polívka and Sundström,[8] is a naturally occurring carotenoid possessing C_s symmetry, most commonly found in citrus fruit skins. In humans, Bapo is produced *in vivo* from enzymatic asymmetric cleavage of β-carotene and can be the starting material for retinal formation.[9] This cleavage leaves the ethylene chain terminated by an aldehyde group, which is included in the conjugated backbone of the molecule. One interesting feature of carbonyl containing carotenoids such as the apo-carotenals and peridinin, is that the S_1 excited state lifetime decreases with increasing solvent polarity.[10-12] The molecular structures of Bapo and β-carotene are shown in Figure 4.1. Bapo, which possesses C_s symmetry (it only has a mirror plane in the plane of the ethylene chain), has been used by several research groups as a model compound to study other carotenoids possessing higher symmetry, including its parent molecule.[10, 13] The ground state (S_0) and first excited singlet state (S_1) of Bapo both possess A' symmetry, while the second excited singlet state (S_2) possesses A'' symmetry, a case analogous to β-carotene in which the S_0 and S_1 states possess A_g symmetry while S_2 is of B_u symmetry. In Bapo the $S_0 \rightarrow S_2$ transition is strongly allowed by symmetry using of one-photon transition excitation (1PE) at 490 nm. The transition from $S_0 \rightarrow S_1$ is

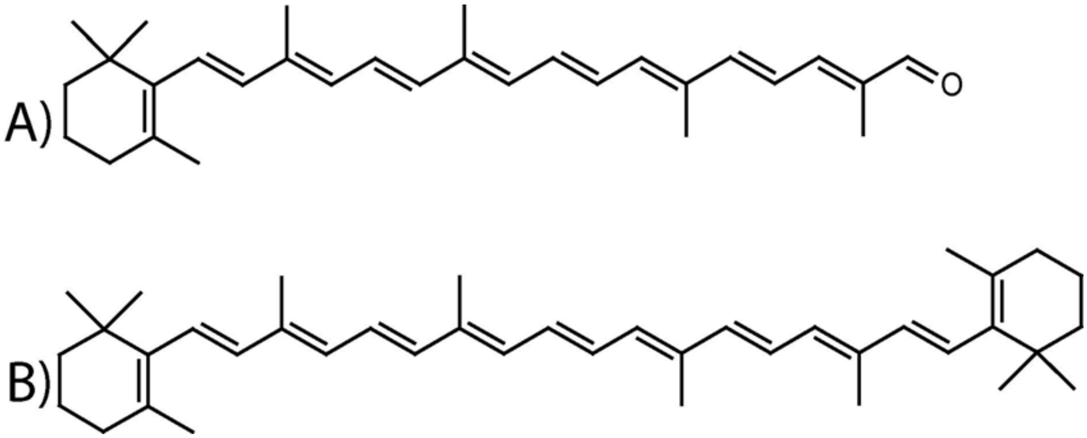

Figure 4.1. Structure of A) β-apo-8’-carotenal which is formed *in vivo* from B) β-carotene.

forbidden by symmetry for one-photon absorption and leads to labeling S_1 as a “dark” state; the transition to S_1 is however allowed by two-photon excitation (2PE). These selection rules are analogous to the case of more highly symmetric molecules, such as β-carotene, which belongs rigorously to the C_{2h} point group, and possess the same symmetry of their electronic states as Bapo; therefore the same electronic selection rules apply.

The energy of the S_1 state may be determined in one of the following ways: probing the $S_2 \rightarrow S_1$ gap via near infrared absorption following 1PE, directly by 2PE, or by measuring the extremely weak fluorescence given off by the S_1 state of carotenoids at low temperatures.[8] However, depending on the method used to measure the position of the S_1 state the energy can vary by as much as 2000 cm^{-1}.[8] Because of this discrepancy, it has been suggested that 1PE and 2PE techniques may populate different regions on the S_1 potential surface.[14]

A second major difference between direct population of the S_1 state by 2PE and population of S_1 after 1PE to S_2 is the excess residual energy (~5000 cm^{-1}) from internal conversion in the latter case. This excess energy may significantly complicate the interpretation of ultrafast studies of structural dynamics in S_1. In this study we compare results of mid-infrared (mid-IR) probing of S_1 following both 1PE and 2PE of Bapo in solution.

4.3 Experimental Methods

The output of a Femtosource Compact Pro Ti:Sapphire oscillator (Femtolasers Produktions, GmbH) was amplified at 1 kHz, using a home-built regenerative amplifier, to produce 40 fs pulses of ~400 μJ centered at 800 nm. One half of the resulting beam is sent into a mid-infrared (mid-IR) optical parametric amplifier (OPA) based upon a two pass near infrared β–Barium Borate (BBO) based OPA followed by independent time synchronization and focusing onto a $AgGaS_2$ difference frequency crystal described elsewhere.[15, 16] The OPA produces a mid-IR pulse of approximately 100 fs and 2 μJ tunable between 3000 cm^{-1} and 1300 cm^{-1}. The remainder of the amplifier pulse is sent to a Quantronix TOPAS near infrared OPA producing 60 fs pulses of ~10 μJ per pulse at 1275 nm for 2PE to the S_1 state. For 1PE to the S_2 state of Bapo, 490 nm light is produced by mixing the TOPAS output with the residual 800 nm pump light in a type-I 1.0 mm BBO crystal and compressing with a prism pair, producing a 60-80 fs 0.8 μJ pulse. The mid-IR beam is then focused using a 15 cm off axis parabolic mirror into a 500 μm path length calcium fluoride flow cell. Detection of the IR beams (signal and reference) was done using of a 2x32 element HgCdTe array detector (Infrared Associates/Infrared Systems Development Corp.) attached to a nitrogen purged, infrared imaging spectrometer (HORIBA Jobin Yvon, Triax 190) with gold optics. Typical sample concentrations for 2PE were ~10^{-3} M (to give an optical density of 4 at the peak visible absorption at 490 nm, measured in a 1mm quartz cell). No change in the shape of the absorption was observed when compared with a 100 fold dilution. Samples were diluted by a factor of four for 1PE. The 1275 nm pump beam wavelength was chosen to produce the maximum signal when probing the $S_1 \rightarrow S_n$ excited state absorption at 545 nm.[10, 17] This beam was focused independently using gold flat mirrors and a fused silica lens adjusted to match the size of the excitation and probing beam waist (~150-200 μm focal spot size in the mid-IR). With this apparatus, we have the ability to record mid-IR spectra at a resolution of 3 cm^{-1} in the ~1400 cm^{-1} fingerprint region increasing linearly to 10 cm^{-1} at 2800 cm^{-1}. Depending only on the grating used, we can collecting from ~100 cm^{-1} to ~320 cm^{-1} at a time. The experiments performed involve either 2PE to S_1 or 1PE to S_2, followed by a vibrational, or white light probe of the excited state dynamics. This allows us to monitor the optically induced electronic and vibrational changes and detect intermediates that form upon relaxation to either photo-products or directly to the ground state.

4.4 Results

Figure 4.1 displays the structure of Bapo, (A), and its parent molecule β-carotene (B), from which Bapo is made *in vivo* from asymmetric enzymatic cleavage. The replacement of the β-ring with an aldehyde group causes the symmetry of Bapo to be decreased from C_{2h} to C_s, while increasing the polarity of the molecule.

Figure 4.2 (A) shows the UV/Vis spectrum of Bapo in CCl_4 (red) and Bapo in $CHCl_3$ (blue). The absorption lineshape of Bapo becomes smoother, due to the loss of vibronic peaks, upon dissolving it in the more polar $CHCl_3$, and is asymmetrically broadened towards the red. Figure 4.2 (B) displays the FTIR spectrum of solid Bapo, deposited from dark prepared $CHCl_3$ solution and evaporated under a stream of nitrogen onto a NaCl window.

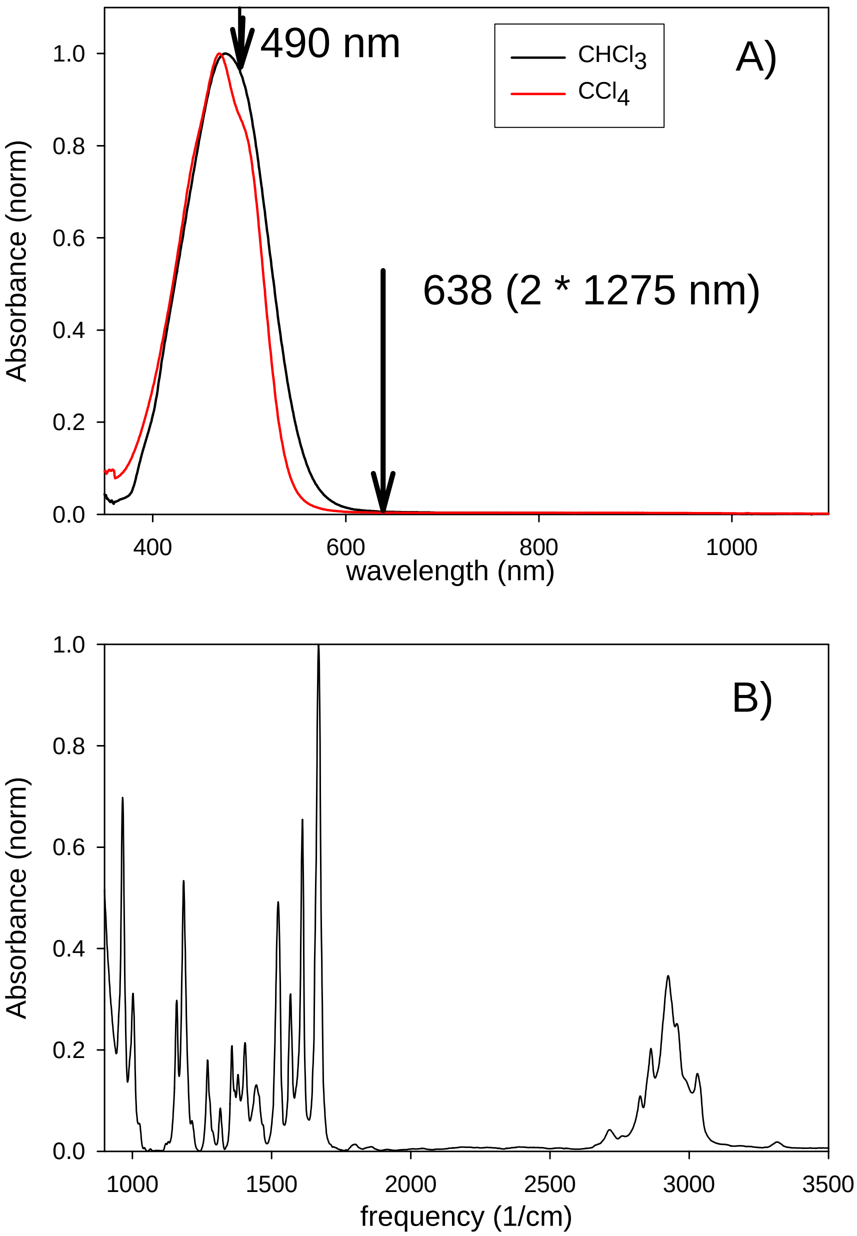

Figure 4.2. A) UV-Vis absorption spectrum of Bapo in chloroform and carbon tetrachloride. The arrows at 490 nm and 638 nm indicate the excitation wavelengths for one- and two photon excitation, respectively B) FTIR spectra of solid Bapo.

Figure 4.3 displays kinetic traces of Bapo in chloroform following excitation; Fits for all the data in Figure 4.3 are collected in Table 4.1. In Figure 4.3(A) the ground state recovery trace of Bapo using a 50 fs, 500 nm pump and 500 nm probe is shown. After a fast solvent spike (~250 fs in all solvents) these kinetic traces decay with a single exponential timescale. In the case of chloroform, whose single exponential fit is shown in red, this timescale is 18.6 ps. Part (B) shows the kinetics of the excited state absorption (ESA) at 545 nm following 2PE using 1275 nm. The three exponential fit to the data is shown in red. The trace has two rising components (negative amplitudes) and one decay component. The rise components of 0.34ps and 4.6 ps contribute nearly the same amount, approximately half, to the trace when normalized to an amplitude of 1 for the decay component of 13.6 ps.

Figure 4.4 displays surface plots created by probing in the mid-IR (1350 -1850 cm^{-1}) following excitation by 1PE (A) or 2PE (B). The time axis is shown from zero to 70 ps delay. These plots are strikingly different; the relative and absolute amplitudes, and lifetimes of all vibrational features are very different, with the 2PE lifetimes being extended by at least an order of magnitude. The 1PE spectrum has its most intense peaks at 1550, 1575 and 1690 cm^{-1} which all decay on roughly an 18 ps timescale, and the amplitude ratio of the ~1700 cm^{-1} to ~1550 cm^{-1} is approximately 3:2. In the 2PE spectrum the most intense band is a long lived 1509 cm^{-1} absorption, which is not evident in the 1PE spectrum; this peak at 1509 cm^{-1} is nearly twice as intense as any other band, and the peak ratio of the 1700 to 1550cm^{-1} bands in the 2PE case is 2:3, the inverse of the 1PE ratio.

GSR (500 nm)						
	a_1	τ_1(ps)	a_2	τ_2(ps)	a_3	τ_3(ps)
CCl_4	2.26	0.27	3.65	27.2		
$CDCl_3$	1.92	0.24	7.74	19.3		
$CHCl_3$	5.64	0.28	4.54	18.6		
2PE ESA (545 nm)						
$CHCl_3$	-0.52	0.34	-0.57	4.6	1	13.7

Table 4.1: Fit parameters to ground state recover kinetics using 500 nm pump 500 nm probe, and excited state absorption kinetics probed at 545 nm following 2PE. Amplitudes a_i are in arbitrary units, times τ_i are in picoseconds.

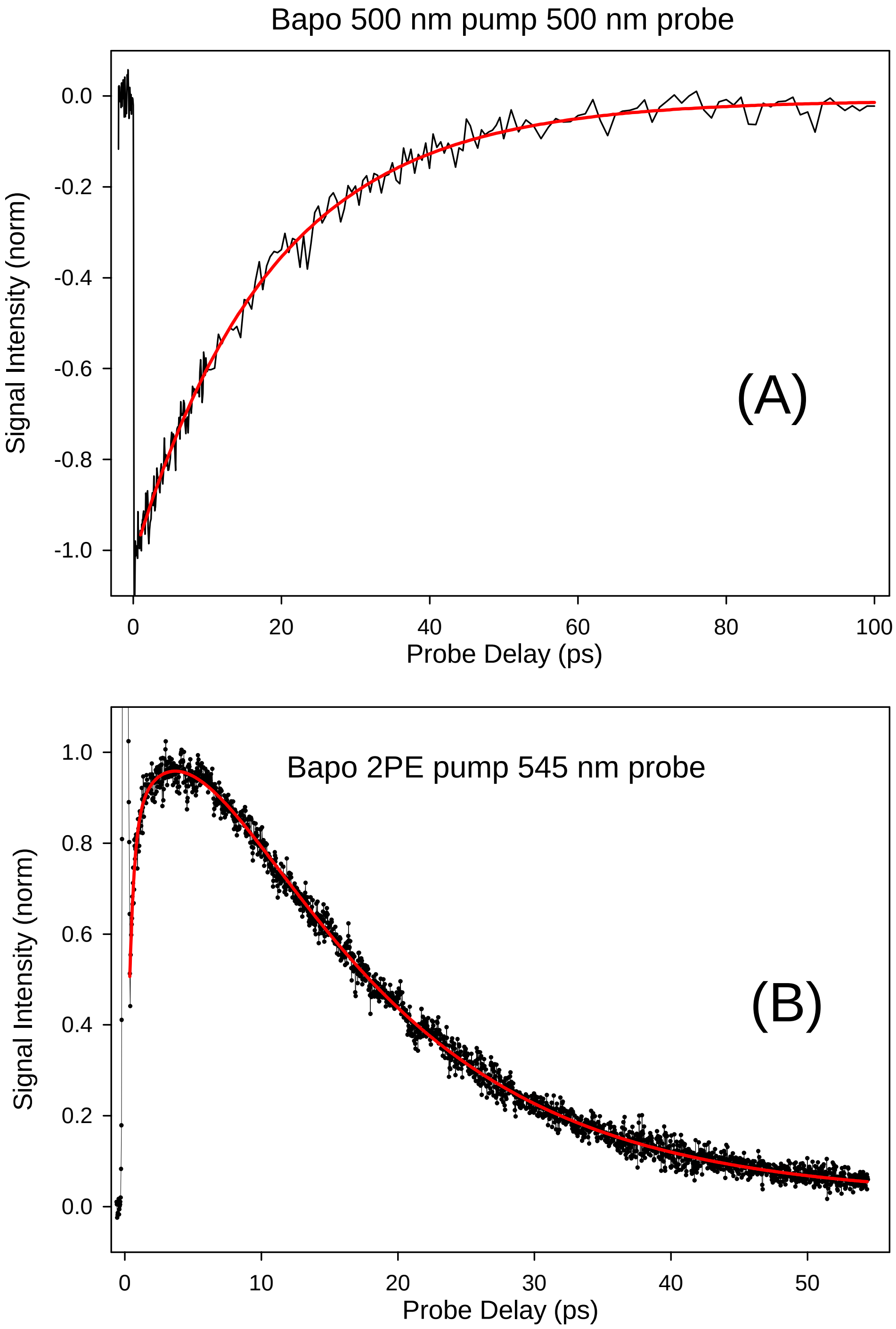

Figure 4.3. (A) Kinetic trace of the ground state recovery of Bapo using 500 nm pump and probe pulses. (B) Kinetic trace of the excited state absorption (S_1-S_n) at 545 nm following 2PE at 1275 nm (B).

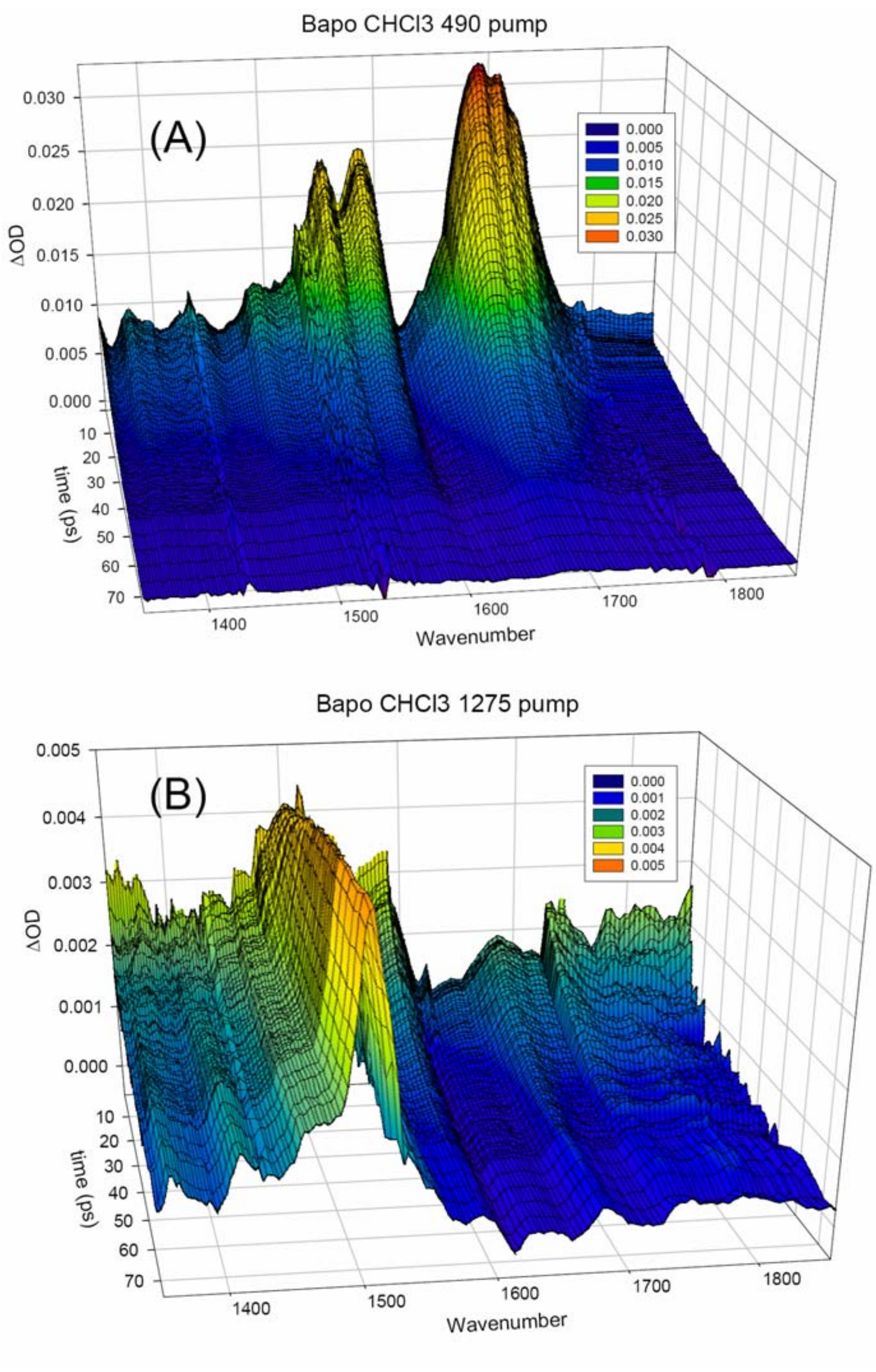

Figure 4.4. Mid-IR excited state infrared absorption of Bapo in $CHCl_3$ shown as a function of time following (A) 1PE at 490 nm and (B) 2PE at 1275 nm.

Figure 4.5 collects time slices of the surface plots in Figure 4.4 to emphasize the differences in their structure. The slices in the 1PE case extend to 75 ps, while the 2PE slices extend to 750 ps. Exponential fit parameters for all bands are collected in Table 4.2. In the 1PE case most bands have a small rise, with a timescale between 1.6 and 4.2 ps, and a single exponential decay between 17.7 and 19.4 ps. However, the 2PE spectrum exhibits substantially longer timescales. The 1509 cm^{-1} band, the largest of those in the 2PE spectrum, has a two exponential rise, with tie constant of 13.5 ps and 125 ps in chloroform. While is it is clear from the data that a decay is present, it is far too long to quantify in 750 ps. For Bapo in CCl_4 (this data is not shown as it is qualitatively identical to that in $CHCl_3$), the 1509 cm^{-1} absorption has a 16.8 ps rise and a 342 ps decay as given in Table 4.2. The majority of the bands in the 2PE spectra including the 1509, 1534, 1584, 1678, 1728 and 2900 cm^{-1} bands have a rise with time constants ranging from 13.5 to 16.2 ps. A few of the bands in the 2PE spectrum have a much shorter rise, specifically the 1412, 1534, 1616 and 2900 cm^{-1} bands which have a risetime ranging from 2.2 to 8.8 ps.

Figure 4.6 shows the power dependence of two bands in the 2PE spectrum. The ordinate is in units of $(\Delta OD/\Delta OD_0)$ and the abscissa is in pump power in units of $(I/I_0)^2$. The blue diamonds are for the 1509 cm^{-1} band, the most intense in the 2PE spectrum, and the pink hollow squares are for the 1584 cm^{-1} band, which is an absorption common to both 1PE and 2PE spectra. Both power dependence fits are linear with the square of the pump power.

Peak (cm^{-1})	a_1	τ_1(ps)	a_2	τ_2(ps)	a_3	τ_3(ps)	a_4	τ_4(ps)
1PE $CHCl_3$								
1489	-9.2	3.9±0.1	1.9 e-2	17.7±0.2				
1589			2.5 e-2	19.4±0.2				
1691	-10	1.6±0.8	3.5 e-2	19.4±0.18				
2450	-4.2	4.2±0.18	1.2 e-2	17.8±0.25				
2952	-5.4	3.5±0.1	1.6 e-2	18.3±0.2				
2PE $CHCl_3$								
1412	0.68	3.0±1.1			-1.4	341±75	1.9	619±98
1509			-0.46	13.5±3.9	-1.1	125±14		
1534	0.31	2.5±0.9	1.4	16.6±2.6				
1584			2.3	17.2±0.42				
1616	1.1	8.8±0.4			0.36	241±43		
1678			1.4	20.2±0.4	0.43	const		
1728			2.3	16.2±1.9	0.20	107±30		
2900	4.2	2.2±0.5	3.7	16.2±1.4				
2PE CCl_4								
1506			-0.79	16.8±0.9	1.1	342±24		

Table 4.2: For parameters to mid-IR probe data at 1PE and 2PE. All amplitudes a_i are in mOD, all times τ_i are in picoseconds.

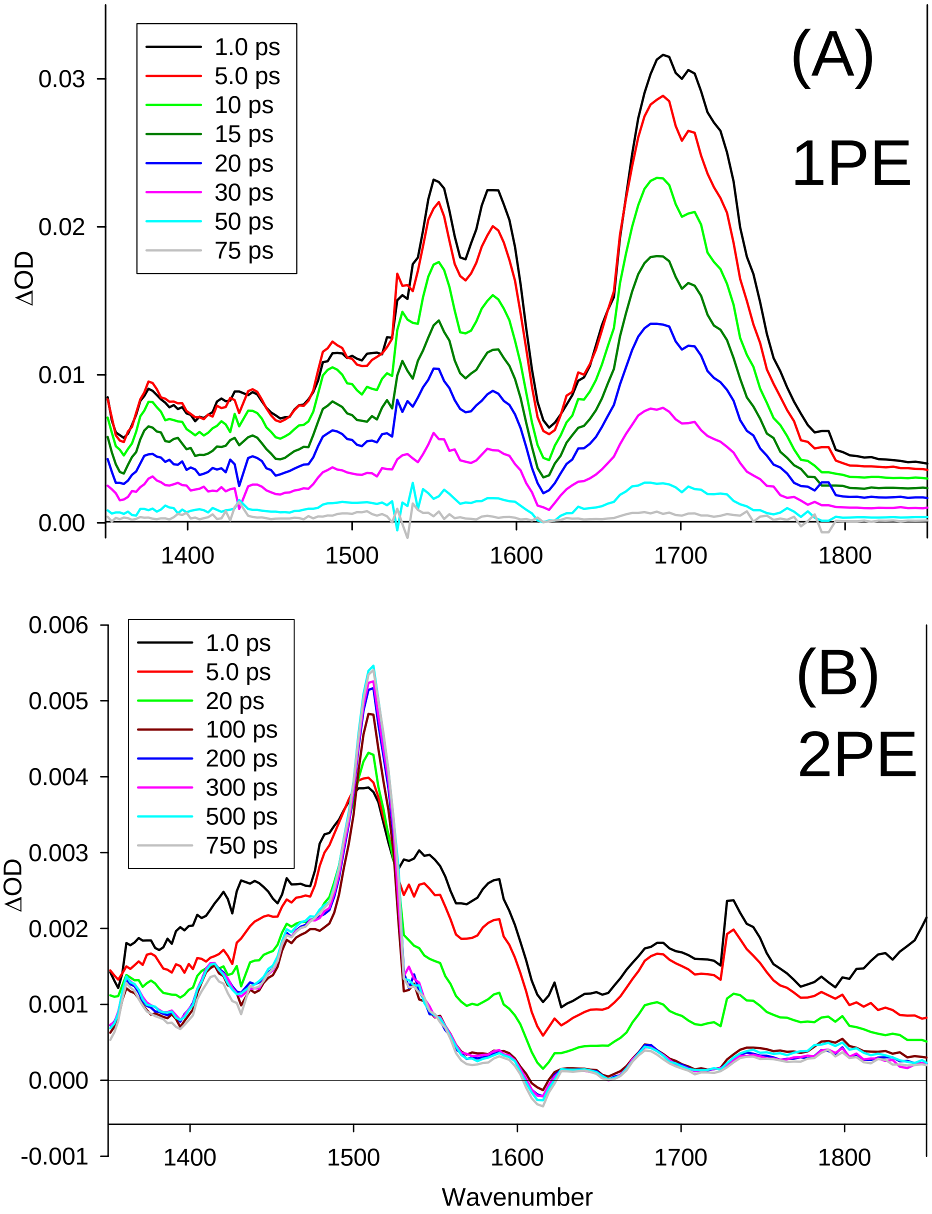

Figure 4.5. Time slices of the surface plots in Fig 4 for Bapo in $CHCl_3$. Note the difference in the timescale of the slices between (A) and (B).

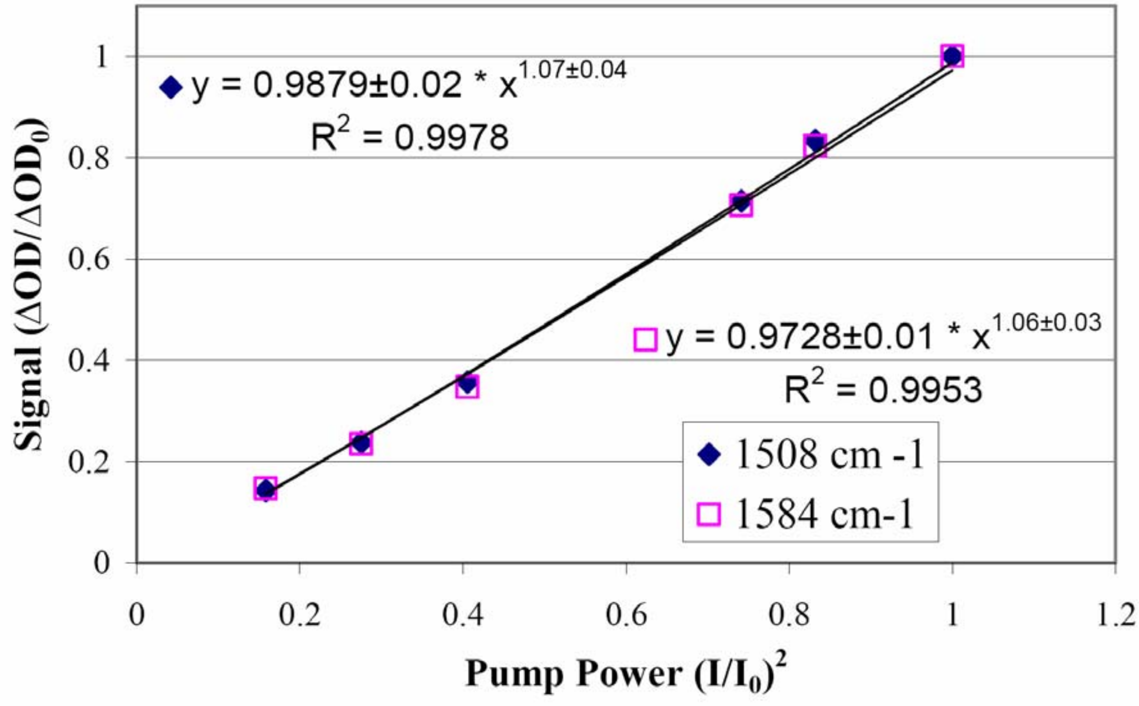

Figure 4.6. Normalized power dependence of the 1509 cm^{-1} (long lived absorption) and 1586 cm^{-1} band (decays primarily on the S_1 lifetime) and power fits to the data showing two-photon behavior on the signal strength.

Figure 4.7 shows an expanded view of the slices shown in Figure 4.5, to a maximum of 3000 cm^{-1}. In this region, a high frequency absorption band is present which is extremely broad and quite intense. For the case of 1PE this band is twice as intense as the absorption in the 1600 cm^{-1} region, and in the 2PE spectrum the absorption peaking near 3000 cm^{-1} is almost as intense as the 1509 cm^{-1} absorption.

Figure 4.8 displays spectra obtained using a white light probe in place of the mid-IR probe used in the previous figures following both 1PE and 2PE. Part (A) displays both spectra at a 25 ps delay. The 1PE spectrum shows three distinct peaks, one centered at 714 nm, one near 764 nm and one at 814 nm. The 2PE spectrum is similar in appearance, with primarily 3 peaks, one broad peak centered near 700 nm, and two extremely narrow peaks: one at 768 nm and the most intense at 835 nm. The peak at 835 nm may be two separate peaks, one at 835 and another at 850 nm. Figure 4.8 (B) shows kinetic traces for the spectra in (A). Since all 1PE kinetic traces have the same qualitative appearance (which is also true for 2PE) only the most intense band is shown for comparison (764 nm for 1PE and 835 nm for 2PE). The 1PE kinetic traces show a fast rise (~2.4-4.0 ps), a decay ranging from 19-24 ps, and a very small rise ranging in timescale from 43 to 250 ps. The 2PE traces show quite different kinetics from the 1PE case. After a rapid rise, the fastest of which is 1.2±0.1 ps and longest of 47±24 ps, there is a long time decay component ranging from 150±71 to 250±7 ps.

4.5 Discussion

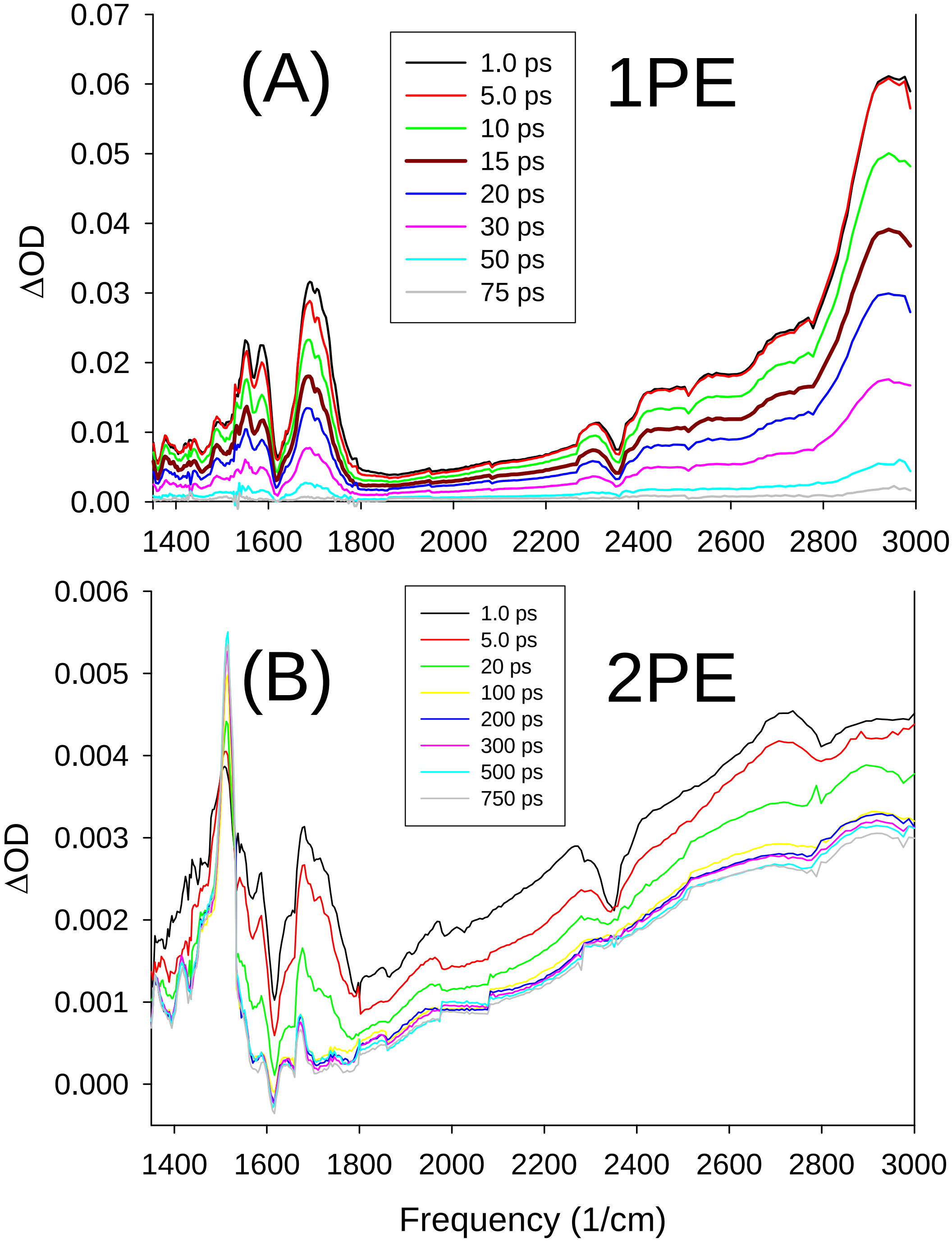

Figure 4.7. Time slices of the infrared data for Bapo in $CHCl_3$ from Fig. 4 extended to higher frequencies. Note the difference in time range between (A) and (B).

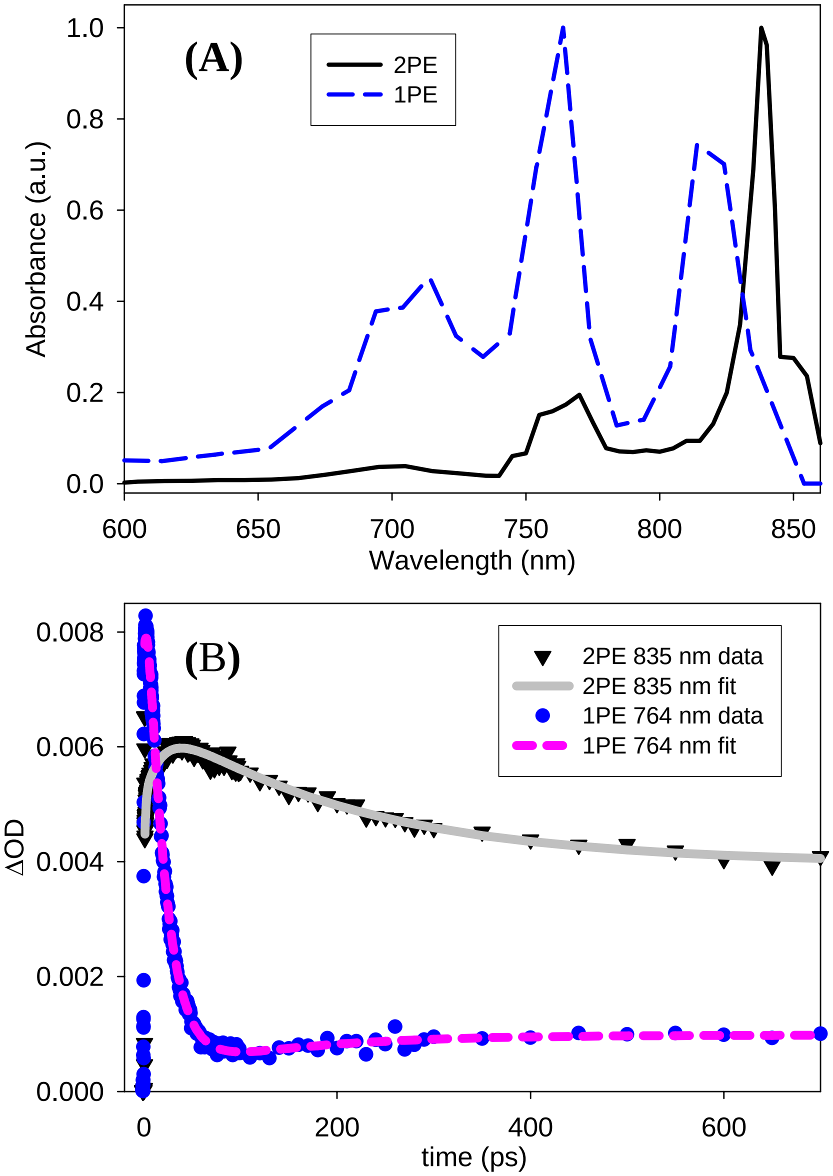

Figure 4.8. (A) Bapo absorption apectra following 1PE and 2PE probe by a white light continuum. The normalized slices shown are taken at 25 ps, the peak of the 2PE intensity. The kinetic traces and fits taken at the maximum absorption from each spectrum 764 nm (1PE), and 835 nm (2PE) are shown in (B). Their exponential fit parameters are collected in Table 4.3.

Table 4.3: Exponential fit parameters for white light probe of Bapo in $CHCl_3$

	a_1	τ_1 (ps)	a_2	τ_2 (ps)	a_3	τ_3 (ps)
1PE						
714 nm	-2.5	3.9±0.12	9	24±1.6	-2	43±10
764 nm	-3	3.8±0.3	10	19±0.7	-7	130±47
814 nm	-1	2.4±0.6	3	19.5±0.6	-0.6	245±45
2PE						
729 nm	-0.2	47±24	0.2	150±71		
768 nm	-0.8	1.2±0.1	0.2	246±7		
835 nm	-1.5	17±0.6	2.0	215±19		

Table 4.3: Exponential fit parameters for 1PE or 2PE pump followed by probing with near-IR light between 700 and 850 nm. All amplitudes a_i are in mOD, all times τ_i are in picoseconds

It has been suggested by Polívka et al that 1PE and 2PE excitation selectively prepare different conformers of carotenoids.[14] This is clearly seen in the fluorescence spectra of short polyenes in free jet expansions. In the absence of collisional vibrational energy redistribution the fluorescence frequency differs by 800 cm^{-1} between 1PE and 2PE.[19] Our infrared spectra are consistent with this notion, and with there being different decay channels for S_1 when excited by 2PE or via S_2 with 1PE. For example, the rise time of the 1509 cm^{-1} band in the 2PE spectrum corresponds to the decay of the S_1-S_n absorption for 2PE. There is no corresponding band in the 1PE spectrum. Figure 4.9 displays a potential energy surface that can help to rationalize these results. 1PE and 2PE allow population of different excited state populations, which result in distinct conformational species upon relaxation.

Several possibilities exist to explain the features we observe, specifically the long lived 1509 cm^{-1} absorption, the broad and intense absorption near 3000 cm^{-1}, and the sharp electronic absorptions near 800 nm. Two of the possible explanations are triplet formation which may explain the 1509 cm^{-1} band, and/or cation radical formation, which could account for the absorptions in the near-infrared. Another possible explanation, which can account for all three features, is soliton formation (such as that seen in conducting polymers), which we tentatively propose as the explanation for the observed features.

We exclude triplet formation as the origin of the 1509 cm^{-1} band, used by

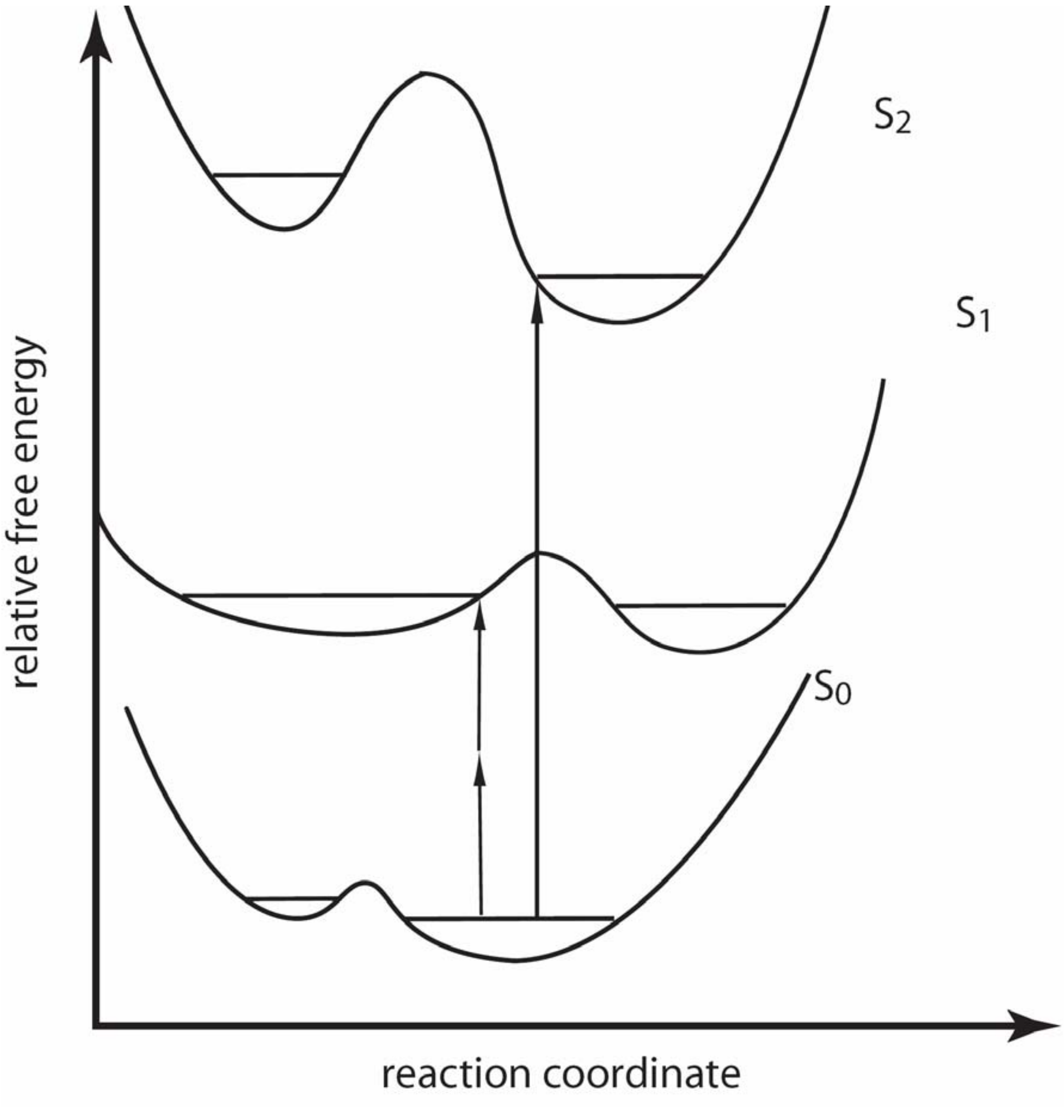

Figure 4.9: Proposed model for the potential energy surfaces along with the one and two-photon transitions to separate portions of their respective excited states.

Hashimoto and Koyama[20] as an explanation of their 1508 cm^{-1} Raman band in n-hexane, for several reasons. Since the intersystem crossing quantum yield to triplet states is on the order of 10^{-3} for carotenoids,[21] and both the 1508 cm-1 band of Hashimoto and Koyama and our 1509 cm-1 band exhibit a much larger quantum yield we cannot attribute the observed bands to triplet formation. We were also unable to detect T_1-T_n absorption at 520 nm, where the triplet is known to absorb, [23] and previously was detectable by Truscott and co-workers only in the presence of a triplet sensitizer probed after a few microseconds delay.[23] Addition of triethylamine (TEA), a triplet quencher,[24-26] in a large excess (150:1 mole ratio) showed no decrease in the mid-IR signal observed. These combined observations strongly suggests that the 1509 cm^{-1} band does not represent triplet formation.

Carotenoid cation radicals, like those produced optically or electrochemically by Kispert, Jeevarajan and co-workers produced,[22, 27] have a broad (~100 nm) electronic absorption spectra that peak near 800 nm.[28] The charge transfer character that Bapo possesses in its excited state, as indicated by the asymmetrically broadened absorption spectra in $CHCl_3$ and the strong dependence of the excited state lifetimes on solvent polarity (a common features among oxygen containing carotenoids and those that possess excited state charge transfer character)[10, 29, 30] would help to stabilize the formation of such a cation radical. Fujii and co-workers have shown that the addition of 0.005:1 mole ratio of TEA completely quenches this.[31] Again the addition of a 150:1 mole ratio of TEA caused only a small (~5%) decrease in the near infrared absorption signal, which corresponds with the amount of dilution (~5%) that occurs. These findings allow us to exclude cation radicals as the source of our induced absorptions.

One possible explanation of both the three narrow and intense electronic absorptions near 800 nm, and the intense broad peak near 3000 cm^{-1} comes from studies of conducting polymers.[32] In conducting polymers of polyacetylene solitons can form by either photexcitation or doping. A soliton, which in polyacetylene manifests as a shape deformation of the C=C backbone when an electron is promoted from the valence to the conduction band. This excitation causes a decrease in the double bond character near the soliton and bond order reversal, i.e. flipping of the double and single bonds, around the shape deformation. A photoinduced soliton produces a counter propagating soliton and anti-soliton, which theory suggests have a a delocalization length on the order of 7-14 carbon atoms.[32] The formation of a soliton causes new absorption bands to appear, the lowest frequency band is located between 800-950 nm, half way between the valence and conduction band, called the mid-gap region. In Bapo the valence to conduction transition would be analogous to a HOMO-LUMO transition. There are typically three or more transitions in this mid-gap region, and in Bapo they would correspond to: HOMO to mid-gap, mid-gap to mid-gap, and mid-gap to LUMO transitions.

In recent years the Su, Schrieffer, and Heeger[33, 34] model of solitons has been extended to shorter chain molecules.[35-38] Garavelli and co-workers have suggested via electronic structure calculations that S_1-S_0 internal conversion occurring via a conical intersection can produce a shape deformation that induces π-diradical (neutral soliton) formation.[37] Bapo, in agreement with classic theory of solitons, should be a long enough conjugated chain to support soliton formation.

A comparison of the 1PE and 2PE electronic absorption spectra in Figure 4.8 shows that both have similar peak positions, whose separation, ~0.2 eV, are similar to that expected from theory. [38] The high frequency peak appears near 2eV (620 nm) with the other peaks separated by ~0.1-0.5 eV with frequency and peak separation changing with soliton type. The 1PE and 2PE spectra also show different relative peak heights suggesting that the detailed geometry of the solitons formed via 1PE and 2PE is different; and that upon relaxation, the 2PE excited molecules form a conformationally new ground state which stabilizes the shape deformation, segregating the solitons, which can recombine only once the all trans conformer is reformed. This conformational change occurs on a 342 ps timescale in CCl_4 and is too slow to measure with our current apparatus in more polar solvents. The potential energy scheme displayed in Figure 4.9 allows two distinct populations to be formed by 1PE and 2PE upon relaxation, with the two populations being separated by a barrier in the ground state.

4.6 Conclusions

In this study, we have presented mid-IR and visible transient absorption experiments on Bapo in chloroform solution using both 1PE and 2PE. Our goal in this experiment was to gain insight into the nature of the S_1 state PES by preparing the one photon forbidden S_1 state directly and via the S_2 state. Both excited state electronic absorption and vibrational absorption yield differing lifetimes for S_1 depending on whether 1PE or 2PE is used. A long lived component, which only appears in the mid-IR absorption spectra for 2PE, is present in both the electronic and vibrational probe spectra. In both the 1PE and 2PE vibrational spectra the S_1 modes appear with identical peak positions and shapes, but with an additional long time component and an additional absorption at 1509 cm^{-1} and incomplete recovery of the ground state bleach near 1610 cm^{-1}. The electronic spectra recorded between 600 and 900 nm are in stark contrast to the observations made with the vibrational spectra, the relative peak heights are drastically different for the 1PE and 2PE spectra, this supports our model of the proposed PES. Different regions of the PES of the S_1 state of Bapo are accessed via 1PE and 2PE, and do not equilibrate indicating that a barrier exists between them. The section accessed by 2PE emphasizes a state which has a long lifetime (>340 ps) decay compared to the S_1 lifetime of 18 ps in $CHCl_3$. This long lifetime and characteristic absorptions of the product state, primarily following 2PE, indicates that the origin of the state is likely due to a photoinduced neutral soliton pair. This pair travels along the polyene backbone, and due to the polarizing effect of the aldehyde group become localized and stabilized at the two ends of the molecule. These results may be evidence that at least from some origins on the S_1 PES of carotenoids, their relaxation causes the formation of π-diradical pairs in the ground state, following the calculations of Garavelli and co-workers.[37]

4.7 Acknowledgements.

This research was funded by the NSF.

4.7 References

1. H. A. Frank, C. A. Violette, J. K. Trautman, A. P. Shreve, T. G. Owens and A. C. Albrecht, *Pure and Applied Chemistry,* 1991, **63**, 109-114.
2. C. S. Foote, *Science*, 1968, **162**, 963.
3. H. A. Frank and R. J. Cogdell, *Photochemistry and Photobiology*, 1996, **63**, 257-264.
4. H. van Amerongen and R. van Grondelle, *J. Phys. Chem. B*, 2001, **105**, 604-617.
5. T. Ritz, A. Damjanovic, K. Schulten, J. P. Zhang and Y. Koyama, *Photosynthesis Research*, 2000, **66**, 125-144.
6. J. M. Stringham and B. R. Hammond, *Nutrition Reviews*, 2005, **63**, 59-64.
7. J. von Lintig, S. Hessel, A. Isken, C. Kiefer, J. M. Lampert, O. Voolstra and K. Vogt, *Biochimica Et Biophysica Acta-Molecular Basis of Disease*, 2005, **1740**, 122-131.
8. T. Polívka and V. Sundström, *Chemical Reviews*, 2004, **104**, 2021-2071.
9. X.-D. Wang, G.-W. Tang, J. G. Fox, N. I. Krinsky and R. M. Russell, *Archives of Biochemistry and Biophysics*, 1991, **285**, 8-16.
10. Z. F. He, D. Gosztola, Y. Deng, G. Q. Gao, M. R. Wasielewski and L. D. Kispert, *J. Phys. Chem. B*, 2000, **104**, 6668-6673.
11. D. A. Wild, K. Winkler, S. Stalke, K. Oum and T. Lenzer, *Physical Chemistry Chemical Physics*, 2006, **8**, 2499-2505.

12. J. A. Bautista, R. E. Connors, B. B. Raju, R. G. Hiller, F. P. Sharples, D. Gosztola, M. R. Wasielewski and H. A. Frank, *J. Phys. Chem. B*, 1999, **103**, 8751-8758.

13. H. Hashimoto, Y. Miki, M. Kuki, T. Shimamura, H. Utsumi and Y. Koyama, *Journal of the American Chemical Society*, 1993, **115**, 9216-9225.

14. T. Polívka, D. Zigmantas, H. A. Frank, J. A. Bautista, J. L. Herek, Y. Koyama, R. Fujii and V. Sundstrom, *J. Phys. Chem. B*, 2001, **105**, 1072-1080.

15. P. Hamm, R. A. Kaindl and J. Stenger, *Opt. Lett.*, 2000, **25**, 1798-1800.

16. A. J. Van Tassle, M. A. Prantil and G. R. Fleming, *J. Phys. Chem. B*, 2006, **110**, 18989-18995.

17. S. Akimoto, I. Yamazaki, T. Sakawa and M. Mimuro, *Journal of Physical Chemistry A*, 2002, **106**, 2237-2243.

18. P. A. Linden, J. Zimmermann, T. Brixner, N. E. Holt, H. M. Vaswani, R. G. Hiller and G. R. Fleming, *J. Phys. Chem. B*, 2004, **108**, 10340-10345.

19. H. Petek, A. J. Bell, Y. S. Choi, K. Yoshihara, B. A. Tounge and R. L. Christensen, *Journal of Chemical Physics*, 1995, **102**, 4726-4739.

20. H. Hashimoto and Y. Koyama, *Chem. Phys. Lett.*, 1989, **162**, 523-527.

21. R. M. Han, Y. S. Wu, J. Feng, X. C. Ai, J. P. Zhang and L. H. Skibsted, *Photochemistry and Photobiology*, 2004, **80**, 326-333.

22. A. S. Jeevarajan, M. Khaled, M. D. E. Forbes and L. D. Kispert, *Zeitschrift Fur Physikalische Chemie-International Journal of Research in Physical Chemistry & Chemical Physics*, 1993, **182**, 51-61.

23. T. G. Truscott, E. J. Land and A. Sykes, *Photochemistry and Photobiology*, 1973, **17**, 43-51.

24. P. Aspari, N. Ghoneim, E. Haselbach, M. vonRaumer, P. Suppan and E. Vauthey, *Journal of the Chemical Society-Faraday Transactions*, 1996, **92**, 1689-1691.

25. R. A. Beecroft, R. S. Davidson, D. Goodwin, J. E. Pratt and X. J. Luo, *Journal of the Chemical Society-Faraday Transactions Ii*, 1986, **82**, 2393-2397.

26. R. W. Yip, Y. L. Chow, Magdzins.Lk and R. O. Loutfy, *Canadian Journal of Chemistry*, 1972, **50**, 3426-&.

27. A. S. Jeevarajan, L. D. Kispert, G. Chumanov, C. Zhou and T. M. Cotton, *Chem. Phys. Lett.*, 1996, **259**, 515-522.

28. A. S. Jeevarajan, L. D. Kispert, N. I. Avdievich and M. D. E. Forbes, *Journal of Physical Chemistry*, 1996, **100**, 669-671.

29. D. Zigmantas, R. G. Hiller, F. P. Sharples, H. A. Frank, V. Sundstrom and T. Polivka, *Phys. Chem. Chem. Phys.*, 2004, **6**, 3009-3016.

30. D. Zigmantas, R. G. Hiller, A. Yartsev, V. Sundstrom and T. Polivka, *J. Phys. Chem. B*, 2003, **107**, 5339-5348.

31. R. Fujii, T. Kusumoto, T. Sashima, R. J. Cogdell, A. T. Gardiner and H. Hashimoto, *Journal of Physical Chemistry A*, 2005, **109**, 11117-11122.

32. A. J. Heeger, S. Kivelson, J. R. Schrieffer and W. P. Su, *Rev. Mod. Phys.*, 1988, **60**, 781-850.

33. W. P. Su, J. R. Schrieffer and A. J. Heeger, *Phys. Rev. B*, 1980, **22**, 2099-2111.

34. W. P. Su, J. R. Schrieffer and A. J. Heeger, *Phys. Rev. Lett.*, 1979, **42**, 1698-1701.

35. F. L. J. Vos, D. P. Aalberts and W. vanSaarloos, *Phys. Rev. B*, 1996, **53**, 14922-14928.

36. F. L. J. Vos, D. P. Aalberts and W. vanSaarloos, *Phys. Rev. B*, 1996, **53**, R5986-R5989.

37. M. Garavelli, B. R. Smith, M. J. Bearpark, F. Bernardi, M. Olivucci and M. A. Robb, *J. Am. Chem. Soc.*, 2000, **122**, 5568-5581.

38. M. Hartmann, M. Schreiber, H. W. Streitwolf and S. Mukamel, *J. Lumines.*, 1995, **66-7**, 97-101.

Chapter 5: Excited State Structural Dynamics of the Charge Transfer State of Peridinin

5.1 Abstract.

We present results of infrared and visible transient absorption measurements of the first excited singlet state (S_1 and $S_{1/ICT}$) of peridinin in methanol, isopropanol and chloroform solution following one-photon excitation, using 490 nm light, to the S_2 state and rapid (~50 fs in methanol) internal conversion. This technique enables the study of subsequent structural dynamics involved in the formation of the charge transfer state. The S_1 lifetime of peridinin in methanol, isopropanol and chloroform is found to be 12, 58, and 79 ps respectively as determined by infrared transient absorption when initially pumped to the S_2 excited state. Our instrument response function, ~150 fs, does not allow us to observe the fast internal conversion to S_1. We observe two formation timescales in the S_1 state. We attribute the shortest timescale to relaxation following internal conversion and the longer timescale to formation of the $S_{1/ICT}$ state.

5.2 Introduction

Carotenoids play many roles in nature, depending on the structure, properties and integration into protein manifold. They are important in photoprotection,[1,2] and light-harvesting;[3-5] they also play an important role in plants by quenching triplet states and radicals.[6] Peridinin, whose structure is shown in Figure 5.1, is an unusual carotenoid, unique in nature as being the only known carotenoid to incorporate three rings into its structure, including one lactone ring connected to the conjugated polyene backbone, as well as allene, epoxide, and carbonyl groups. Peridinin's role in the light harvesting complex peridinin-chlorophyll-protein (PCP) is essential to the survival of

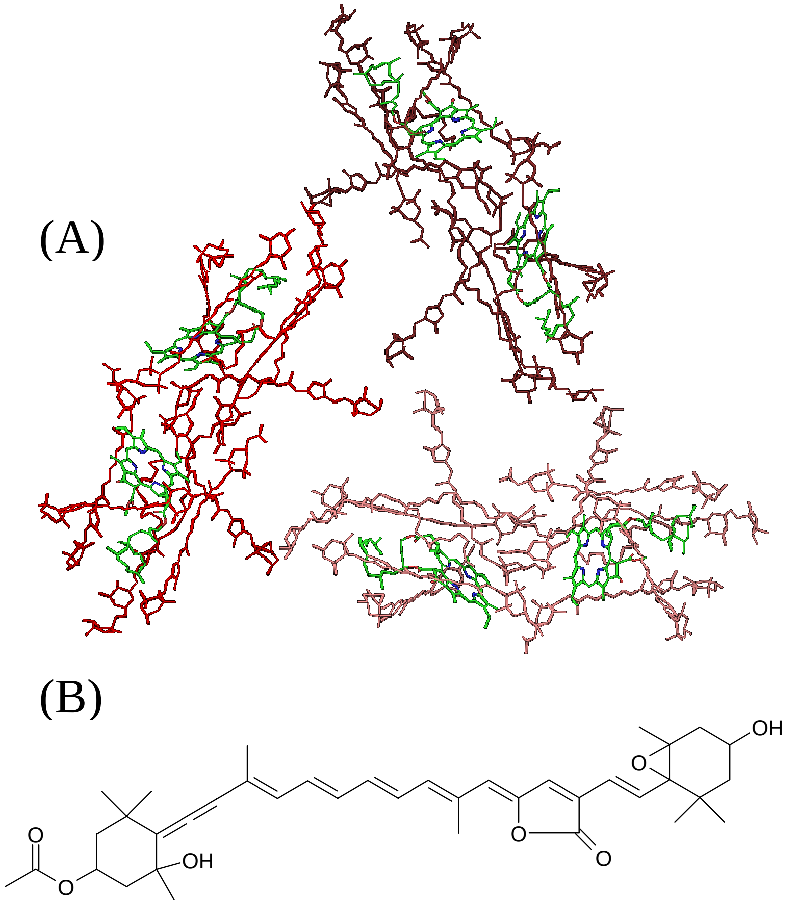

Figure 5.1: The crystal structure of peridinin-chlorophyll-protein chromophores (A), taken from the Protein Database 1PPR, and the molecular structure of peridinin (B).

many dinoflagellates.[7] When the crystal structure of PCP was determined by Hofmann and co-workers,[7] PCP was found to possess a trimeric structure with constituents made up of two chlorophylls, each of which is surrounded by four peridinin molecules. As with most carotenoids, the electronic energy levels can be envisioned to have symmetry corresponding to the idealized C_{2h} point group; that is, the S_0, S_1, and S_2 energy levels belong to the irreducible representations of A_g, A_g, and B_u respectively. These states possess transition selection rules, such that only transitions between A and B and between g and u, are one photon allowed. Because of its deviation from the idealized point group however, relatively strong fluorescence can be measured from the S_1 state[8] and an extremely long lifetime, 103 ps, was measured for this state in CS_2.[9] This lifetime depends strongly on the polarity of the solvent,[10-13] which Frank and co-workers[12] attribute to the existence of an intramolecular charge transfer (ICT) state that strongly couples to the S_1 state, and can be envisioned simply as a conformationally different structure in S_1. In polar solvents this state appears below the S_1 state, while in non-polar solvents the order of these two states is reversed, as demonstrated in the potential energy scheme proposed by Zigmantas et al.[13] This scheme is similar to the one shown in Figure 5.2 where an increase in solvent polarity causes the stabilization of one section on the potential energy landscape of S_1. Vaswani and co-workers[14] substantiate these findings using a dipole in a sphere model demonstrating that the ICT like state is more highly stabilized in polar solvents. Using electron attachment/detachment[15] they also show that the electrons are rearranged in the ICT state, moving density from the ethylene backbone to the epoxide containing ring. As

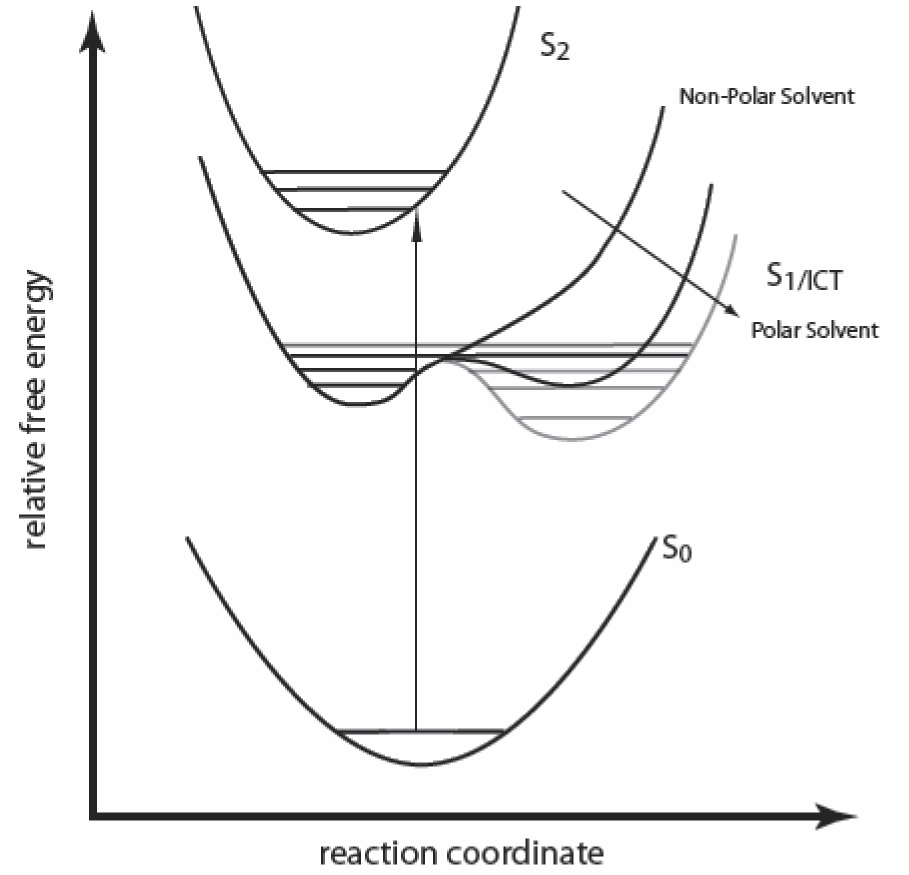

Figure 5.2: Potential energy scheme for peridinin in solution

such this would label modes and allow us to identify those involved the $S_{1/ICT}$ formation using the vibrational technique described below.

5.3 Experimental

5.3.1 Sample Preparation

Peridinin was purified from washed thylakoids of *Amphidinium carterae* (CS-21). Thylakoids were suspended in an aqueous solution of 25 mM Tricine in 10 mM KCl at pH 7.6 and subsequently mixed 75% v/v with solvent B (50% methanol:50% acetonirile). Protein and membrane fragments were removed by centrifugation at 32000 g at 4°C for 20min. The supernatant was applied to a Strata C18-E column (Phenomenex 8B-S001-HCH) and washed with 75% solvent B until all the chlorophyll-c and minor carotenoid degradation products had been removed. Solvent B was increased to 92% and peridinin was eluted followed by diadinoxanthin. The fraction corresponding to the central part of the peridinin peak was evaporated in a gentle stream of nitrogen. Peridinin quantity was determined in ethanol using an E (ml.mg^{-1}) of 132.5. Diadinoxanthin contamination of the peridinin was found by HPLC separation[13] to be minimal and would not contribute to our signal as its absorption band is at much higher frequency than peridinin. Peridinin was dissolved in normal (Sigma HPLC grade) and fully deuterated (Cambridge Isotopes Laboratories Inc.) methanol and isopropanol to give an optical density of 1 in a 500 μm path length cell when measured at 490 nm.

5.3.2 Experimental Apparatus

The output of a Femtosource Compact Pro Ti:Sapphire oscillator (Femtolasers Produktions, GmbH) was amplified at 1kHz, by means of a home-built regenerative amplifier to produce 40 fs pulses of ~400 μJ centered at 800 nm. The resulting beam is then split; one half is sent into a mid-infrared (mid-IR) optical parametric amplifier (OPA)[16,17] composed of a two pass β−Barium Borate (BBO) near infrared OPA followed by independent time synchronization, focusing and difference frequency generation in a $AgGaS_2$ crystal. The OPA produces a mid-IR pulse of approximately 100 fs with 2 μJ of tunable energy between 3000 cm^{-1} and 1300 cm^{-1}. The remainder of the amplifier pulse is sent to a near infrared OPA (Quantronix TOPAS) producing 60 fs pulses of ~18 μJ (combined power of the signal and idler beams at 1275 nm signal beam) per pulse. For one photon excitation (1PE) to the S_2 state of peridinin, 500 nm light is produced by mixing the TOPAS output with the residual 800 nm pump light in a 1.0 mm type-I BBO crystal and compressing with a prism pair, producing a 60-80 fs 0.8 μJ pulse. Although the induced signal was inadequate the retrieve accurate lifetime information we located the S_1 state by means of two photon excitation to be 16100 cm^{-1} in agreement with Zigamtas.[13] The mid-IR beam was focused using a 15 cm off-axis parabolic mirror into a 500 μm path length calcium fluoride flow cell. The IR beams (signal and reference) were measured with a 2x32 element HgCdTe array detector (Infrared Associates/Infrared Systems Development Corp.) attached to a nitrogen purged, imaging spectrometer (HORIBA Jobin Yvon, Triax 190) with gold coated optics. The pump beam was focused independently using flat aluminum mirrors and a fused silica lens adjusted to optimize the size of the excitation and probing beam waist (~150-200 μm focal spot size in the mid-IR). With this apparatus, we have the ability to record mid-IR spectra at a resolution of 3 cm^{-1} in the ~1400 cm^{-1} fingerprint region with resolution increasing linearly to 10 cm^{-1} at 2800 cm^{-1}, depending only on the grating used, collecting from ~100 cm^{-1} to ~320 cm^{-1} at a time. The experiments performed involve one-photon excitation to the S_2 state, followed by a vibrational probe of the excited state dynamics using the described apparatus. This scheme allows us to monitor the optically induced vibrational changes and detect intermediates that form upon relaxation to either photo-products or directly to the ground state.

5.4 Results

Figure 5.1 (A) shows the crystal structure of the organic component of PCP (A), (protein database identifier 1PPR), showing the trimeric structure of the protein chlorophylls, which are colored green, and peridinin molecules, which are colored in different shades of red for each monomer. The molecular structure of free peridinin is shown in Figure 5.1 (B). Figure 5.2 displays the proposed potential energy diagram. This diagram is analogous to the schemes proposed by Zigmantas et al[18] in which the $S_{1/ICT}$ state is stabilized and lowered in energy in more polar solvents. Figure 5.3 (A) shows the visible absorption of peridinin in n-hexane, 2-propanol, and methanol. The loss of vibronic structure upon increasing polarity is a common occurrence in carotenoids that possess carbonyl groups and ICT character in the excited state.[19] In peridinin the visible absorption (due to the S_0-S_2 transition) takes on an asymmetrically

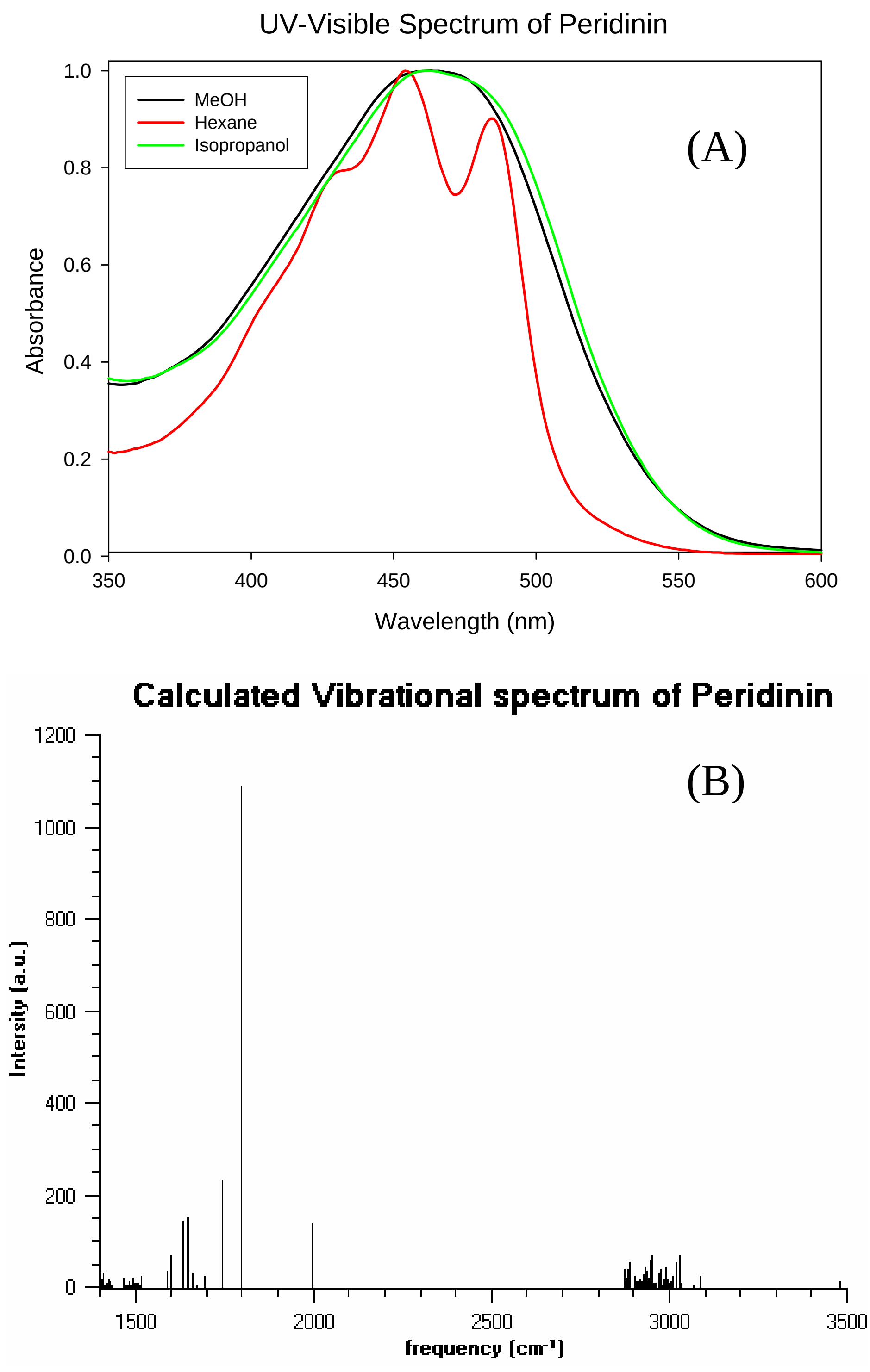

Figure 5.3: UV-Vis absorption spectrum of peridinin in various solvents (A) and calculated infrared spectrum of peridinin (B).

broadened character, especially in solvents capable of forming hydrogen bonds with the carbonyl groups.[18] The formation of hydrogen bonds helps to stabilize the charge transfer character of the electronic state.[10,12,13,18-22] Figure 5.3 (B) displays the vibrational spectrum of peridinin calculated using Q-Chem 2.1[23] HF 3-21g basis set, and scaled by the appropriate factor (0.9085). A previous investigation reported the following bands in the FTIR spectrum in chloroform as 3425 (OH), 2959, 2922 and 2853 (CH), 1929 (allene), 1741 (C=O, acetate), 1642, 1521, 1456 (CH_2), 1369 (geminate CH_3), 1253 (C-O, acetate), 1162, 1125, 1030, and 985 cm^{-1} (trans C=C).[24] Our virbrational frequency calculations confirm their assignments, with the addition of the C=O of the lactone ring with a frequency 50 wavenumber higher (calculated to be 1814 cm^{-1}) than the C=O frequency (calculated 1758 cm^{-1}). Figure 5.4 displays surface plots of peridinin dissolved in either h4-methanol or d4-methanol, with regions of strong solvent absorption omitted. In order to emphasize the infrared absorptions, frequency slices taken at several different time delays are displayed in Figure 5.5. Our time resolution does not allow us to observe internal conversion from S_2 to S_1, reported to occur in 56 fs when the rise of the S_1-S_n excited state absorption is probed.[18] Infrared absorptions appear at 1550, 1642, 1728, 1860 cm^{-1}, and a very broad absorption spans the region between 2000 to 2300 cm^{-1}. The kinetics of these bands are collected in Table 5.1; the data was fit by convolving our instrument response function with either one or two exponential decays. In the cases where two timescales are necessary, the first corresponds to a rising component, except for the chloroform absorption at 1630-1650 cm^{-1} . The vibrational features that appear can be collected into two groups based on the presence, or lack, of a measurable rise component. The first group of bands at

Wavenumber	**a_1(mOD)**	**τ_1 (ps)**	**a_2(mOD)**	**τ_2 (ps)**
d4-MeOH				
1550	-0. 2	0.5±0.09	6	12.0±0.4
1642	-4	0.5±0.05	11	12.0±0.5
1728			10	10.1±0.2
1860			4	7.7±0.1
h4-MeOH				
2300	-1	0.6±0.08	6	9.0±0.05
d8-Isopropanol				
1540	-7	2.4±0.1	41	58±0.3
1624	-12	2.7±0.15	58	56±0.5
1720	-10	1.6±0.05	28	55±0.4
1861	-12	1.1±0.07	9	56±0.4
2900	-2	2.9±0.4	12	56±0.8
h8-Isopropanol				
2440	-2	3.0±0.3	11	46±0.5
$CHCl_3$				
1442	-0. 3	1.5±0.3	2	79±10
1479	-0. 8	4.2±0.7	3	66±12
1532	-0. 4	2.4±0.8	5	66±19
1630-1650	1.1	18±1.0	3	54±13
1732	-0.14	1.2±0.6	3	67±10
2930	-0.5	7.6±1.1	2	58±9

Table 5.1: Exponential fit parameters of all prominent induced absorption features for peridinin dissolved in methanol, isopropanol and chloroform. All amplitudes a_i are in units of mOD and timescales τ_i are in ps.

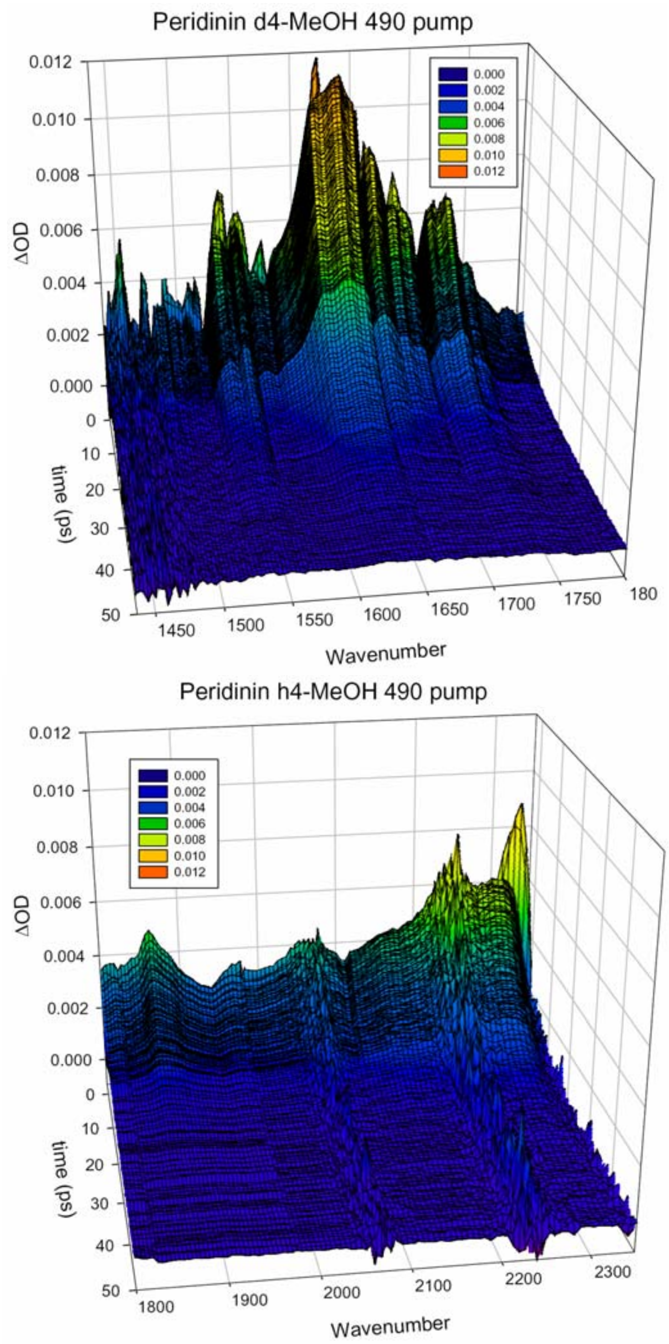

Figure 5.4: Transient absorption spectra of peridinin with 490 nm pump and mid-infrared probe in (A) d4-methanol and (B) h4-methanol. The spectra are plotted on the same ΔOD scale and are of different spectral regions due to strong solvent absorptions.

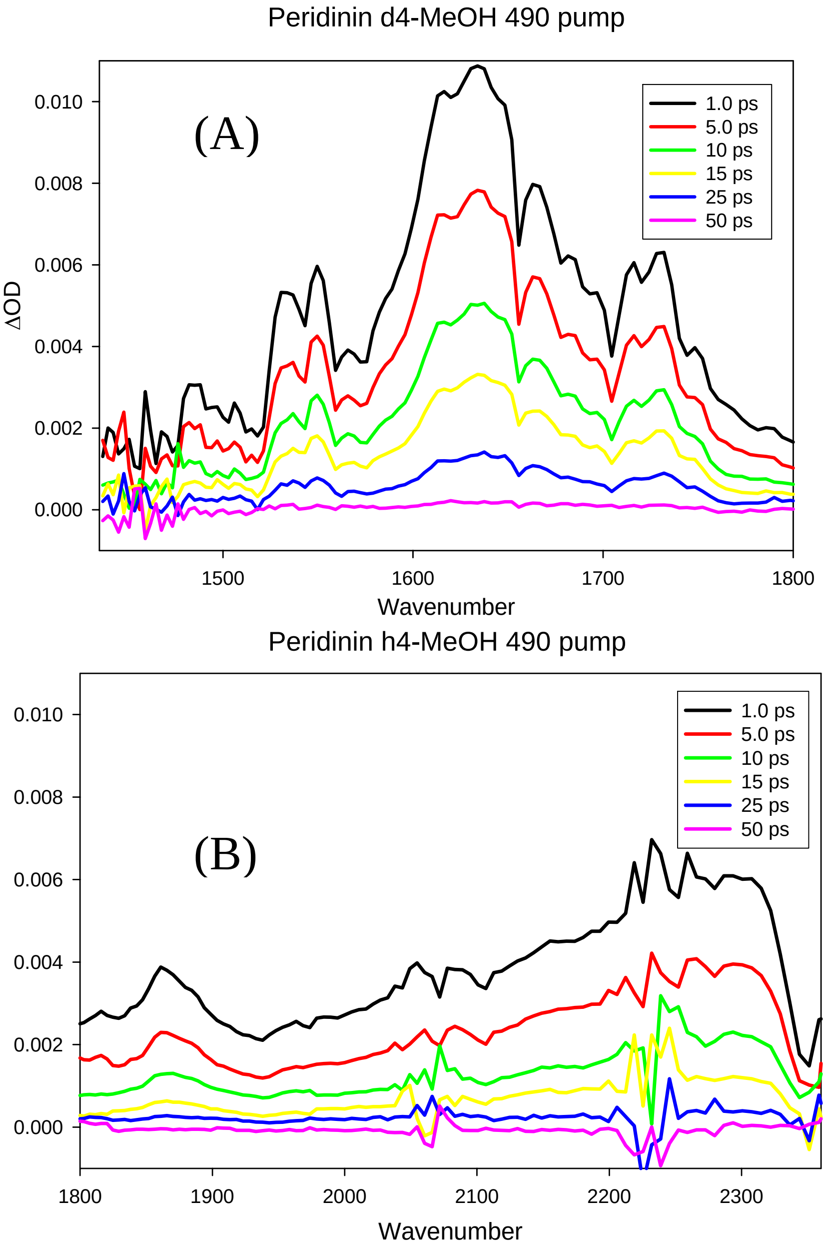

Figure 5.5: Time slices of the transient absorption spectra of peridinin with 490 nm pump and mid-infrared probe in A) d4-MeOH and B) h4-MeOH. The spectra are plotted on the same ΔOD scale and are of different spectral regions due to strong solvent absorptions.

1550, 1642, and 2300 cm^{-1} all rise with a timescale of 500±0.09 to 600±0.08 fs. While the 1550 and 1642 cm^{-1} bands decay with a 12±0.5 ps timescale in d4-methanol, the 2300 cm^{-1} band decays on 9±0.05 ps in h4-methanol. In the other group of absorption bands at 1728 and 1860 cm^{-1}, we were unable to resolve any negative amplitude. The 1728 cm^{-1} absorption decays with a 10.1±0.2 ps timescale and the 1860 cm^{-1} absorption has a 7.7±0.1 ps lifetime.

Figure 5.6 displays surface plots analogous to Figure 5.4 for (A) d8-isopropanol and (B) h8-isopropanol. Frequency slices are again collected in Figure 5.7 for emphasis. Features appear in isopropanol at similar vibrational frequencies to those in methanol, but the lifetimes increase dramatically. Bands appear at 1540, 1624, 1720, 1861, and 2440 cm^{-1}; the solvent absorption of d8-isopropanol allows us to collect an additional region at 2900 cm^{-1} for comparison to the 2440 cm^{-1} band in h8-isopropanol. As in the methanol, the vibrational bands in isopropanol can be divided into two groups by their rise times. The first group, including the 1540, 1624, and >2000 cm^{-1} bands, all rise on a timescale of 2.4±0.1 to 3.0±0.3 ps, as shown in Table 5.1. The vibrations at 1720 and 1861 cm^{-1} have a much shorter rise than the other group of vibrations, 1.6±0.05 ps in the case of the 1720 cm^{-1} band and 1.1±0.07 ps for the 1861 cm^{-1} vibrational band. The bands all decay on the same timescale in d8-isopropanol, ~56 ps, and the broad absorption lifetime in h8-isopropanol is approximately 10 ps shorter, fitting to 46 ps, which is likely due to the deuterium isotope effecting the coupling of solvent and solute molecules.

Figures 5.8 and 5.9 display the surface plot and frequency slices of peridinin in chloroform. In the much less polar solvent chloroform, peridinin exhibits several

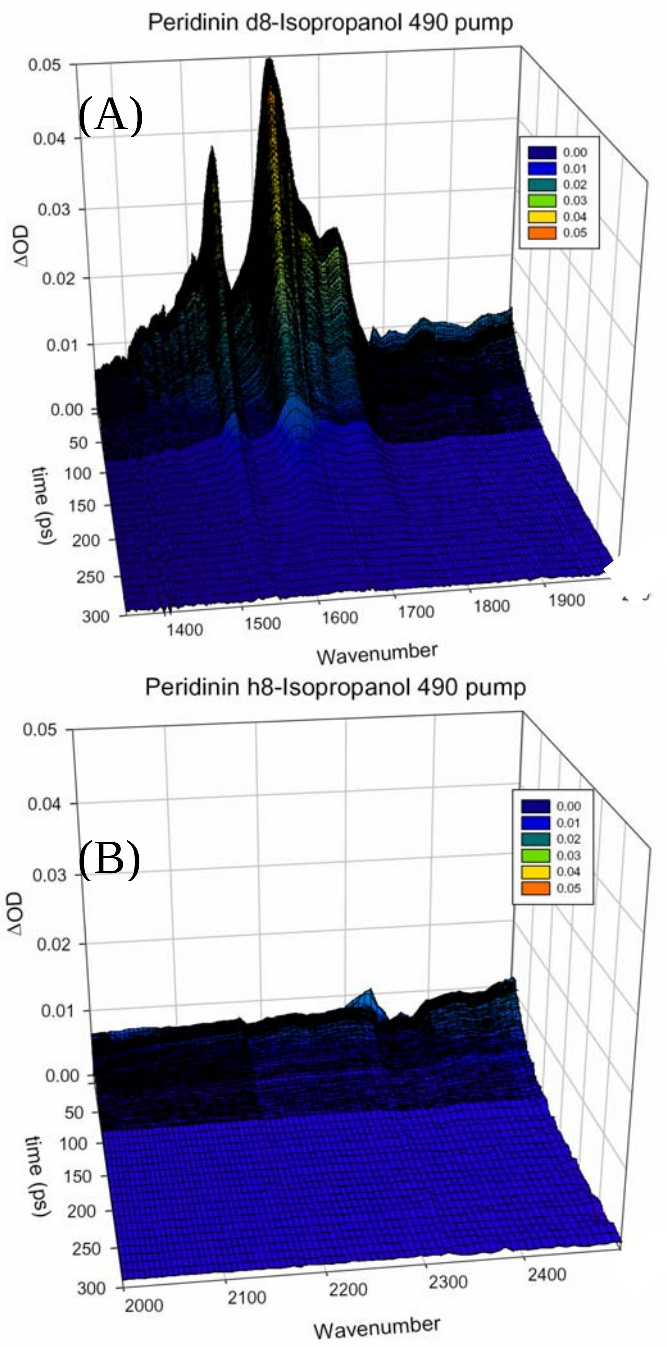

Figure 5.6: Transient absorption spectra of peridinin with 490 nm pump and mid-infrared probe in (A) d8-isopropanol and (B) h8-isopropanol. The spectra are plotted on the same ΔOD scale and are of different spectral regions due to strong solvent absorptions.

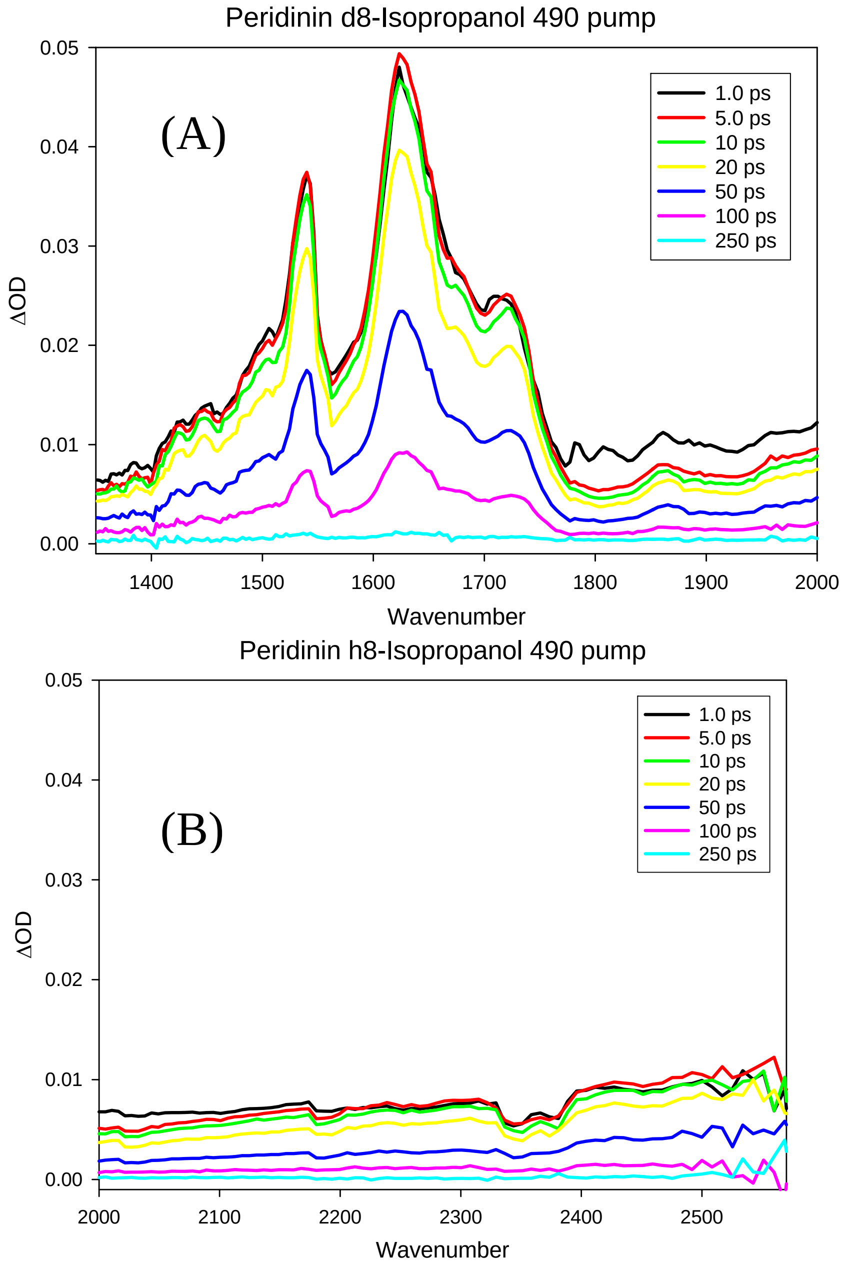

Figure 5.7: Time slices of the transient absorption spectra of peridinin with 490 nm pump and mid-infrared probe in (A) d8-isopropanol and (B) h8-sopropanol. The spectra are plotted on the same ΔOD scale and are of different spectral regions due to strong solvent absorptions.

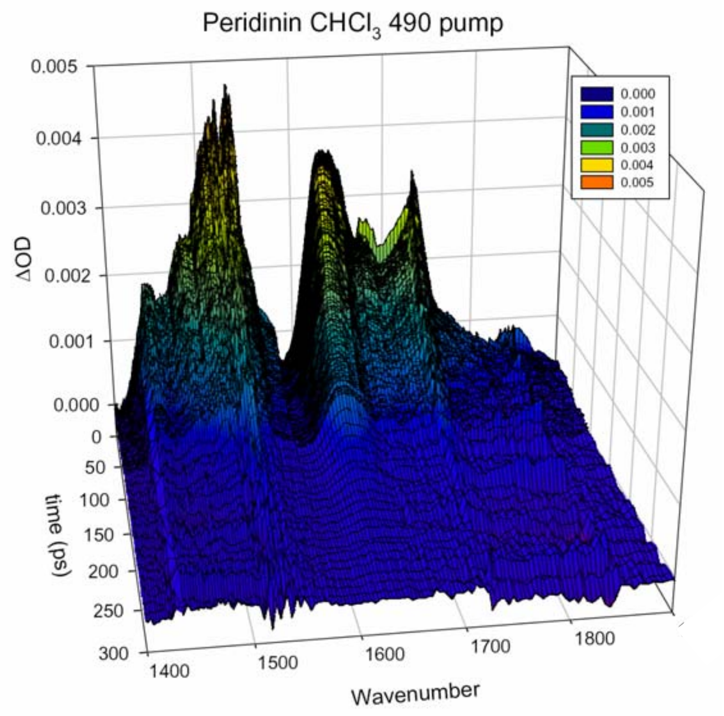

Figure 5.8: Transient absorption spectra of peridinin with 490 nm pump and mid-infrared probe in $CHCl_3$.

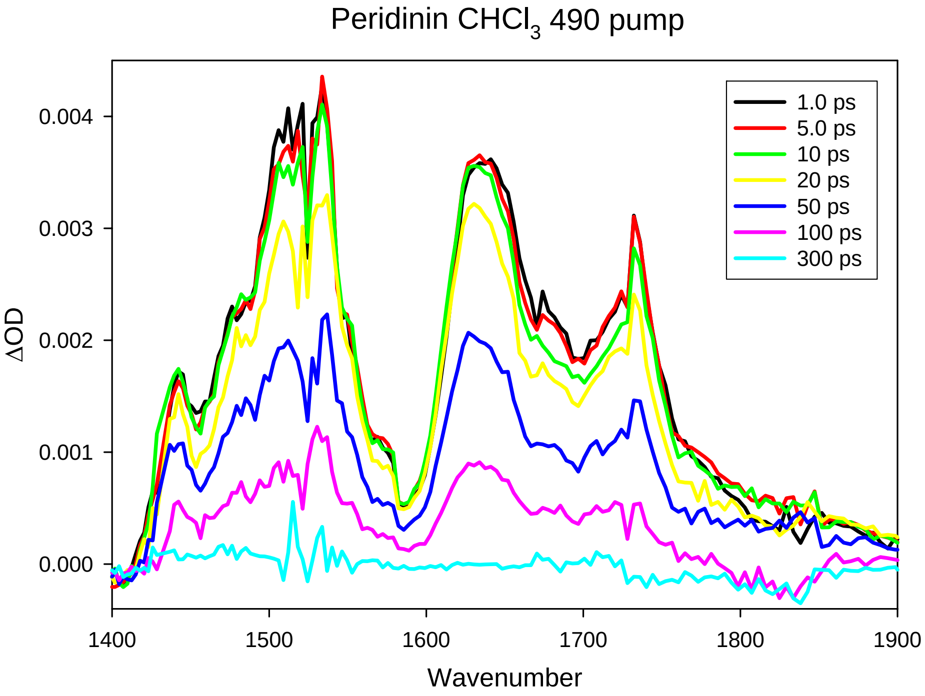

Figure 5.9: Time slices of the transient absorption spectra (from figure 5.8) of peridinin with 490 nm pump and mid-infrared probe in $CHCl_3$.

different behaviors than in methanol and isopropanol. One significant difference is that peridinin is not nearly as stable in chloroform. While no changes in absorption were found during our experiments in methanol and isopropanol, long scans in chloroform were not possible due to large degradation of the peridinin sample (as monitored by UV/Vis absorption). The samples were refreshed as soon as degradation was observed to avoid contributions from the photodegraded products. Similar absorption features to the alcohols are found in chloroform, most notably induced absorptions at 1450, 1510-1520, 1630 and 1725 cm^{-1}. While the most intense feature in the alcohols was the ~1630 cm^{-1} absorption, the ~1510 cm^{-1} band in chloroform is the most intense, and no broad absorption appears above 2000 cm^{-1}. The band at ~1645 cm^{-1} in addition to simply decaying, red shifts in center frequency by approximately 15 cm^{-1} to a terminal value of 1630 cm^{-1}. To extract the contributions from shifting and pure intensity dynamics, the surface from 1590 to 1675 cm^{-1} was fit with a Gaussian function that was allowed to shift in frequency. We find that the band shifts with a timescale of 5.4 ps, and is likely due in some part to intramolecular vibrational redistribution or vibrational cooling to a much less stabilized $S_{1/ICT}$ state. The fact that we observe similar features in the chloroform spectra is likely due to the fact that while non-polar, chloroform still has the ability to form hydrogen bonds with the carbonyl moiety of peridinin allowing for some small contribution to ICT formation similar to that found in the more polar alcohols.

5.5 Discussion

While our single decay timescale do not match the finding of Zigmantas et al.[18] (they are able to fit the decay to two timescales give 4.5 and 10.5 ps in methanol using a global fitting algorith), our findings do agree with their conclusion, that in solution multiple conformers of peridinin exist. We find primarily two populations in the S_1, and $S_{1/ICT}$ state. Most likely what we are observing is the branching of internal conversion from S_2 into (1) the S_1 state without extensive ICT and (2) the formation of the $S_{1/ICT}$. We measure ICT formation timescales of 0.5 ps in methanol and ~2-3 ps in isopropanol, which are in very close agreement to the ICT formation times found by Zigmantas and co-workers.[13,18] The decay route involving just S_1 state dynamics is characterized by the 1728 and 1860 cm^{-1} bands in d4-methanol which do not show a rise other than instrument response. These bands have a ~9 ps decay which we set as the S_1 state in d4-methanol. The second observed decay route is mapped with the 1550, 1642 cm^{-1} bands in d4-methanol and the 2300 cm^{-1} peak in methanol. These three absorptions show a ~0.5 ps rise which we characterize as the charge transfer state formation, and a decay of 12 ps in d4-methanol, 9 ps in h4-methanol, which we set as the charge transfer state lifetime. The lifetime of the charge transfer state is slightly shorter in h4-methanol due to deuterium effects which are also seen in h8-isopropanol.

A similar branching scheme was observed in d8- and h8-isopropanol. The absorptions at 1540, 1624, and 2900 cm^{-1} in d8-isopropanol and the 2440 cm^{-1} band in isopropanol have a rise of ~2.7 ps and a decay of 56 ps in d8-isopropanol and 46 ps in h8-isopropanol. We attribute these absorptions to the charge transfer state formation and decay. The absorptions at 1720 and 1861 cm^{-1} show a shorter rise, 1.6 and 1.1 ps respectively, with a decay of 56 ps and are attributed to the S_1 state only. These absorptions in isopropanol are located in similar positions as those found in methanol leading us to be believe that the same effect is occurring in both solvents.

The shifting of the center frequency of the ~1630 cm^{-1} band observed in chloroform is most likely due to formation of the ICT state, in direct competition with direct internal conversion to the ground state. As illustrated in the potential energy diagram in Figure 5.3, in less polar solvents the $S_{1/ICT}$ state lies at a different position on the S_1 state with a broadened potential well such that the vibrational modes associated with it would be of lower frequency than those that appear in the polar alcohols. This is in agreement with our observation that the frequency of the ICT vibration in chloroform undergoes a red shift. The signals we observe are comprised of several groups representing the different populations forming on the excited state manifold.

The frequencies that we observe in our experiments match normal modes, calculated using the HF/3-21G basis set in Q-Chem involving the epoxide containing cyclohexane ring, and no other part of the molecule. These modes are localized on the same atoms that are identified Vaswani and co-workers,[14] using electron attachment plots, as belonging to the ICT state of peridinin in both solution and PCP.

Their calculations find that there exists a distinct charge transfer state in addition to the S_1 state and S_2 states. [14] Also, the study by Zigmantas and coworkers found a $S_{1/ICT}$ state with a single lifetime[13,18] which is what we observe, especially in isopropanol, for the S_1 and the $S_{1/ICT}$ routes. Our results are consistent with the first excited singlet potential energy surface having an S_1 region with little charge transfer character and an ICT region. Both states are formed following decay from S_2 and that the degree of ICT formation is determined primarily by the solvent polarity.

5.6 Conclusions

In this study, we have presented optically induced mid-IR transient absorption experiments of peridinin in methanol, isopropanol and chloroform solutions using one-photon excitation to the S_2 excited state followed by fast internal conversion to the first excited state S_1. Our goal in this experiment was to gain insight into the structural nature of the $S_{1/ICT}$. Our vibrational probe technique allows for measurement of induced vibrational features following visible excitation. In our solvents, peaks appear with similar peak positions and shapes, the alcohols have different peak ratios than the less polar chloroform. This fact along with lifetime analysis allows us to separate vibrational features formed directly from internal conversion from S_2, those located between 1700-1900 cm^{-1} and those involved in formation of the $S_{1/ICT}$ state, located between 1500-1650 and above 2000 cm^{-1}. Those frequencies associated with formation of the charge transfer state have been identified as being located on the epoxide containing cyclohexane ring, by means of theoretical normal mode calculations, and match the changes in electron density that Vaswani and co-workers assigned using attachment/detachment calculation. While insight into the solution phase aids in the understanding of the structural characteristics of the charge transfer state, more in depth experiments on the entire PCP complex must be undertaken in order to coalesce our current findings with peridinin's biological dynamics.

5.7 Acknowledgements

This research was funded by the NSF. Peridinin samples were provided by Prof. Roger Hiller

5.8 References

1. Frank, H. A.; Violette, C. A.; Trautman, J. K.; Shreve, A. P.; Owens, T. G.; Albrecht, A. C. *Pure and Applied Chemistry* **1991**, *63*, 109.
2. Foote, C. S. *Science* **1968**, *162*, 963.
3. Frank, H. A.; Cogdell, R. J. *Photochemistry and Photobiology* **1996**, *63*, 257.
4. van Amerongen, H.; van Grondelle, R. *Journal of Physical Chemistry B* **2001**, *105*, 604.
5. Ritz, T.; Damjanovic, A.; Schulten, K.; Zhang, J. P.; Koyama, Y. *Photosynthesis Research* **2000**, *66*, 125.
6. Demmig-Adams, B.; Adams, W. W. *Trends in Plant Science* **1996**, *1*, 21.
7. Hofmann, E.; Wrench, P. M.; Sharples, F. P.; Hiller, R. G.; Welte, W.; Diederichs, K. *Science* **1996**, *272*, 1788.
8. Mimuro, M.; Nagashima, U.; Takaichi, S.; Nishimura, Y.; Yamazaki, I.; Katoh, T. *Biochimica Et Biophysica Acta* **1992**, *1098*, 271.
9. Akimoto, S.; Takaichi, S.; Ogata, T.; Nishimura, Y.; Yamazaki, I.; Mimuro, M. *Chemical Physics Letters* **1996**, *260*, 147.
10. Bautista, J. A.; Connors, R. E.; Raju, B. B.; Hiller, R. G.; Sharples, F. P.; Gosztola, D.; Wasielewski, M. R.; Frank, H. A. *Journal of Physical Chemistry B* **1999**, *103*, 8751.

11. Bautista, J. A.; Hiller, R. G.; Sharples, F. P.; Gosztola, D.; Wasielewski, M.; Frank, H. A. *Journal of Physical Chemistry A* **1999**, *103*, 2267.

12. Frank, H. A.; Bautista, J. A.; Josue, J.; Pendon, Z.; Hiller, R. G.; Sharples, F. P.; Gosztola, D.; Wasielewski, M. R. *Journal of Physical Chemistry B* **2000**, *104*, 4569.

13. Zigmantas, D.; Polivka, T.; Hiller, R. G.; Yartsev, A.; Sundstrom, V. *Journal of Physical Chemistry A* **2001**, *105*, 10296.

14. Vaswani, H. M.; Hsu, C. P.; Head-Gordon, M.; Fleming, G. R. *Journal of Physical Chemistry B* **2003**, *107*, 7940.

15. Head-Gordon, M.; Graña, A. M.; Maurice, D.; White, C. A. *Journal of Physical Chemistry* **1995**, *99*, 14261.

16. Hamm, P.; Kaindl, R. A.; Stenger, J. *Opt. Lett.* **2000**, *25*, 1798.

17. Van Tassle, A. J.; Prantil, M. A.; Fleming, G. R. *Journal of Physical Chemistry B* **2006**, *110*, 18989

18. Zigmantas, D.; Hiller, R. G.; Yartsev, A.; Sundstrom, V.; Polivka, T. *Journal of Physical Chemistry B* **2003**, *107*, 5339.

19. He, Z. F.; Gosztola, D.; Deng, Y.; Gao, G. Q.; Wasielewski, M. R.; Kispert, L. D. *Journal of Physical Chemistry B* **2000**, *104*, 6668.

20. Shima, S.; Ilagan, R. P.; Gillespie, N.; Sommer, B. J.; Hiller, R. G.; Sharples, F. P.; Frank, H. A.; Birge, R. R. *Journal of Physical Chemistry A* **2003**, *107*, 8052.

21. Zigmantas, D.; Hiller, R. G.; Sharples, F. P.; Frank, H. A.; Sundstrom, V.; Polivka, T. *Physical Chemistry Chemical Physics* **2004**, *6*, 3009.

22. Zimmermann, J.; Linden, P. A.; Vaswani, H. M.; Hiller, R. G.; Fleming, G. R. *Journal of Physical Chemistry B* **2002**, *106*, 9418.

23. J. Kong, C. A. W., A. I. Krylov, C. D. Sherrill, R. D. Adamson, T. R. Furlani, M. S. Lee, A. M. Lee, S. R. Gwaltney, T. R. Adams, C. Ochsenfeld, A. T. B. Gilbert, G. S. Kedziora, V. A. Rassolov, D. R. Maurice, N. Nair, Y. Shao, N. A. Besley, P. E. Maslen, J. P. Dombroski, H. Daschel, W. Zhang, P. P. Korambath, J. Baker, E. F. C. Byrd, T. Van Voorhis, M. Oumi, S. Hirata, C.-P. Hsu, N. Ishikawa, J. Florian, A. Warshel, B. G. Johnson, P. M. W. Gill, M. Head-Gordon, and J. A. Pople. *J. Comput. Chem.* **2000**, *21*, 1532.

24. Pinto, E.; Catalani, L. H.; Lopes, N. P.; Di Mascio, P.; Colepicolo, P. *Biochemical and Biophysical Research Communications* **2000**, *268*, 496.